Doctoral Dissertation

New Mechanism of Absorption Collision Energy on Rolling-Over Protective Structure (ROPS) Using Compression-Expansion Crash box

(圧縮膨張型衝撃吸収部材を用いたロールオーバ保護構造の衝撃エネルギー吸収メカニズムに関する研究)

September, 2018

ZEFRY DARMAWAN

Graduate School of Science and Engineering

Yamaguchi University

Japan

New Mechanism of Absorption Collision Energy on Rolling-Over Protective Structure (ROPS) Using Compression-Expansion Crash box

(圧縮膨張型衝撃吸収部材を用いたロールオーバ保護構造の衝撃エネルギー吸収メカニズムに関する研究)

September, 2018

ZEFRY DARMAWAN

Supervisors

Prof. Ken KAMINISHI **Prof. Shigeyuki HARUYAMA**

Graduate School of Science and Engineering

Yamaguchi University

Japan

ABSTRACT

This paper clarifies the energy absorption mechanism of the cab frame corresponding to the roll-over protective structure (ROPS) using the compression-expansion thin-walled tube absorbing member. The summary is as follows.

It is important to protect operators from the impact of falls in heavy machinery. As a safety protection a rollover protection structure is applied to the cab frame. The cab is required to absorb the impact energy of a heavy machine fall accident and to keep the operator's survival space at the same time. Therefore, it is necessary for the cab to absorb energy without lowering the rigidity and strength with respect to a predetermined amount of deformation. Also, when deformation cracks occur at the weakest part of the frame, the load decreases rapidly and lost sufficient energy absorption performance. Since it is difficult to obtain various modifications for preventing the bending collapse of the frame and a cast member, while develop the cab to satisfy the ROPS standard for each weight of the heavy machine body. In addition, like the automobile, the energy absorbing members mainly used for absorbing the collision energy at the accident are not used at cab. Development cost and resources are required for each cab applied to ROPS in order to design each heavy machine individually. Simulation based on theoretical analysis improves efficiency by using the finite element method. In this research, we investigate the characteristics of the collapse of the cab frame corresponding to the ROPS standard, without considering the special cross sectional design frame and individual optimized parts to increase performance. A study on new absorption mechanism for improvement also investigates to enhancing performance of ROPS.

Chapter 1 present the research on the ROPS structure of the heavy equipment, the impact absorbing member and the problem of the impact energy absorbing mechanism in the previous research, and the outline of the research in this paper is shown. In chapter 2, the mechanical properties of the materials used for analysis and evaluation, and the properties of the newly proposed compressive expansion type absorbing member and cab frame are shown. In chapter 3, we showed the analysis environment such as the boundary condition of the simulation, the theoretical analysis by finite element method used in this research and the investigation result on ROPS test.

In Chapter 4, the characteristics of the cab frame and the weak points from the evaluation of the load-deformation curve and the energy-deformation curve in the thickness combination of each frame is varied based on the typical 6-post cab frame shape. As a result of specifying the members and parts, local wrinkles which become weak points in the four

different regions of the cab frame are shown. The important part in this cab frame is vertical pillar A, C, and H pillars.

Chapter 5, we investigated the bending characteristics of square tubes with expanded compression type energy absorption part for the purpose of preventing bending collapse of the frame member and occurrence of local wrinkles. The collapse form of the square tube was influenced by the thickness of the member and the dimension of the cross sectional area. The deformation mode was clarified into 3 type; side, bottom, and flat collapse. Particularly, in the flat collapse mode, it was shown that high energy absorption characteristics can be obtained because there is no local buckling.

In Chapter 6, the optimum design shape of the cab frame was investigated based on the results of the stress distribution specified along the three observation points on the square tube cross section. Using the basic shape of 6-post ROPS, the change of the stress and strain of the frame under the different plate thickness condition is investigated using those points. The energy absorption of the cab frame is increased, and at the same time also reduces the local buckling.

In Chapter 7, we propose a new energy absorbing mechanism using the compression expansion type absorbing member and compared it with the evaluation data of the preceding research. As the result, the members using the proposed mechanism have higher energy than the conventional one. The proposed mechanism is to install the compression expansion type absorbing member so that the load direction can be reversed to both end faces of the absorbing member and the energy can be absorbed in the tensile direction. Both end connection are made from bar with higher rigidity than the absorbing member, so it can be pulled, and the load transmitted to the frame can be absorbed. In addition, it was shown that attaching the absorbing member on the rear diagonal line of the cab frame (Chapter 4, H pillar take out) is effective.

Chapter 8 summarizes the results obtained and presented various parameters and conditions for optimum design of the cab frame using the new energy absorption mechanism for the ROPS structure. Finally, overall result of this research of ROPS using new mechanism of absorption collision energy on rolling-over protective structure (ROPS) using compression-expansion crash box could increase the ROPS performance. In line with increasing ability of ROPS it is possible to design single cab frame for various operating weight machine by adjust the size of compression-expansion member according to the ROPS standard testing criteria.

ACKNOWLEDGMENT

It would have been my honor to study in Yamaguchi University Japan and many regard and support from several persons during my study:

First of all, I would like to regard and deepest appreciation to my supervisors. Professor Ken KAMINISHI, and Professor Shigeyuki HARUYAMA for excellent guidance and motivation in my doctoral study. Thank you for your generous attention and sharing knowledge to enrich my research study. I also gratefully thank you to examiner committee; Professor Koichi GODA, Professor Xian CHEN, and Professor Junji OHGI for their suggestion and valuable review of my research paper. Also thank you for Associate Professor Tsuyoshi KOGA for help me preparing administration documents for conference and business travel accommodation.

Dear friends and members in Strength of Material Laboratory Yamaguchi University Japan for great moment, support, and discussion during my study. All lectures in Mechanical Engineering Department for a nice education atmosphere and transfer knowledge sessions. Appreciate to Mr Okajima, Mr Kadota, and Ms Tomoko ASANO for good daily administration activities during my stay in Ube city Yamaguchi Japan.

I am gratefully thank you to all my friends in Ube city for our friendship. Thank you to all Indonesian students in Yamaguchi Japan for happiness and great moments. For all member of PPI Yamaguchi thank you for great support and togetherness. Appreciate also for Indonesian Embassy in Japan for support and attention for my living in Japan. Gratitude to Brawijaya University Indonesia for give me an opportunity continue my study in Japan, Directorate General of Resources for Science, Technology and Higher Education, Ministry of Research, Technology and Higher education of Indonesia for funding support my study in Japan. All colleagues in Industrial Engineering Department of Brawijaya University for support me.

I would like to say thank you to my parents Drs. Sudarto, MSc and Iswati BSc, my parents in law Professor. Dr. Ir. Henny Pramodyo, MS and Dra Nurlaily for your love and care. Finally I would like to say special thank you to my wife Sativana Sari, AMd. NP, ST, my children Nadia Zeva and Narandra Zesa for your love, understanding, support, and motivation for me.

Zefry Darmawan

Ube City, Augt 8th, 2018

TABLE OF CONTENTS

LIST OF FIGURES

LIST OF TABLES

PARAMETER LIST

Symbol	Definition	Unit
R	Radius of circular	mm
C	Side length of rectangular tube	mm
b	Width	mm
t	Thickness	mm
L	Length	mm
Ɛ	Elongation	mm
A	Area of cross section	mm
D	Diameter	mm
E	Young's modulus	GPa
E_h	Hardening modulus	GPa
G	Shearing modulus	GPa
v	Poisson's ratio	
σ_y	Yield stress	MPa
σ_T	True stress	MPa
M	Momen	N . m
κ	Curvature	m^{-1}
ϵ	Strain	
ϵ_T	True strain	
τ	Shear stress	MPa
U_r	Modulus resilience	GPa
I	Momen of inertia	Kg . m^2
y	Distance of deflection from normal axis	
Θ	Slope angle	°
C_{2f}	Vertical shrinkage of tube	Mm
C_{1f}	Horizontal stretch of tube	Mm
μ	Ratio vertical shrinkage	
F	Load	N or kN
P_{peak}	Compressive peak load	N or kN
P_{ave}	Compressive average load	N or kN
α	Contact slope	°
m	mass	Kg
δ	Displacement	mm
	Special note Figure 3.1	
BP	Boundary planes of DLV	
E	Horizontal mid-point of upper ROPS structural member	
F	Load force	
H	Height of upper ROPS structural member	
L	Length of ROPS	
LAP	Load application point	

LDD	Load distribution device
S	Socket
W	Width of ROPS Special note Figure 3.1
L[W]	Length [width] of ROPS Special note Figure 3.3
A	Angle bisector of two tangent lines (B and C)
B	Tangent line parallel to D on outer surface of curved ROPS structural member
C	Projection of top surface of upper ROPS structural member
D	Straight line intersecting ends of curved ROPS structural member with mating member
H	Height of load application zone
I	Intersection of curved surface with flat surface
Y	Intersection of vertical line from LAP to inner surface of vertical member Special note Figure 3.4
a	Upper ROPS frame member to which lateral load is applied
b	Outermost point from end view of frame member a
c	Vertical line throught point b
d	Vertical plane parallel to the machine longitudinal centerline through line c
LSGP	Lateral simulated ground plane

CHAPTER I

INTRODUCTION

1.1 Background

Safety is one of main concern at work environment. Working device such as heavy equipment should follow safety standard procedures. Rollover protective structures (ROPS) were developed together with operator restraint systems, the purpose is to keep the operator within a protected area and maintain the body during lateral rollover accidents. This protected area, however, is not enough for major accidents, and the rollover kinetic energy should be diverted through the permanent plastic deformation of ROPS components, so that the kinetic energy hit the operator is at a minimum or none at all [1]-[3]. Figure 1.1 shows several accidents due to roll over condition at excavator.

Figure 1.1. Accidents due to rolling over on heavy machinery.

Cabs should be designed such that energy absorption occurs without reducing stiffness and strength [4]. When the Cab cracks, the energy is not absorbed by the permanent plastic deformation of the ROPS components [5]. Supporting structure in ROPS usually assembly of bars or kind of tubular frame. This structure mainly as protection and not equipped with special device for absorb the rollover energy. Figure 1.2 shows condition of cab frame currently compare with automotive vehicle. The research method which undertakes real vehicle rollover tests is similarly to the actual situation in the rollover accident [6]. This test is the most basic and intuitive method of comprehensively evaluating vehicle safety performance. However, its repeatability is poor and each test needs large amounts of resources [6]. Improving energy absorption by partially modifying a shape is a potential method. Andrews et al. [7] reported that crushing a cylinder in an axisymmetric (concertina) mode absorbs more energy than crushing in a non-axisymmetric (diamond) mode. They

showed that the crushing mode was dependent on not only the thickness and the radius of a cylinder but also on its length.

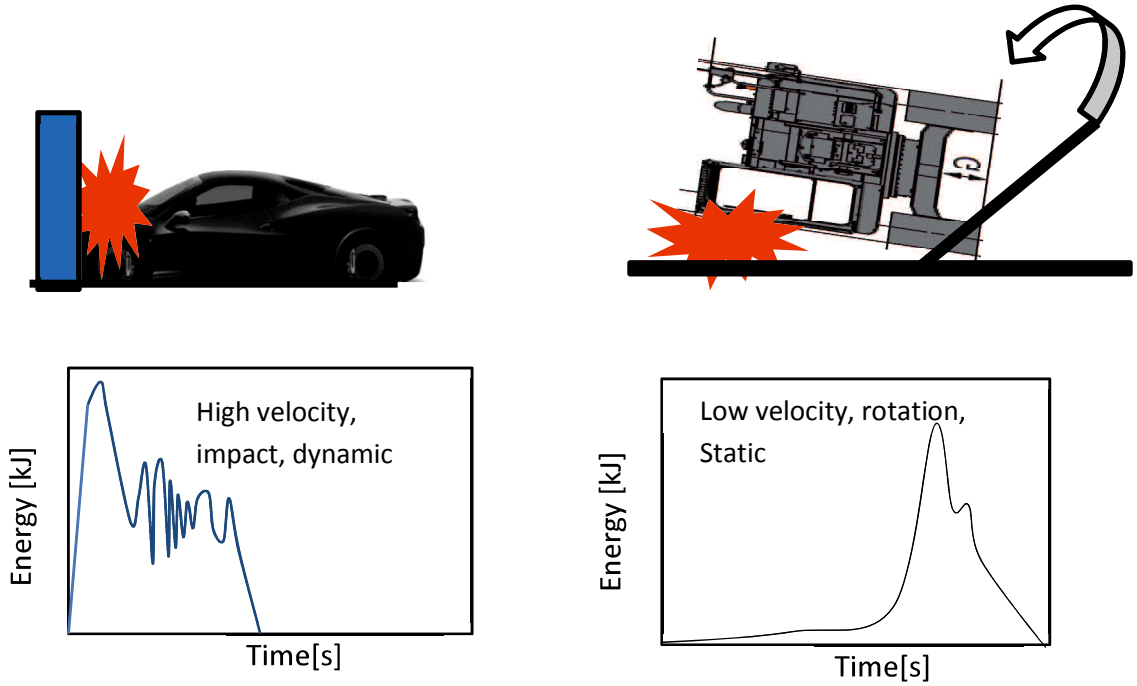

(a). Energy – Time curve at frontal crash of automotive vehicle.

(b). Energy – time curve at roll-over of heavy machinery.

Figure 1.2. Comparison risk characteristic between automotive vehicle and heavy machinery.

Modeling partial geometry of cab frame was conducted by Elmarakbi et al. [8] conducted extensive research using finite element simulations of the thin S-shaped longitudinal members with variable cross-sections made of different materials. They used the optimized members to determine the desired variables for the design of energy absorbing system to enhance vehicle safety. Further, full geometry modeling of cab frame leaded by [9], obtained that characteristic cab according to thickness combination was influenced by wrinkle which can reduce energy absorption.

Some modification was subjected to increased energy and avoid wrinkle. [10]-[11] modeling cab frame for roll over test according to certain model developed by specific companies and conducted FEA analysis to perform result for later loading condition. Figure 1.3 shows comparison project life cycle development between conventional method and Analysis Led Design (ALD) which perform integration of computer aided design and finite element method to create product design robustness. Figure 1.4 shows comparison testing condition in conventional method and finite element simulation in ALD. ALD enhance the product life cycle more forward than conventional method a digital engineering. This

approach will solve several problems tent to high expenses, high resources, and reduce development time.

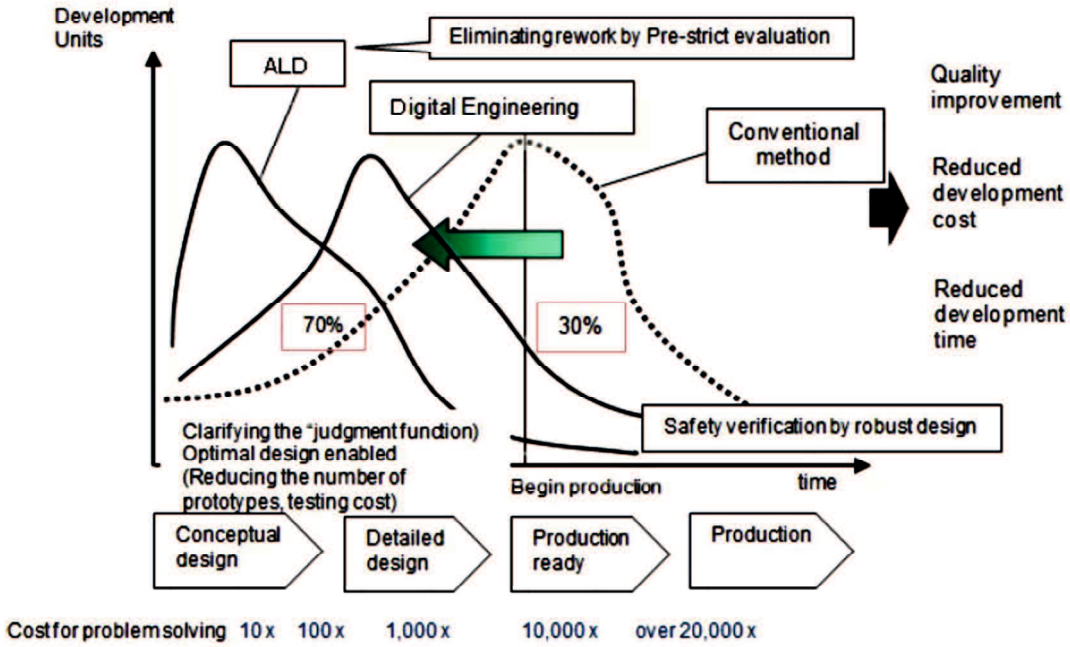

Figure 1.3. Comparison product life cycle chart between ALD and conventional method.

- Expensive
- Time-consuming
- High resources

(a). Real experiment testing of cab frame (conventional method).

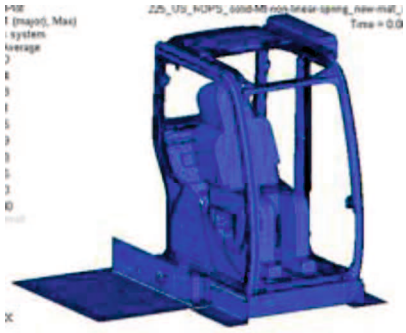

(b). Finite element simulation in Analysis Led Design (ALD).

Figure 1.4. Comparison cab frame testing condition between real experiment and ALD.

1.2 Comparison Studies of ROPS.

Below are the comparison studies of cab frame with previous researchers:

1. C Chen, et all [6]. 2012
   a. Title: Effect of lateral stiffness coefficient of loader ROPS on human injury in a lateral roll over incident.
   b. Application: two and six post ROPS
   c. Result:

- Introduce new approach to verify ROPS performance using LSC (lateral stiffness coefficient)
- LSC range 1-1,5 meets the standard ISO 3471
- Higher LSC will absorb smaller collision energy

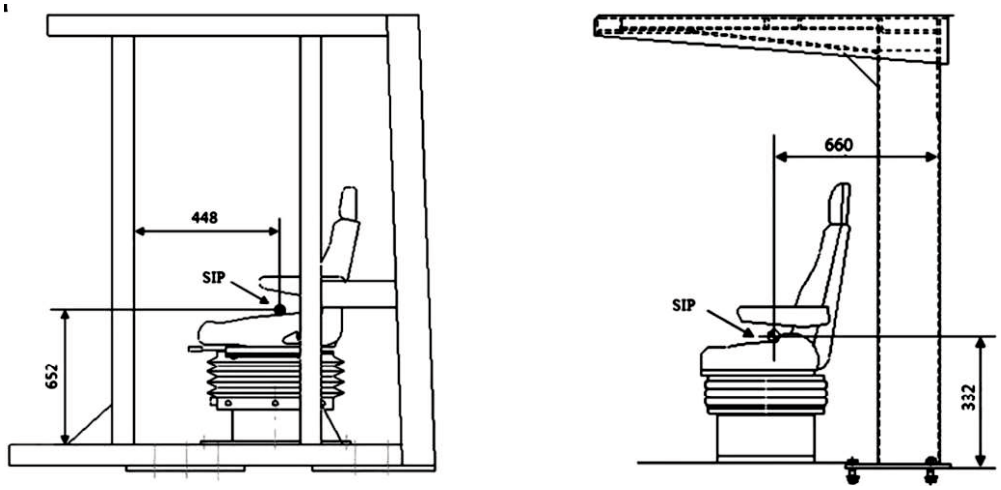

(a). Six-post ROPS. (b). Two-post ROPS.

Figure 1.5. Six post and two post of ROPS [6].

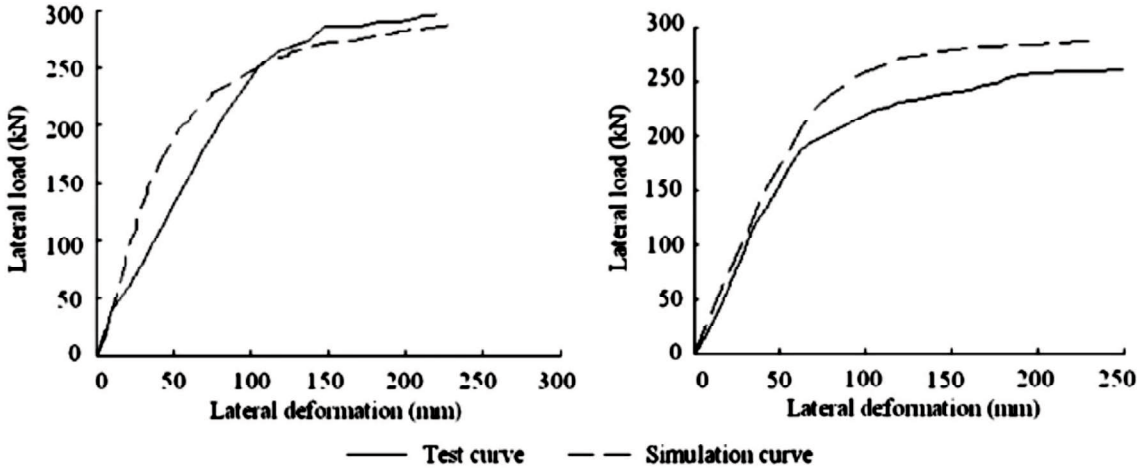

(a). Load-Deformation curve six-post ROPS. (b). Load-Deformation curve two-post ROPS.

Figure 1.6. Lateral load- deformation curve of two and six post ROPS [6].

2. F Khorsandi, et all [12]. 2017
   a. Title: Developing and evaluating a finite element model for predicting the two-post rollover protective structure nonlinear behavior using SAE J2194 static test.
   b. Application: two post ROPS (tractor model Allis Chalmers 5040 and Long 460)

c. Result:

- Use FE to predict non-linear force deflection curve according to SAE J2194 static test.
- Compare between experiment test and FE simulation using Ramberg-Osgood material model.
- Result of experiment was found more accurate than FE models.

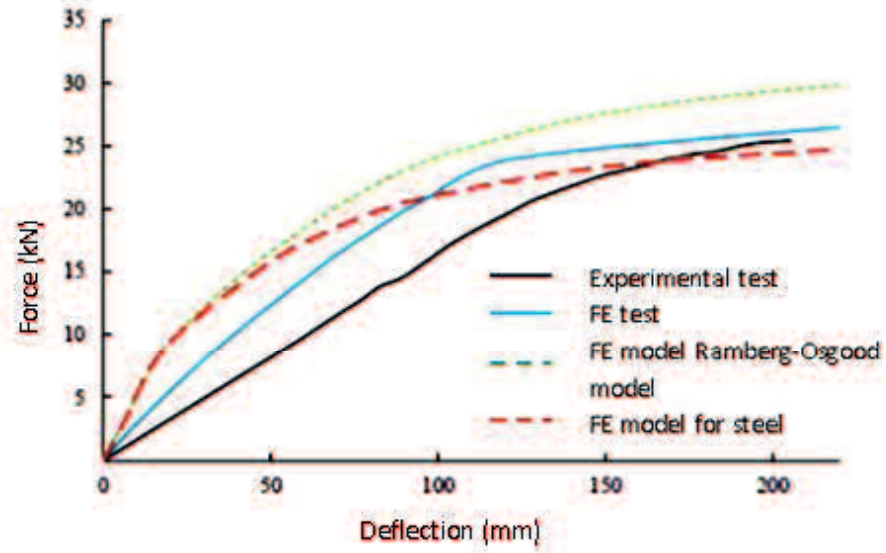

(a). ROPS deflection under rear loading for Allis Chalmers 5040.

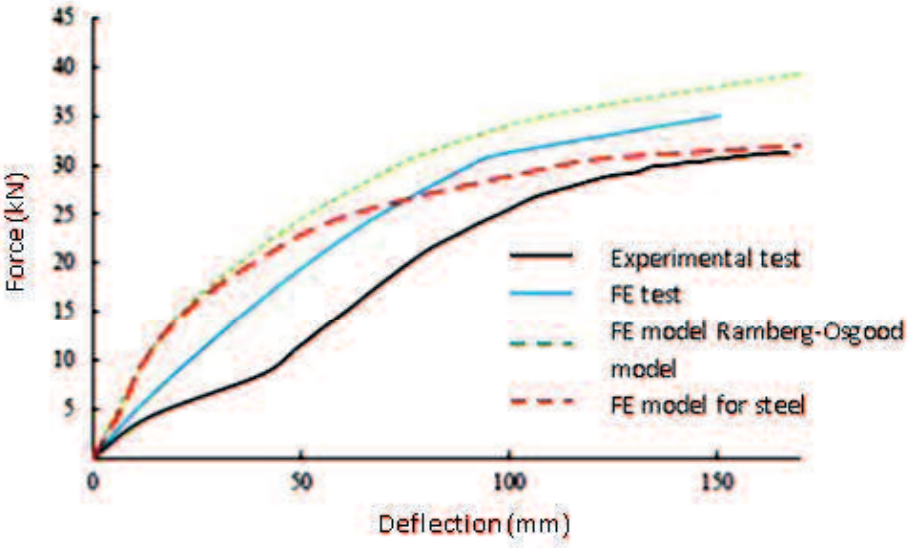

(b). ROPS deflection under rear loading for Long 460.

Figure 1.7. Comparison result Force – Deflection curve between of Allis Chalmers 5040 and Long 460 [12].

3. J Mangado, et all [13]. 2007
   a. Title: Design Calculations on Roll-over Protective Structures for Agricultural Tractors.
   b. Application: four post ROPS (tractor model Massey Ferguson 178)
   c. Result:
      - Provide design calculation for ROPS and compare with FE simulation.
      - Calculation method is able to determine the needed steel section of the structure tube, minimum height of the beam, quality and shank diameter of screws of ROPS.

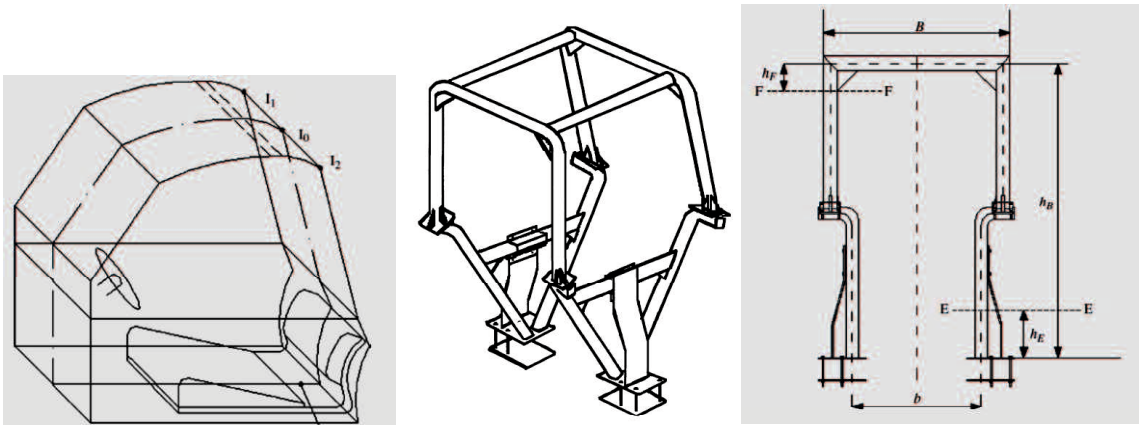

(a). Clearance zone of ROPS. (b). Isometric view of ROPS. (c). Rear view of ROPS.

Figure 1.8. Finite element models of four-post ROPS [13].

4. J. R Alvaro, et all [14]. 2010
   a. Title: Assessing the safety provided by SAE J2194 Standard and Code 4 Standard code for testing ROPS, using finite element analysis.
   b. Application: four post ROPS
   c. Result:
      - Using FE modeling to provide ROPS static test and compare with experiment test.
      - FE method possible to evaluate the fixing elements and different structural ROPS and the safety level provided.

5. J Karlinski, et all [11]. 2013
   d. Title: Simulation tests of roll-over protection structure.
   e. Application: two post ROPS
   f. Result:
      – Provide methodology of conducting strength test for protection structures using finite element modeling.

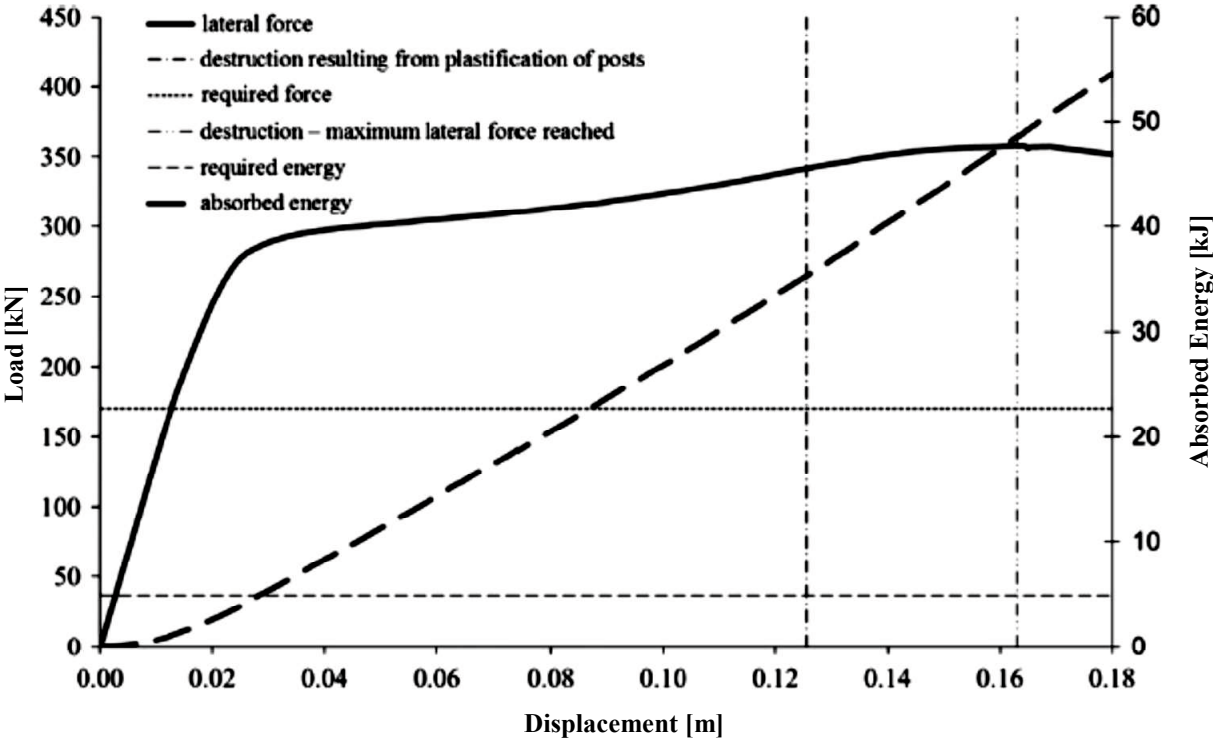

Figure 1.9. Main characteristic of lateral testing of ROPS [11].

6. T. H Kim, et all [15]. 2001
   a. Title: Multiaxial softening hinge model for tubular vehicle roll-over protective structures.
   b. Application: four post ROPS
   c. Result:
      - Provide a computational tool for design ROPS composed of rectangular thin walled tubes. This tool corresponding to SAE standard J1040 static test.
      - Introduce term “the hinge super element”, consists of two nodes separated by a small distance. Each node has six degrees of freedom and the components of stiffness at each node are able to switch into appropriate value provide rigid response in the collapse stage.

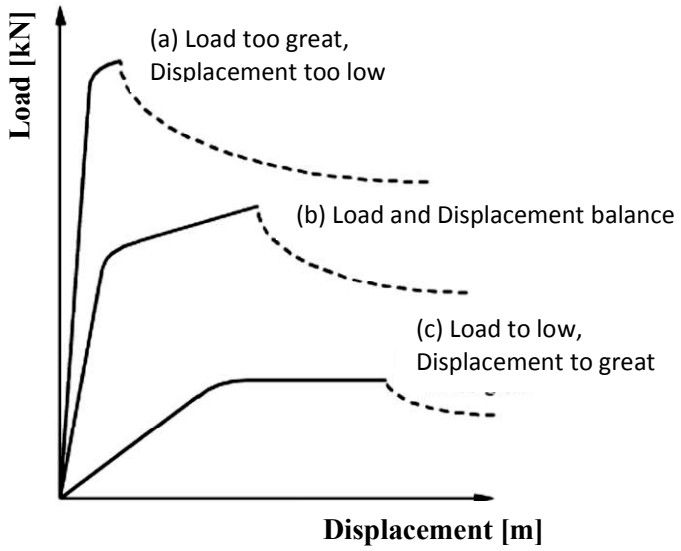

Figure 1.10. Load-deflection curves of stiffness respond [15].

7. V Pardeshi [10]. 2015
   a. Title: Design of ROPS (Roll-over protective structure) for operator cabin.
   b. Application: six post ROPS
   c. Result:
      - Provide a finite simulation for standard testing of ROPS according to ISO 3471, using two types of test; vertical load, and lateral load.
      - Provide the initial testing information to predict performance ROPS against the specific load in real experiment testing.
8. A Fabbri, et all [16]. 2002
   a. Title: Validation of a Finite Element for the design of Roll-over Protective Frame Structure (ROPS) for Agricultural Tractors.
   b. Application: four post ROPS of commercial tractor
   c. Result:
      - Create a self-defined finite element numerical model comprised of code C language which complies with ROPS standard test of OECD/EEC codes.
      - Higher layer finite element model provide higher precision compare with non-layered finite element model.

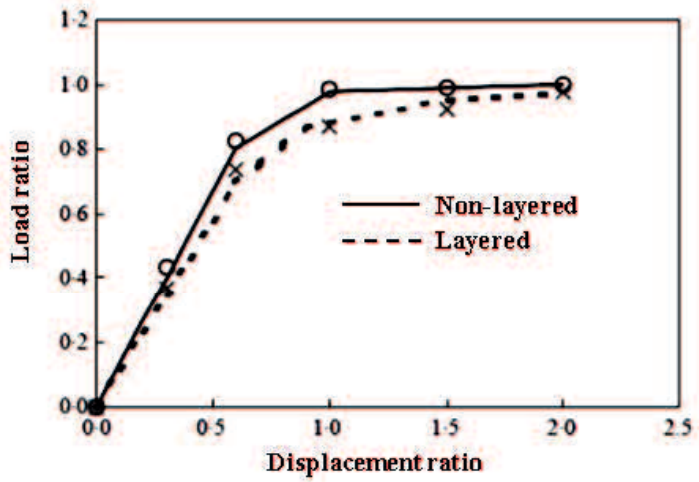

(a). Load ratio-displacement ratio curve for layered and non-layered finite element model.

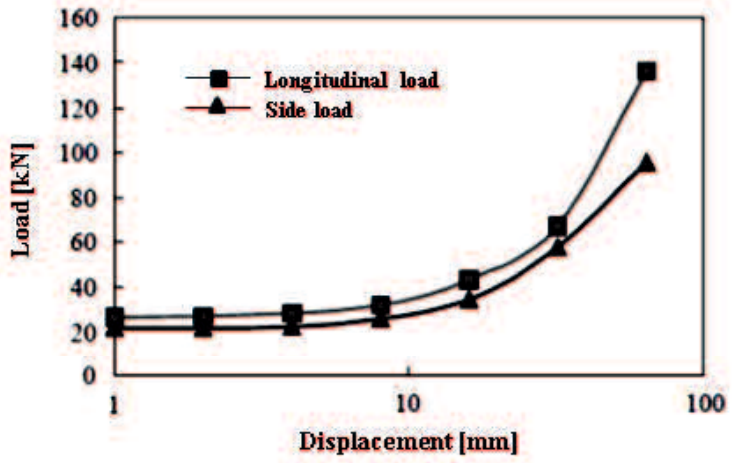

(b). Comparison between longitudinal loading and side loading.

Figure 1.11. Comparison Load-displacement curves for agricultural tractor [16].

9. P Ayers, et all [17]. 2017
   a. Title: ROPS design to protect operators during agricultural tractor rollovers.
   b. Application: two post ROPS (tractor model Allis Chalmers 5040)
   c. Result:
      - Develop a computer-based ROPS Design Program (CRDP) to generate ROPS design based on weight and dimension of tractor.
      - Develop a foldable ROPS which effective to protect operator during rollover. This ROPS model also predicts the higher center of gravity of vehicle, possibility of continuous rollover is higher. Appropriate ROPS height assists to stop the roll.

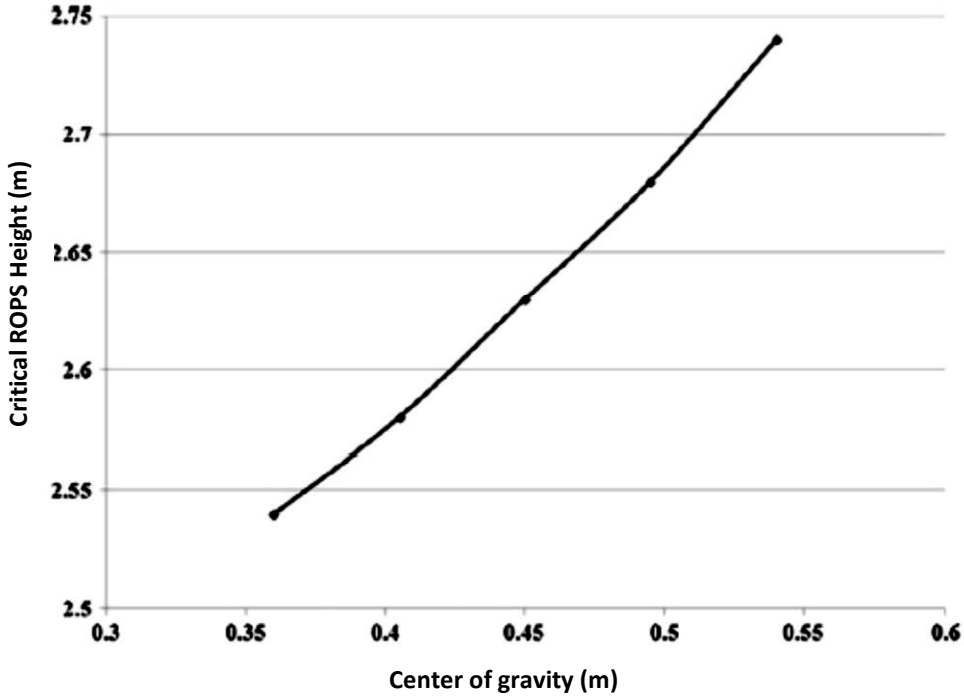

Figure 1.12. Influence of COG to critical ROPS height [17].

10. J. R Harris, et all [18]. 2011
    a. Title: Predicting the performance of cost-effective rollover protective structure designs.
    b. Application: two post ROPS (tractor model Ford-3000) according to SAE J2194.
    c. Result:
        - Cost-effective rollover protective structure (CROPS) concept is to increase the percentage of tractors in United States with ROPS installed by lowering the economic barrier to retrofitting old tractors with ROPS.
        - Probabilistic design simulation was used to identify the test response in SAE J2194 and OSHA 29 CFR1928.52. the simulation show that SAE J2194 static test sequence could be a more conservative design test than OSHA static test series.

11. W Abramowicz [19], 2003
    a. Title: Thin-walled structures as impact energy absorbers
    b. Application: thin walled rectangular tube as automobile crashbox
    c. Result:

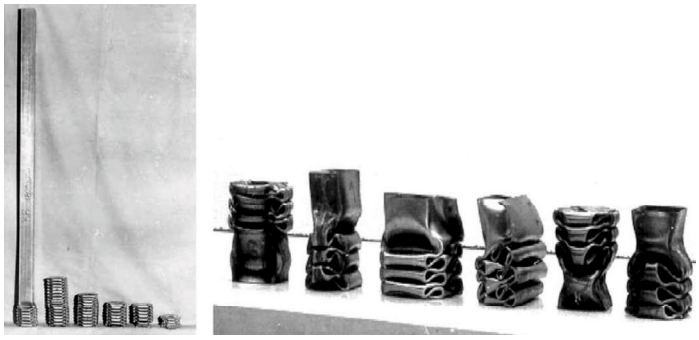

Figure 1.13. Axial deformations on rectangular tube [19].

- Folding modes based on super folding element theory
- Folding parameter determined by assumption
- Crushing force determined from numerical derivation

12. Sami E Alkhatib, et all [20]. 2018
    a. Title: Collapse behavior of thin-walled corrugated tapered tubes under oblique impact.
    b. Application: thin walled corrugated tapered tube as automobile crash box
    c. Result:

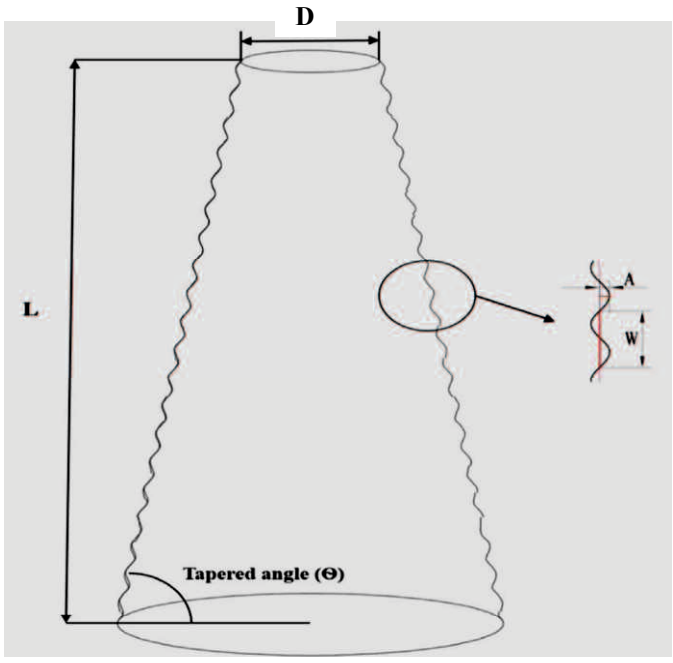

(a). Parameter of corrugated tapered tube.

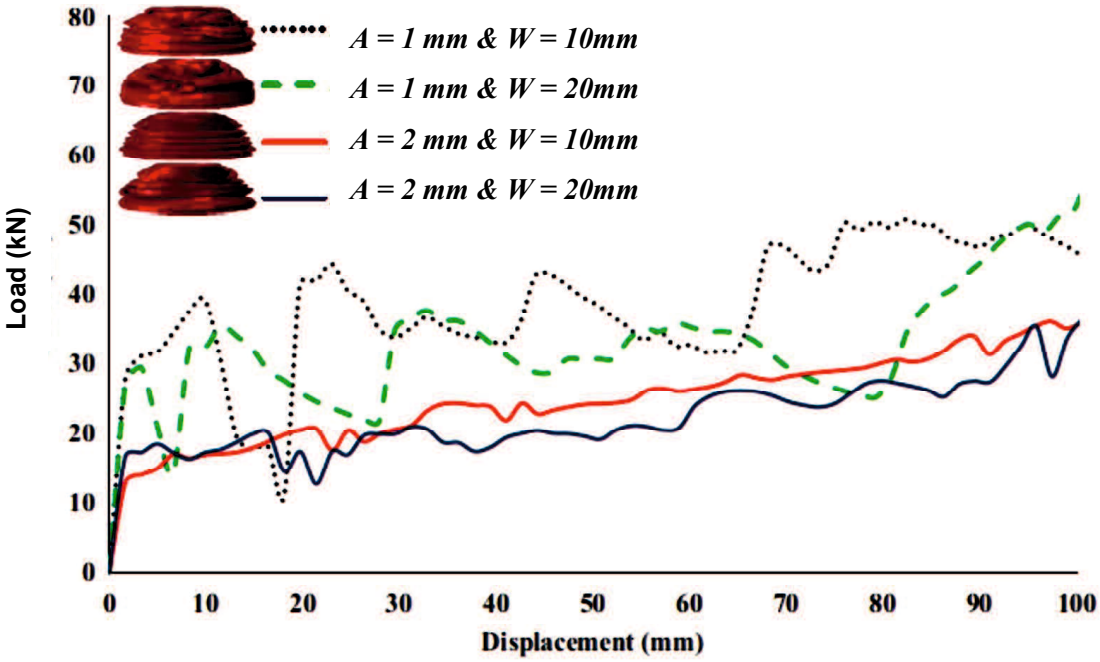

(b). Load-displacement curve for corrugated tapered tube R=20 [mm], t=2 [mm], L=150 [mm].

Figure 1.14. Characteristic of tapered tube under axial compression [20].

13. X W Zhang, et all [21]. 2009

a. Title: Axial crushing of circular tubes with buckling initiators.

b. Application: thin walled Circular tubes with buckling initiator as automobile crashbox

c. Result:

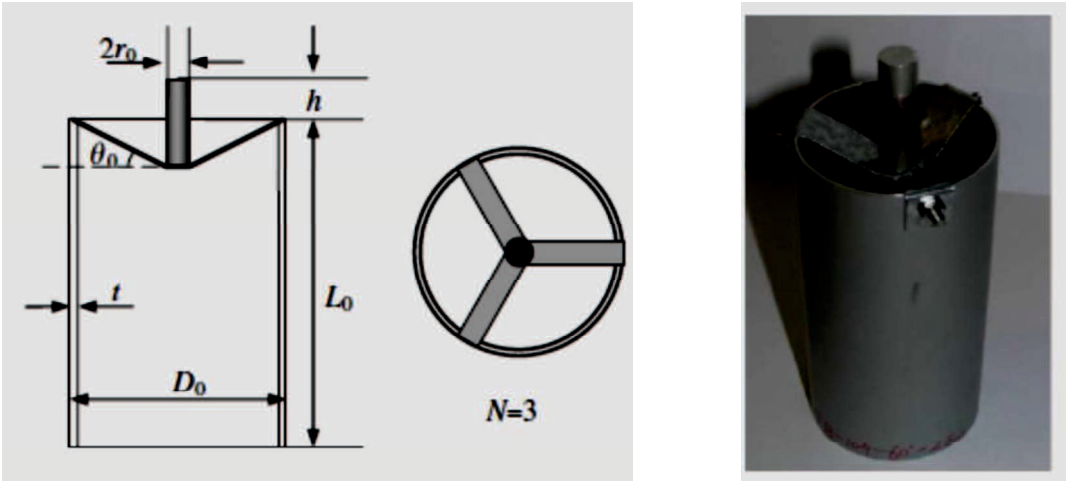

(a). Parameter of circular tube with buckling initiator.

(b). Real condition circular tube with buckling initiator.

Figure 1.15. Circular tubes equipped with buckling initiator [21].

- Peak force reduced by buckling initiator about 30%.
- New deformation resulted was switched from ring to diamond mode and provide stable deformation end results.

14. S Haruyama, et all [22]. 2013
    a. Title: Modes of collapse of compress-expand member under axial loading.
    b. Application: thin walled 3 pieces circular tubes with (compress-expand)
    c. Result:

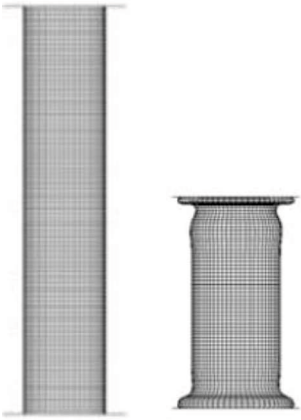

(a). Axial crush for cylindrical tube (pre crush and post crush).

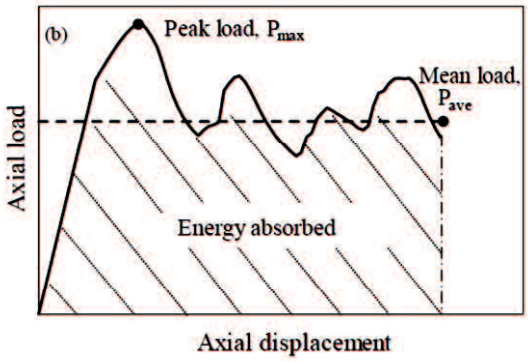

(b). Load-displacement curve for cylindrical tube.

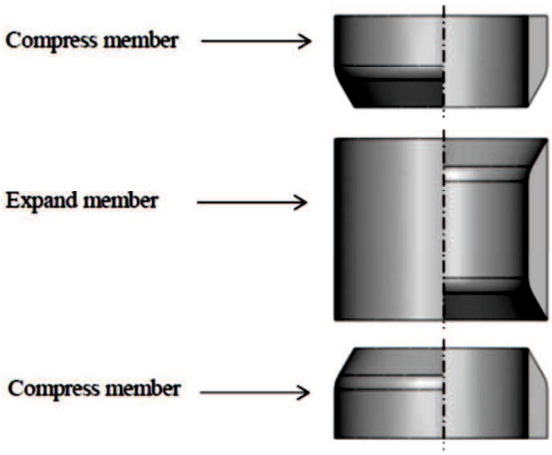

(c). Compress-expand tube geometry.

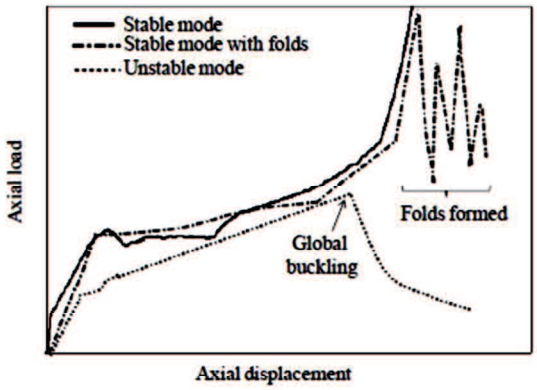

(d). Load-displacement curve for compress-expand tube.

Figure 1.16. Comparison characteristic of circular tubes and compress-expand tubes [22].

- Axial collapse of compress-expand member tent to no fold formed.
- Stable region obtained wider range than cylindrical tube.

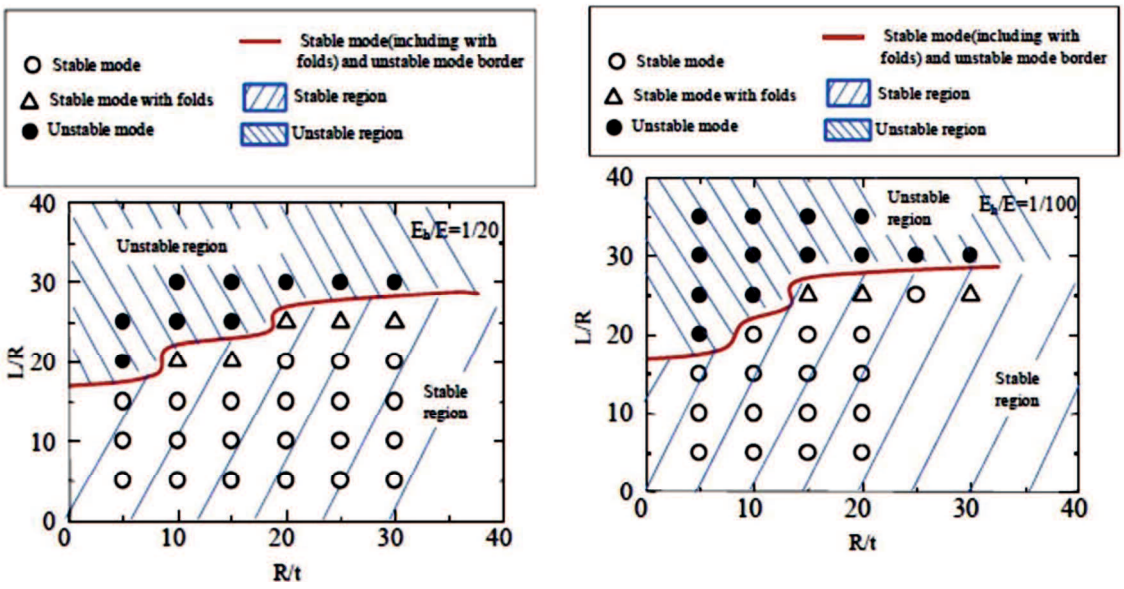

(a). Deformation map hardening ratio (Eh/E=1/20).

(b). Deformation map hardening ratio (Eh/E=1/100).

Figure 1.17. Deformation map of compress-expand tubes [22].

15. AF. Johnson [23]. 1973

a. Title: Bending and torsion of anisotropic beam.

b. Application: mathematical formulation for bending and torsion of composite material

c. Result: bending stiffness increase if torsion is prevented.

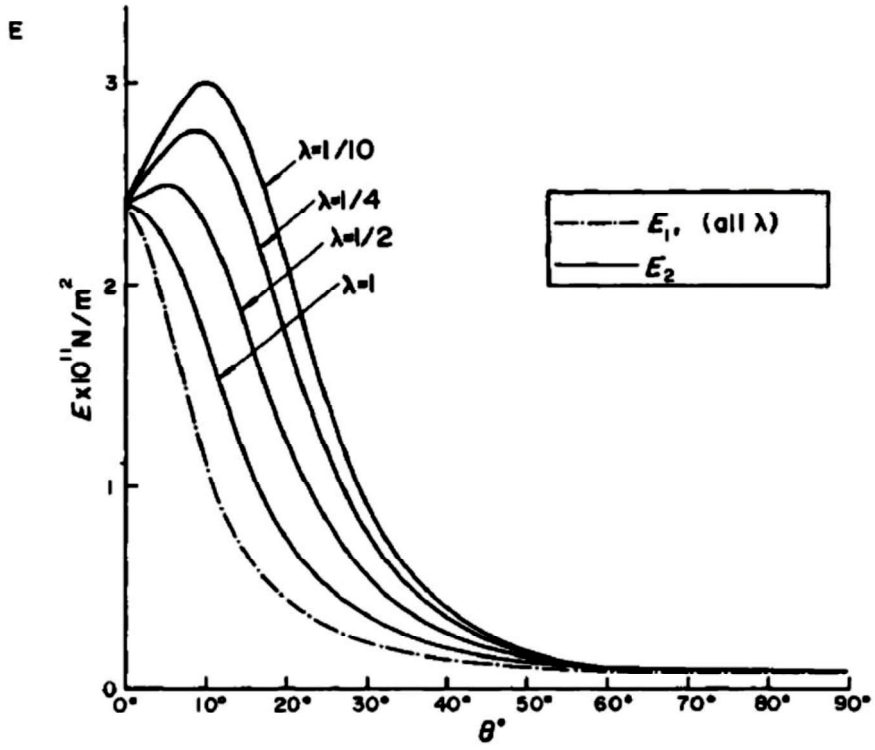

(a). Stiffness - slope curve for constrained bending.

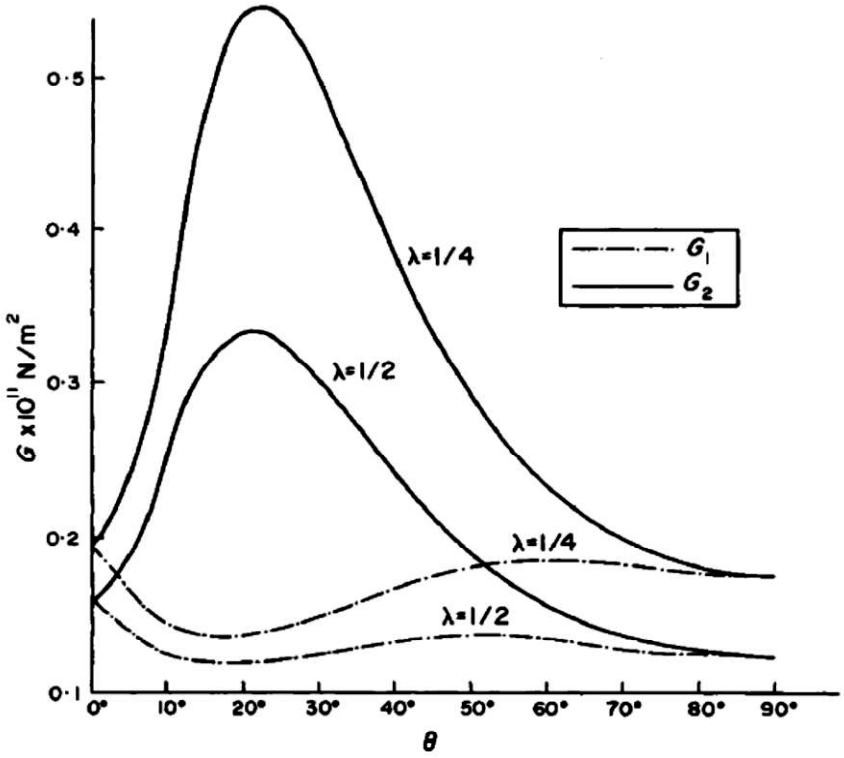

(b). Shear modulus – slope curve for constrained torsion.

Figure 1.18. Effective longitudinal stiffness and effective shear modulus for constrained torsion [23].

16. J. M. Alexander [24]. 1959

a. Title: An approximate analysis of the collapse of thin cylindrical shells under axial loading.
b. Application:
c. Result:

An analytical approach of square tube collapse according assumption:

- Shell collapse mode is concentric
- Elastic strain and work hardening ignored Material is assumed as plastic-rigid

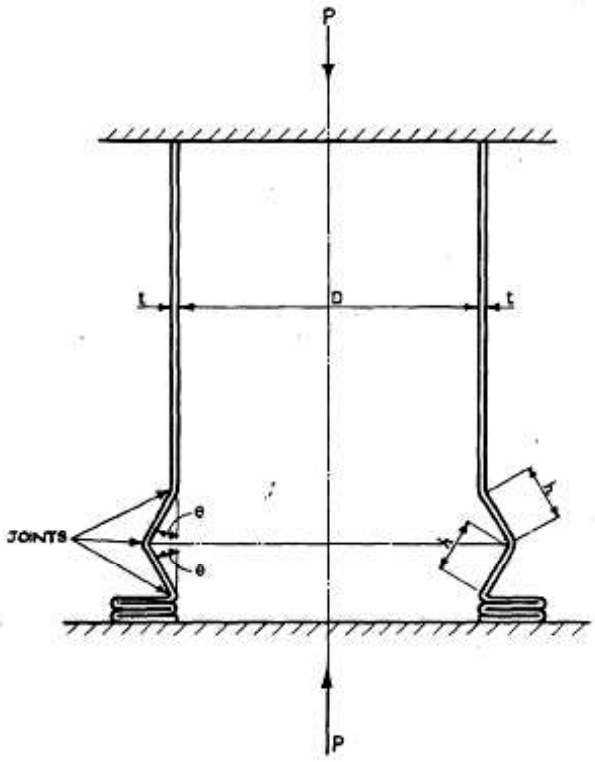

(a). Assumed collapse mode.

Table 1.1. Parameter of cylindrical tube.

Diameter (in)	t (in)	t^1,5 √D (in^2)	P (lb)
1.43	0.03	0.006214	2600
1.43	0.04	0.009567	4260
1.43	0.05	0.013370	6650
2.12	0.03	0.007566	3450
2.12	0.04	0.011648	4990
2.12	0.05	0.016279	6980
2.66	0.03	0.008475	3700
2.66	0.04	0.013048	5610
2.66	0.05	0.018235	7480

P : Collapse load

t : shell thickness

D : shell diameter

h : distance between joints (assume same distance)

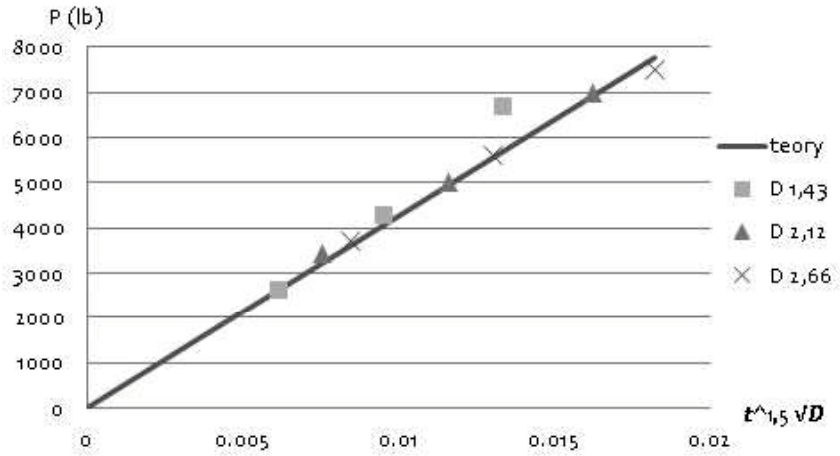

(b). Collapse load – $t^{1.5}\sqrt{D}$ curve for mild stell tubes.

Figure 1.19. Approximation model of axial deformation of cylindrical tube [24].

17. B. Zheng, et all [25]. 2016

a. Title: Study on the Bending Capacity of Cold-formed Stainless Steel Hollow Sections

b. Application: bending on cold-formed stainless steel rectangular and circular hollow section

c. Result:

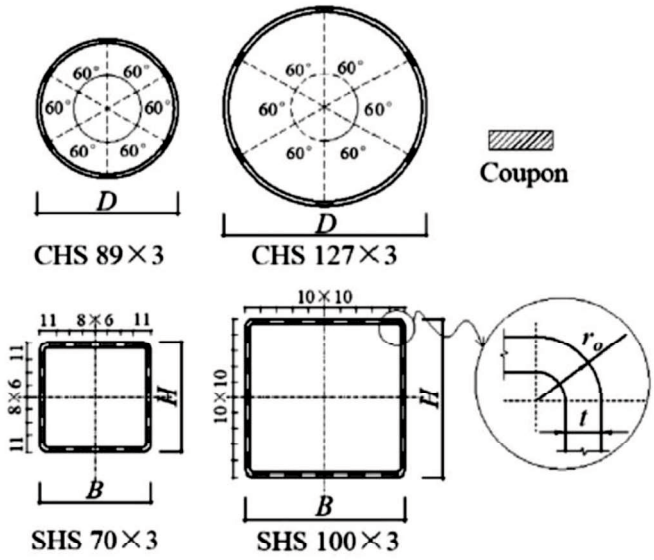

(a). Parameter of cylindrical and rectangular tubes.

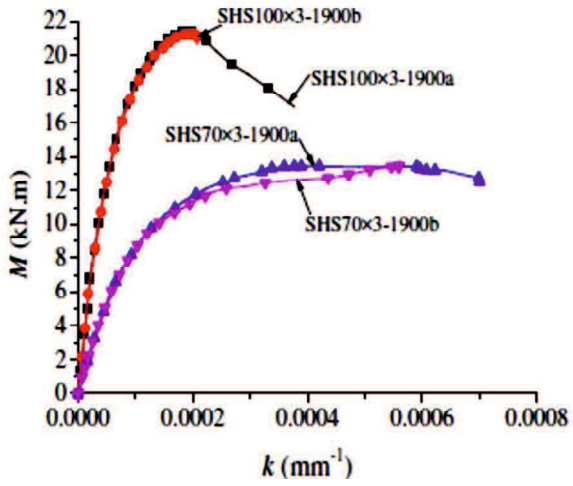

(b). Momen – curvature curve for rectangular hollow section.

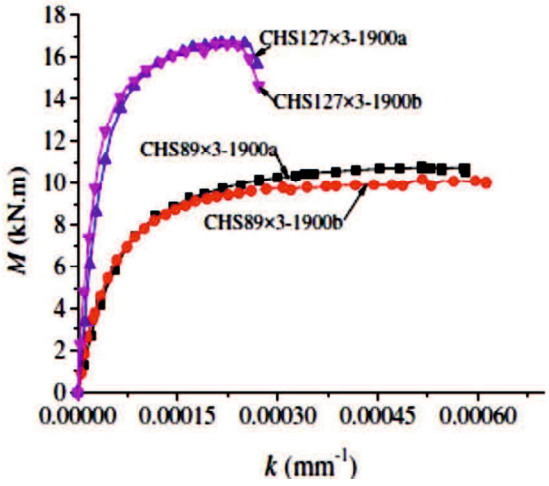

(c). Momen – curvature curve for cylindrical hollow section.

Figure 1.20. Stainless steel hollow section model and moment-curvature curve of rectangular and cylindrical tube [25].

18. F. Paulsen, et all [26]. 2001

a. Title: A design method for rectangular hollow sections in bending.

b. Application: bending of aluminum alloy to determine local post buckling

c. Result:

Slenderness ratio (b/t) and width of flange are the main parameters related to the bending radius at the onset of plastic buckling and magnitude of local deformation

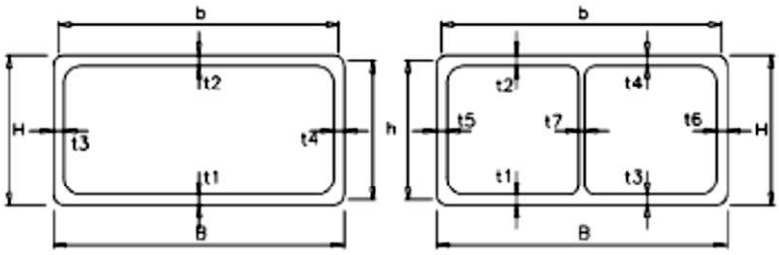

SC (single chamber) DC (double chamber)

(a). Parameter of rectangular hollow cross section for SC and DC.

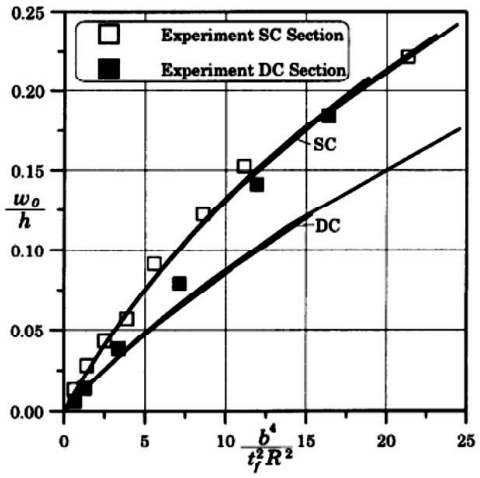

(b). Suck-in curve for SC and DC section tube.

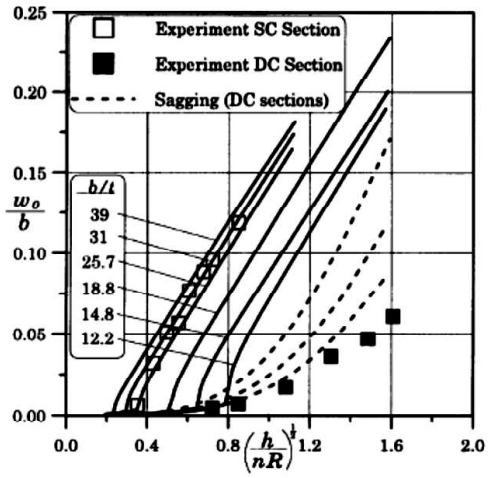

(c). Buckling wave depth of the compressive flange for SC and DC section tube.

Figure 1.21. Parameter of rectangular tubes and characteristic of buckling wave in SC and DC section [26].

19. D. H. Chen, et all [27]. 2016

a. Title: Rectangular hollow section in bending : Part I – Cross sectional flattening deformation
b. Application: bending of rectangular hollow section
c. Result:

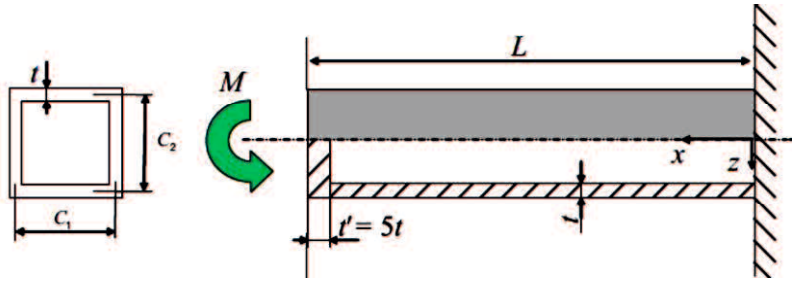

(a). Rectangular tube model.

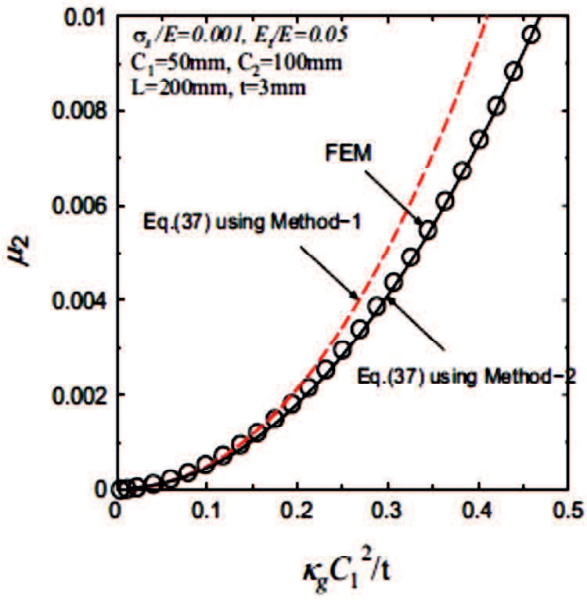

(b). Vertical shrinkage at $\sigma_s/E=0,001$; $E_t/E=0,05$; t=1,5mm.

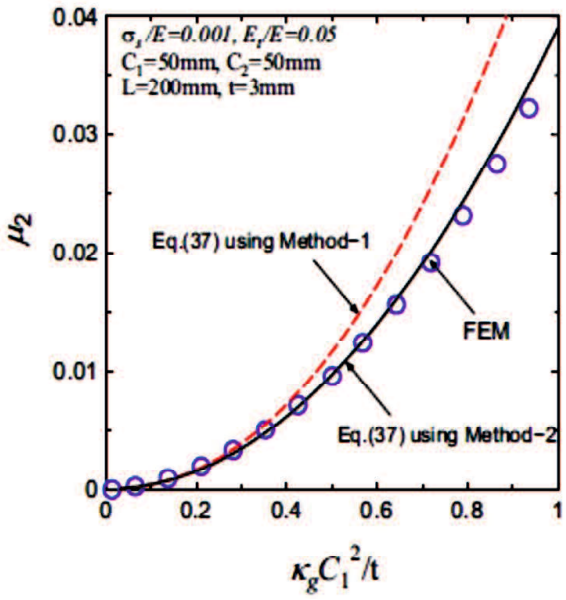

(c). Vertical shrinkage at $\sigma_s/E=0,001$; $E_t/E=0,05$; t=3mm.

Figure 1.22. Rectangular tube model and comparison result of vertical shrinkage under various parameter conditions [27].

1.3 Research Objectives

As mentioned before in research background that the main object of this research is ROPS or cabin frame. The research focus on develop method to improve performance of cab frame using series of improvement technique. The important point on whole research step defined as statement:

Improve performance the rolling over protective structure (ROPS) and investigate the characteristic of cab frame by develop the design which can absorb the rolling over energy accident.

Below are the problem statements of the following research objective:

- What is the characteristic of rolling over protective structure (ROPS) in lateral collision during accident and the deformation process of whole structure against the external load?
- How to improve performance of cab frame by using the new mechanism of energy absorber (compress-expand thin walled tubes) as integrated part in whole structure?

Research novelty in this study is explained in figure 1.24 below.

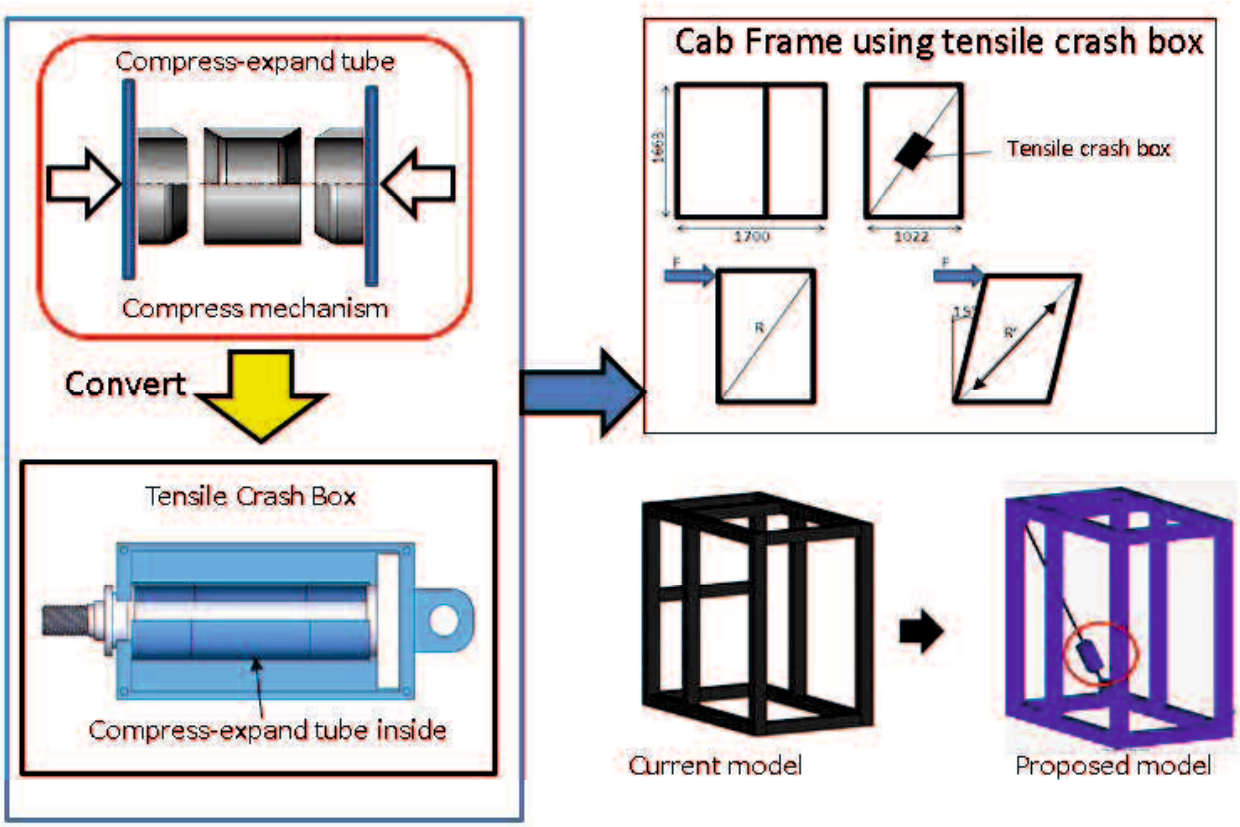

Figure 1.23. Research novelty of this study.

1.4 Outline

The complete dissertation is organized in the following eight chapters:

1. Chapter I describes about the introduction, related to background, previous studies and purpose of the research. The comparison of this study with other studies was compared. This chapter also introduce the new mechanism to improve cab frame performance by using thin-walled tubes, furthermore the mechanism transform axial compression stress of tubes become tensile stress to absorb deformation energy of cab frame. This is the original idea of this research.
2. Chapter II explains about the literature review that related to the research. Initially from mechanical properties of material, bending and deformation modes of rectangular tubes, axial compression of tubes, design of ROPS for cabin operator, and finite element modeling.
3. Chapter III is about the simulation environment of cab frame in finite element modeling, experiment apparatus that used in common cab frame test, and the standardization of ROPS testing according to ISO 3471: 2008.

4. Chapter IV is about the characteristic of cab frame as ROPS during lateral roll-over accident. A typical six-post ROPS used in this study showed load-deformation and energy-deformation curve in whole structure. Using Taguchi's method by improve thickness level reduced wrinkle in several area of cab frame. Also, critical area in cab improved by preforming vertical part of cab which increased initial strength of parts.
5. Chapter V is the research about bending of square tubes these tubes were used in cab as pillar, characteristic of bending deformation, type of bending deformation, flattening in bending deformation, and maximum bending moment due to flattening. Compress-expand type of absorption energy on lateral bending using thin-walled tube also described in this research. This research introduce the compress-expand tube as energy absorption in bending moment. Square tube equipped with compress-expand tubes showed increasing absorption energy of bending and reduce buckling.
6. Chapter VI discuss about optimized design parameter of cab frame to improve energy absorption due to lateral load. This research explores detail stress distribution at critical parts specified along the three observation points on the square tube cross section. A basic shape of six-post ROPS was used in this study with design parameter scope is thickness condition. The energy absorption of the cab frame is increased, and at the same time also reduces the local buckling. Optimized thickness condition was obtained from Taguchi's, increased energy absorption of cab frame and reduce stress at several parts while encounter lateral load.
7. Chapter VII is about implementation of analysis Led Design (ALD) to improve performance of ROPS by conducted series of design. Several designs introduced in this study; improve bending capacity of vertical pillars, and install additional part as energy absorber in complete structure. Result from each design condition compared to obtain the highest absorption energy of cab frame. A new energy absorbing mechanism using the compression expansion type was introduced in this research and called as tensile crash box. It is obtained that new mechanism of energy absorber resulted highest performance of cab frame. The new mechanism compression expansion type member reversed the direction of the absorbing and the energy can be absorbed in the tensile direction. The research show the tensile crash box (compress-expand tubes) could increase energy absorption more than 50% compare with cab frame without tensile crash box.
8. Chapter VIII is the conclusion of the whole chapter in this study.

CHAPTER II

LITERATURE REVIEW

2.1 Mechanical Properties

The mechanical properties of materials are ascertained by performing carefully designed laboratory experiments that replicate as nearly as possible the service conditions. Factors to be considered include the nature of the applied load and its duration, as well as the environmental conditions. It is possible for the load to be tensile, compressive, or shear, and its magnitude may be constant with time, or it may fluctuate continuously. Application time may be only a fraction of a second, or it may extend over a period of many years. Service temperature may be an important factor.

The role of structural engineers is to determine stresses and stress distributions within members that are subjected to well-defined loads. This may be accomplished by experimental testing techniques and/or by theoretical and mathematical stress analyses. These topics are treated in traditional stress analysis and strength of materials texts. Materials and metallurgical engineers, on the other hand, are concerned with producing and fabricating materials to meet service requirements as predicted by these stress analyses. This necessarily involves an understanding of the relationships between the microstructure (i.e., internal features) of materials and their mechanical properties. Materials are frequently chosen for structural applications because they have desirable combinations of mechanical characteristics.

2.1.1 Stress-Strain Behavior

The degree to which a structure deforms or strains depends on the magnitude of an imposed stress. For most metals that are stressed in tension and at relatively low levels, stress and strain are proportional to each other through the relationship.

$$\sigma = E \times \varepsilon \tag{2.1}$$

This is known as Hooke's law, and the constant of proportionality E [GPa] or [psi] is the modulus of elasticity, or Young's modulus. For most typical metals the magnitude of this modulus ranges between 45 [GPa] (6.5 x 10^6 [psi]), for magnesium, and 407 [GPa] (59 x 10^6 [psi]), for tungsten. The moduli of elasticity are slightly higher for ceramic materials, which range between about 70 and 500 [GPa] (10 x 10^6 and 70 x 10^6 [psi]). Polymers have modulus

values that are smaller than both metals and ceramics, and which lie in the range 0.007 and 4 [GPa] (10^3 and 0.6 x 10^6 [psi]).

Deformation in which stress and strain are proportional is called elastic deformation; a plot of stress (ordinate) versus strain (abscissa) results in a linear relationship, as shown in Figure 2.1. The slope of this linear segment corresponds to the modulus of elasticity E. This modulus may be thought of as stiffness, or a material's resistance to elastic deformation. The greater modulus, produce stiffer the material or the smaller elastic strains that results from the application of a given stress. The modulus is an important design parameter used for computing elastic deflections.

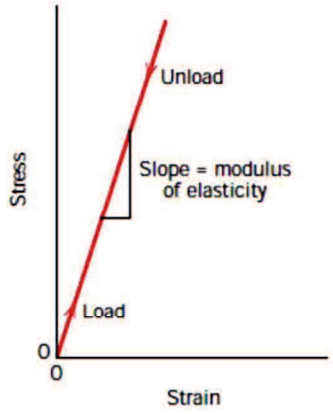

Figure 2.1. Stress-strain diagrams

For nonlinear behavior material, either tangent or secant modulus is normally used. Tangent modulus is taken as the slope of the stress–strain curve at some specified level of stress, while secant modulus represents the slope of a secant drawn from the origin to some given point of the stress-strain curve. The determination of these moduli is illustrated in Figure 2.2.

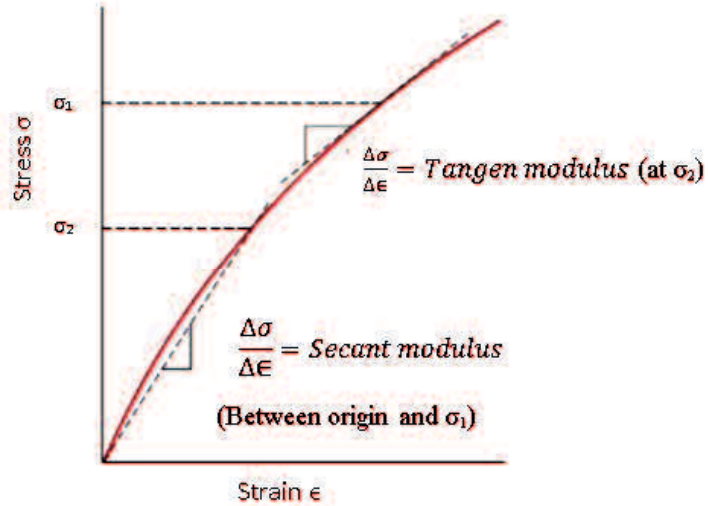

Figure 2.2. Stress-strain diagram of non-linear behavior

2.1.2 Elasticity of Material

When a tensile stress is imposed on virtual materials, an elastic elongation and accompanying strain ϵ_z result in the direction of the applied stress (arbitrarily taken to be the z direction), as indicated in Figure 2.3.

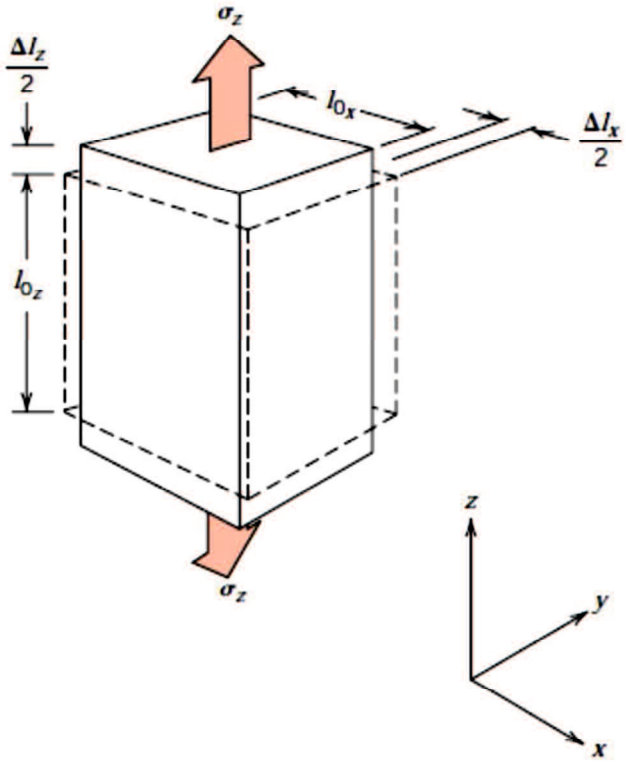

Figure 2.3. Axial deformation and lateral contraction response in tensile stress.

As a result of this elongation there will be constrictions in the lateral (x and y) directions perpendicular to the applied stress; from these contractions, the compressive strains ϵ_x and ϵ_y may be determined. If the applied stress is uniaxial (only in the z direction), and the material is isotropic, then $\epsilon_x = \epsilon_y$. Parameter termed Poisson's ratio is defined as the ratio of the lateral and axial strains.

$$\nu = \frac{\epsilon_x}{\epsilon_z} = -\frac{\epsilon_y}{\epsilon_z} \tag{2.2}$$

The negative sign is included in the expression so that will always be positive, since ϵ_x and ϵ_z will always be of opposite sign. Theoretically, Poisson's ratio for isotropic materials should be 1/4; furthermore, the maximum value for ν (or that value for which there is no net volume change) is 0.50. For many metals and other alloys, values of Poisson's ratio range between 0.25 and 0.35. For isotropic materials, shear and elastic moduli are related to each

other and to Poisson's ratio according to (2.3). In most metals G is about 0.4E; thus, if the value of one modulus is known, the other may be approximated.

$$E = 2G(1 + v) \tag{2.3}$$

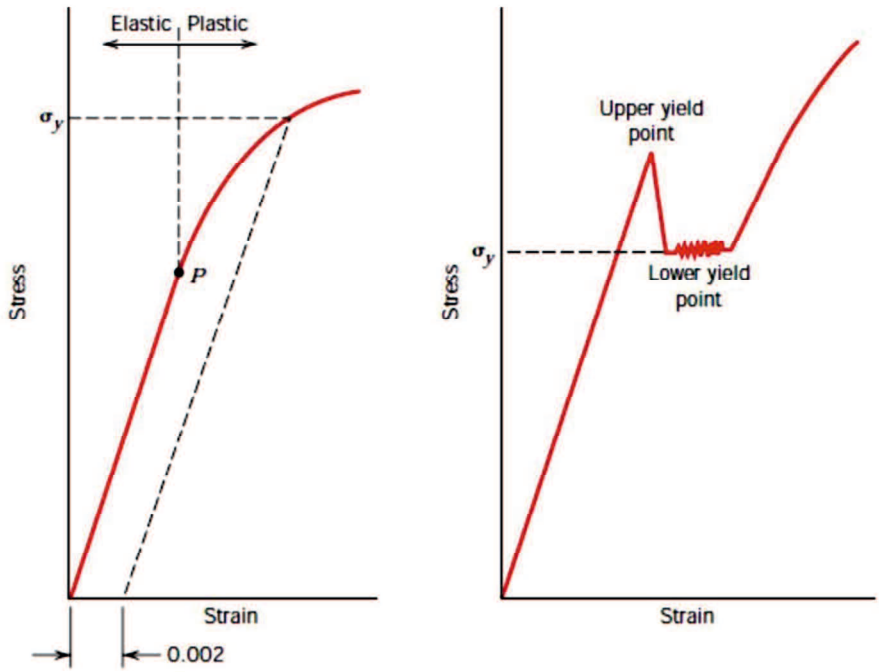

(a). Elastic and plastic region. (b). Yield phenomenon.

Figure 2.4. Elastic and plastic region in stress-strain curve.

Most structures are designed to ensure that only elastic deformation will result when a stress is applied. It is therefore desirable to know the stress level at which plastic deformation begins, or where the phenomenon of yielding occurs. For metals that experience this gradual elastic–plastic transition, the point of yielding may be determined as the initial departure from linearity of the stress–strain curve; this is sometimes called the proportional limit, as indicated by point P, in Figure 2.4 (a). In such cases the position of this point may not be determined precisely. As a consequence, a convention has been established wherein a straight line is constructed parallel to the elastic portion of the stress–strain curve at some specified strain offset, usually 0.002. The stress corresponding to the intersection of this line and the stress–strain curve as it bends over in the plastic region is defined as the yield strength σ_y, the units of yield strength are [MPa] or [psi].

Some steels and other materials exhibit the tensile stress–strain behavior as shown in Figure 2.4 (b). The elastic–plastic transition is very well defined and occurs abruptly in what

is termed a yield point phenomenon. At the upper yield point, plastic deformation is initiated with an actual decrease in stress. Continued deformation fluctuates slightly about some constant stress value, termed the lower yield point; stress subsequently rises with increasing strain. For metals that display this effect, the yield strength is taken as the average stress that is associated with the lower yield point, since it is well defined and relatively insensitive to the testing procedure. Thus, it is not necessary to employ the strain offset method for these materials. The magnitude of the yield strength for a metal is a measure of its resistance to plastic deformation. Yield strengths may range from 35 [MPa] (5000 [psi]) for low-strength aluminum to over 1400 [MPa] (200,000 [psi]) for high-strength steels.

2.1.3 Ductility

Ductility is another important mechanical property. It is a measure of the degree of plastic deformation that has been sustained at fracture. A material that experiences very little or no plastic deformation upon fracture is termed brittle. The tensile stress–strain behaviors for both ductile and brittle materials are schematically illustrated in Figure 2.5. Ductility may be expressed quantitatively as either percent elongation or percent reduction in area. The percent elongation %EL is the percentage of plastic strain at fracture.

$$\%EL = \left(\frac{l_f - l_0}{l_0}\right) \times 100 \qquad (2.4)$$

Where l_f is the fracture length and l_0 is the original gauge length as above. A significant proportion of the plastic deformation at fracture is confined to the neck region; the magnitude of *%E*L will depend on specimen gauge length. The shorter, the greater is the fraction of total elongation from the neck and, consequently, the higher the value of *%EL*. Therefore, l_0 should be specified when percent elongation values are cited; it is commonly 50 [mm]. Percent reduction in area *%RA* is defined as.

$$\%RA = \left(\frac{A_0 - A_f}{A_0}\right) \times 100 \qquad (2.5)$$

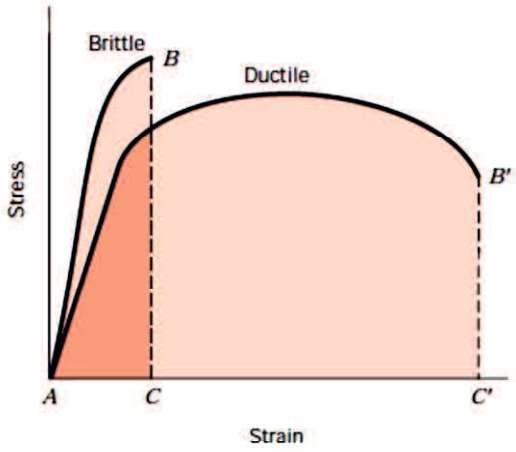

Figure 2.5. Comparison curve for brittle and ductile material.

Where A_0 is the original cross-sectional area and A_f is the cross-sectional area at the point of fracture. Percent reductions in area values are independent of both l_0 and A_0. Furthermore, for a given material the magnitudes of %EL and %RA will in general be different. Most metals possess at least a moderate degree of ductility at room temperature; however, some become brittle as the temperature is lowered.

2.1.4 Resilience

Resilience is the capacity of a material to absorb energy when it is deformed elastically and then, upon unloading, to have this energy recovered. The associated property is the modulus of resilience U_r, which is the strain energy per unit volume required to stress a material from an unloaded state up to the point of yielding. Computationally, the modulus of resilience for a specimen subjected to a uniaxial tension test is just the area under the engineering stress–strain curve taken to yielding (Figure 2.6).

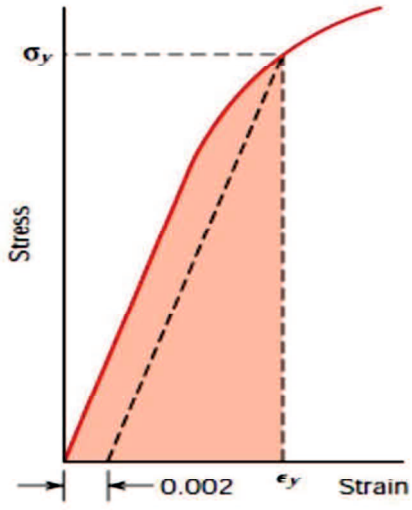

Figure 2.6. Modulus of resilience.

$$U_r = \int_0^{\epsilon_y} \sigma \, d \in \tag{2.6}$$

Assuming a linear elastic region

$$U_r = \frac{1}{2}\sigma_y \epsilon_y \tag{2.6a}$$

In which ϵ_y is the strain at yield point. The units of resilience are the product of the units from each of the two axes of the stress–strain plot. For SI units, this is joules per cubic meter [J/m^3], equivalent to [Pa], whereas with Customary U.S. units it is inch-pounds force per cubic inch [in.lbf/in^3] equivalent to [psi]. Both joules and inch-pounds force are units of energy, and thus this area under the stress–strain curve represents energy absorption per unit volume (in cubic meters or cubic inches) of material.

2.1.5 Toughness

Toughness is a mechanical term that is used in several contexts; loosely speaking, it is a measure of the ability of a material to absorb energy up to fracture. Specimen geometry as well as the manner of load application is important in toughness determinations. For dynamic (high strain rate) loading conditions and when a notch (or point of stress concentration) is present, notch toughness is assessed by using an impact test. Furthermore, fracture toughness is a property indicative of a material's resistance to fracture when a crack is present

For the static (low strain rate) situation, toughness may be ascertained from the results of a tensile stress–strain test. It is the area under the stress-strain curve up to the point of fracture. The units for toughness are the same as for resilience (i.e., energy per unit volume of material). For a material to be tough it must display both strength and ductility; and often, ductile materials are tougher than brittle ones. This is demonstrated in Figure 2.5, in which the stress–strain curves are plotted for both material types. Hence, even though the brittle material has higher yield and tensile strengths, it has a lower toughness than the ductile one, by virtue of lack of ductility; this is deduced by comparing the areas ABC and AB'C' in Figure 2.5.

2.1.6 True Stress and Strain

From Figure 2.7, the decline in the stress necessary to continue deformation past the maximum, point M, seems to indicate that the metal is becoming weaker. This is not at all the case; as a matter of fact, it is increasing in strength. However, the cross-sectional area is

decreasing rapidly within the neck region, where deformation is occurring. This results in a reduction in the load-bearing capacity of the specimen. The stress, as computed from equation (2.1), is on the basis of the original cross-sectional area before any deformation, and does not take into account this diminution in area at the neck.

Sometimes it is more meaningful to use a true stress–true strain scheme. True stress σ_T is defined as the load F divided by the instantaneous cross-sectional area A_i over which deformation is occurring (i.e., the neck, past the tensile point).

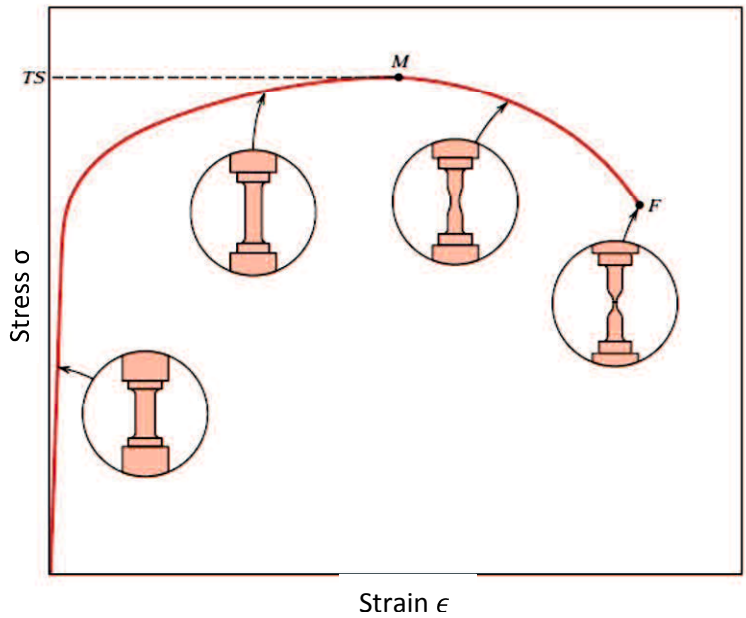

Figure 2.7. Neckıng at tensile test.

$$\sigma_T = {}^{F}/_{A_i} \tag{2.7}$$

Furthermore, it is occasionally more convenient to represent strain as true strain ϵ_T, defined by:

$$\epsilon_T = ln\frac{l_0}{l_i} \tag{2.8}$$

If no volume change occurs during deformation, that is, if

$$A_i l_i = A_0 l_0 \tag{2.9}$$

$$\sigma_T = \sigma(1+\epsilon) \tag{2.10a}$$

$$\epsilon_T = \ln(1+\epsilon) \tag{2.10b}$$

Equations (2.10a) and (2.10b) are valid only to the onset of necking; beyond this point true stress and strain should be computed from actual load, cross-sectional area, and gauge length measurements.

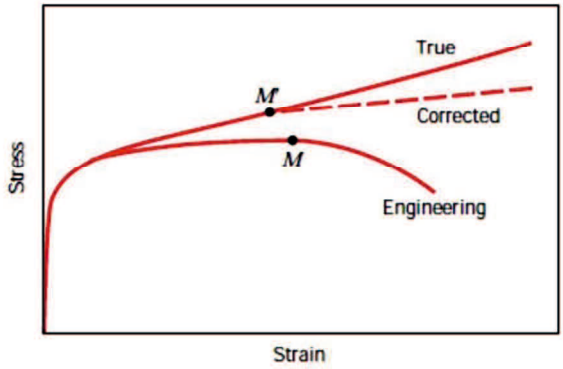

Figure 2.8. Comparison of engineering stress-strain and true stress-strain curve. Points M and M' corresponding to necking begin at material.

2.1.7 Compressive, Shear, and Torsion

Metals may experience plastic deformation under the influence of applied compressive, shear, and torsional loads. The resulting stress–strain behavior into the plastic region will be similar to the tensile counterpart at Figure 2.4 (a). However, for compression, there will be no maximum, since necking does not occur; furthermore, the mode of fracture will be different from that for tension.

2.2 Plasticity of Material

Plasticity theory deals with yielding of materials under complex stress states. It allows one to decide whether a material will yield under a stress state and to determine the shape change that will occur if it does yield. It also allows tensile test data to be used to predict the work hardening during deformation under such complex stress states. These relations are a vital part of computer codes for predicting crashworthiness of automobiles and for designing forming dies.

2.2.1 Yield Criteria

The concern here is to describe mathematically the conditions for yielding under complex stresses. A yield criterion is a mathematical expression of the stress states that will cause yielding or plastic flow. The most general form of a yield criterion is

$$f(\sigma_x, \sigma_y, \sigma_z, \tau_{yz}, \tau_{zx}, \tau_{xy}) = C \qquad (2.11)$$

Where C is a material constant, and f is a mathematical function. For an isotropic material, this can be expressed in terms of principal stresses.

$$f(\sigma_1, \sigma_2, \sigma_3) = C \tag{2.12}$$

The yielding of most solids is independent of the sign of the stress state. Reversing the signs of the stresses has no effect on whether a material yields. This is consistent with the observation that for most materials, the yield strengths in tension and compression are equal. Also with most solid materials, it is reasonable to assume that yielding is independent of the level of mean normal stress σ_m.

$$\sigma_m(\sigma_1 + \sigma_2 + \sigma_3)/3 \tag{2.13}$$

It will be shown later that this is equivalent to assuming that plastic deformation causes no volume change. This assumption of constancy of volume is certainly reasonable for crystalline materials that deform by slip and twinning because these mechanisms involve only shear. With slip and twinning, only the shear stresses are important. With this simplification, the yield criteria must be of the form.

$$f[(\sigma_2 - \sigma_3), (\sigma_3 - \sigma_1), (\sigma_1 - \sigma_2)] = C \tag{2.14}$$

In terms of the Mohr's stress circle diagrams, only the sizes of the circles (not their positions) are of importance in determining whether yielding will occur. In three dimensional stress space (σ_1 vs. σ_2 vs. σ_3), the locus can be represented by a cylinder parallel to the line $\sigma_1 = \sigma_2 = \sigma_3$, as shown in Figure 2.9.

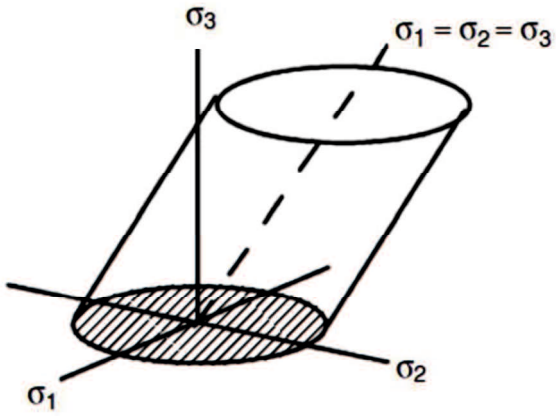

Figure 2.9. Yield state locus of three dimensional stress space.

2.2.2 TRESCA (maximum stress strain criterion)

The simplest yield criterion is one first proposed by Tresca. It states that yielding will occur when the largest shear stress reaches a critical value. The largest shear stress is:

$$\tau_{max} = (\sigma_{max} - \sigma_{min})/2 \tag{2.15}$$

So the Tresca criterion can be expressed as:

$$\sigma_{max} - \sigma_{min} = C \tag{2.16}$$

If the convention is maintained that $\sigma_1 \geq \sigma_2 \geq \sigma_3$, this can be written as:

$$\sigma_1 - \sigma_3 = C \tag{2.17}$$

The constant *C*, can be found by considering uniaxial tension. In a tension test, $\sigma_1 = \sigma_2 = \sigma_3 = 0$, and at yielding $\sigma_1 = Y$, where *Y* is the yield strength. Substituting into equation (2.17), C = Y. Therefore, the Tresca criterion may be expressed as:

$$\sigma_1 - \sigma_3 = Y \tag{2.18}$$

For pure shear, $\sigma_1 = -\sigma_3 = k$, where k is the shear yield strength. Substituting in equation (2.18), $k = Y/2$, so:

$$\sigma_1 - \sigma_3 = 2k = C \tag{2.19}$$

2.2.3 Von Misses Criterion

The effect of the intermediate principal stress can be included by assuming that yielding depends on the root-mean-square diameter of the three Mohr's circles. This is the Von Mises criterion, which can be expressed as:

$$\{[(\sigma_2 - \sigma_3)^2 + (\sigma_3 - \sigma_1)^2 + (\sigma_1 - \sigma_2)^2]/3\}^{1/2} = C \tag{2.20}$$

Note that each term is squared so the convention, $\sigma_1 \geq \sigma_2 \geq \sigma_3$, is not necessary. Again, the material constant, *C*, can be evaluated by considering a uniaxial tension test. At yielding, $\sigma_1 = Y$ and $\sigma_2 = \sigma_3 = 0$. If $[0^2 + (-Y)^2 + Y^2]/3 = C^2$, or $C = (2/3)^{1/3} Y$ is substituted, equation (2.20) becomes.

$$(\sigma_2 - \sigma_3)^2 + (\sigma_3 - \sigma_1)^2 + (\sigma_1 - \sigma_2)^2 = 2Y^2 \tag{2.21}$$

For a state of pure shear, $\sigma_2 = -\sigma_3 = k$ and $\sigma_2 = 0$. Substituting in equation (2.21), $(-k)^2 + [(-k) - k]^2 + k^2 = 2Y^2$, so

$$k = Y/\sqrt{3} \tag{2.22}$$

If one of the principal stresses is zero (plane–stress conditions, $\sigma_z = 0$), equation (2.20) simplifies to ${\sigma_1}^2 + {\sigma_2}^2 - \sigma_1\sigma_2 = Y^2$ which is an ellipse. With further substitution of $\alpha = \sigma_2/\sigma_1$,so

$$\sigma_1 = Y/(1 - \alpha + \alpha^2)^{1/2} \tag{2.23}$$

2.2.4 Flow Rules

When a material yields, the ratio of the resulting strains depends on the stress state that causes yielding. The general relations between plastic strains and the stress states are called the flow rules. They may be expressed as:

$$d\varepsilon_{ij} = d\lambda(\partial f/\partial\sigma_{ij}) \tag{2.24}$$

Where *f* is the yield function corresponding to the yield criterion of concern and $d\lambda$ is a constant that depends on the shape of the stress–strain curve. For the Von Mises criterion, we can write $f = [(\sigma_2 - \sigma_3)^2 + (\sigma_3 - \sigma_1)^2 + (\sigma_1 - \sigma_2)^2]/4$. In this case, equation (2.24) results in:

$$d\varepsilon_1 = d\lambda[2(\sigma_1 - \sigma_2) - 2(\sigma_3 - \sigma_1]/4 = d\lambda[\sigma_1 - (\sigma_2 + \sigma_3)/2] \tag{2.25a}$$

$$d\varepsilon_2 = d\lambda[\sigma_2 - (\sigma_3 + \sigma_1)/2] \tag{2.25b}$$

$$d\varepsilon_3 = d\lambda[\sigma_3 - (\sigma_1 + \sigma_1)/2] \tag{2.25c}$$

These are known as the Levy-Mises equations. Even though dl is not usually known, these equations are useful for finding the ratio of strains that result from a known stress state or the ratio of stresses that correspond to a known strain state.

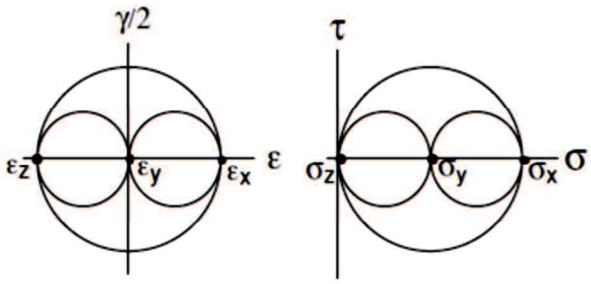

Figure 2.10. Mohr's strain and stress for plane-strain.

2.2.5 Principle of Normality

The flow rules may be represented by the principle of normality. According to this principle, if a normal is constructed to the yield locus at the point of yielding, the strains that result from yielding are in the same ratio as the stress components of the normal. This is illustrated in Figure 2.11. A corollary is that for a σ_1 versus σ_2 yield locus with $\sigma_3 = 0$

$$d\varepsilon_1/d\varepsilon_2 = -\partial\sigma_2/\partial\sigma_1 \tag{2.26}$$

$$\partial\sigma_2/\partial\sigma_1 = \Theta \tag{2.27}$$

Where $\partial\sigma_2/\partial\sigma_1$ is the slope of the yield locus at the point of yielding. It should be noted that equations (2.24) and (2.27) are general and can be used with other yield criteria, including ones formulated to account for anisotropy and pressure dependent yielding.

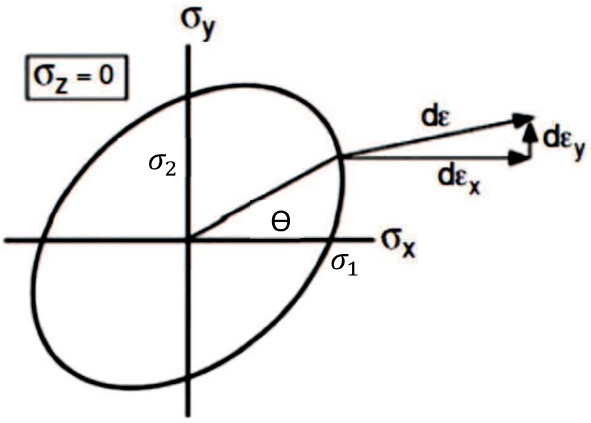

Figure 2.11. Ratio of strain resulting from yielding in same proportion as the component of vector normal to the yield surface.

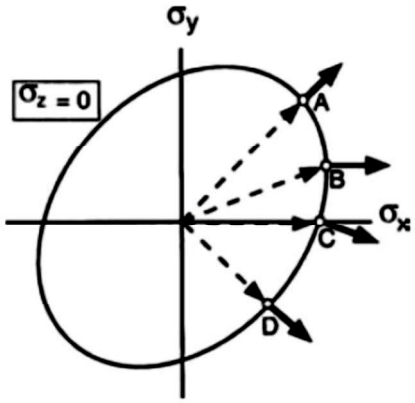

Figure 2.12. Ratio of strain resulting from yielding along several loading path.

Figure 2.12 shows how different shape changes result from different loading paths. The components of the normal at point A – D are:

Normal at A is $d\sigma_y \Big/ d\sigma_x = 1$ so $\varepsilon_y = \varepsilon_x$ (2.28a)

Normal at B has a slope of $d\sigma_y = 0$ so $\varepsilon_y = 0$ (2.28b)

For uniaxial tension at C

Normal at C is $d\sigma_y \Big/ d\sigma_x = -1/2$ so $\varepsilon_y = (-1/2)\varepsilon_x$ (2.28c)

Normal at D is $d\sigma_y \Big/ d\sigma_x = -1$ so $\varepsilon_y = -\varepsilon_x$ (2.28d)

Figure 2.13 is a representation of the normality principle applied to the Tresca criterion. All stress states along a straight edge cause the same ratio of plastic strains. The shape changes corresponding to the corners are ambiguous because it is ambiguous which stress component is σ_{max} and which stress component is σ_{min} . For example, with yielding under biaxial tension, $\sigma_x = \sigma_y$, at $0 \leq \varepsilon_y/\varepsilon_x \leq \infty$.

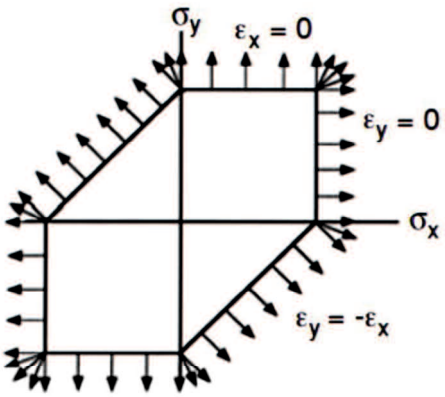

Figure 2.13. Normal principle applied to Tresca yield criterion.

2.2.6 Effect of Strain Hardening on Yield

According to the isotropic hardening model, the effect of strain hardening is simply to expand the yield locus without changing its shape. The stresses for yielding are increased by the same factor along all loading paths. This is the basic assumption that $\sigma = f(\varepsilon)$. The isotropic hardening model can be applied to anisotropic materials. It does not imply that the material is isotropic. An alternative model is kinematic hardening. According to this model, plastic deformation simply shifts the yield locus in the direction of the loading path without changing its shape or size. If the shift is large enough, unloading may actually cause plastic deformation. The kinematic model is probably better for describing small strains after a change in load path. However, the isotropic model is better for describing behavior during large strains after a change of strain path. Figure 2.13 illustrates both models.

2.3 Bending Moments and Deformation Mode

2.3.1 Bending Moments

Bending moments are produced by transverse loads applied to beams. The simplest case is the cantilever beam, widely encountered in balconies, aircraft wings, diving boards etc. The bending moment acting on a section of the beam, due to an applied transverse force, is given by the product of the applied force and its distance from that section. It thus has units of N m. It is balanced by the internal moment arising from the stresses generated. This is given by a summation of all of the internal moments acting on individual elements within the section. These are given by the force acting on the element (stress times area of element) multiplied by its distance from the neutral axis, y.

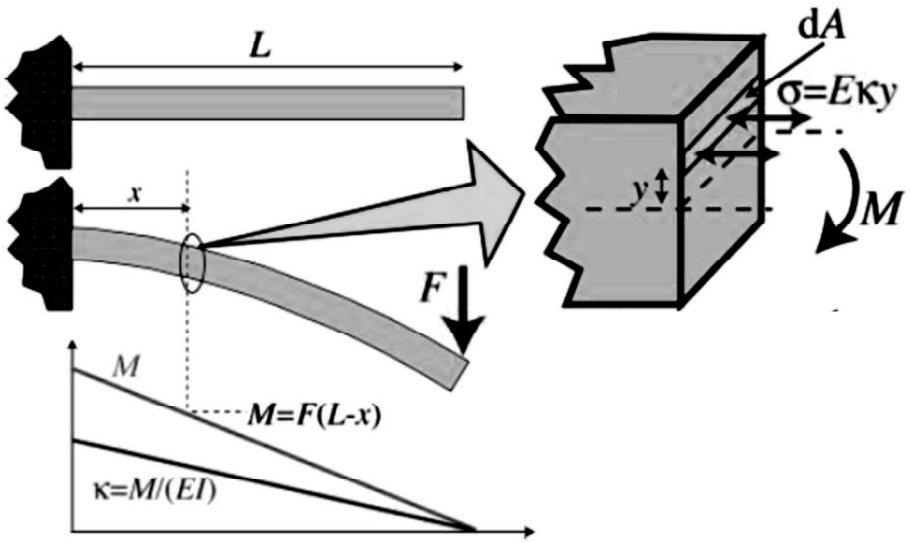

Figure 2.14. Bending moments at isotropic beam.

Therefore, the bending moment M, in a loaded beam can be written in the form

$$M = \int y(\sigma \, dA) \tag{2.29}$$

The concept of the curvature of a beam κ, is central to the understanding of beam bending. The figure below, which refers now to a solid beam, rather than the hollow pole shown in the previous section, shows that the axial strain ε is given by the ratio y/R, equivalently, 1/R (the "curvature", κ) is equal to the through-thickness gradient of axial strain. It follows that the axial stress at a distance y from the Neutral axis of the beam is given by

$$\sigma = E \, \kappa \, y \tag{2.30}$$

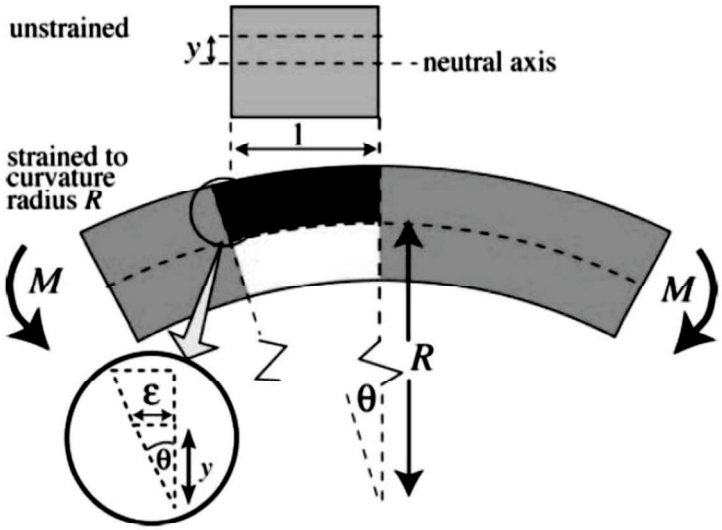

Figure 2.15. Relation between radius of curvature (R), beam curvature (κ), and strain within beam moment.

From equation (2.29) we can substitute (2.30) to

$$M = \int y(E\kappa y dA) = \kappa E \int y^2 dA$$

Where

$$I = \int_0^{y_{max}} y^2 dA$$

$$M = \kappa E I \qquad (2.31)$$

2.3.2 Bending Deformation of Rectangular Tubes

Many researchers have studied bending deformation of rectangular tubes. Those type of bending deformation are similar to bending to cylindrical tubes. A tube with a cross sectional area C1 x C2, thickness t, and length L as shown in figure 2.15 is considered as square tube.

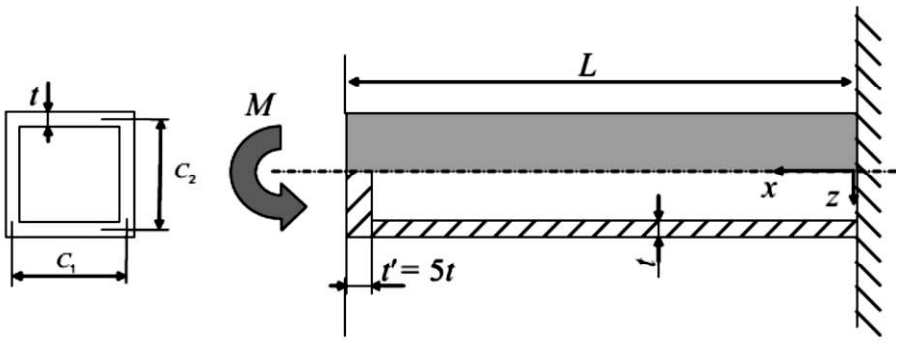

Figure 2.16. Rectangular tube with a pure bending moment.

Deformation due to bending is considered as flattened condition was initially studied by Timoshenko. Figure 2.16 shows bending deformation on cross section area of rectangular tube. The cross section shrinks vertically symmetric, and the vertical distance is the smallest at the center. Distance C_{2f} is shown in the figure and the vertical shrinkage is evaluated by the flattening ratio as defined by.

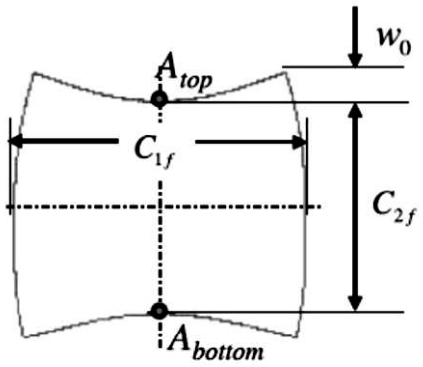

Figure 2.17. Cross sectional area of square tube in bending deformation.

$$\mu = 1 - {}^{C_{2f}}\!/_{C_2} \tag{2.32}$$

Cross sectional flattening in bending deformation of rectangular tube can be evaluated by compared vertical shrinkage and lateral stretch by:

$$\frac{1-{}^{C_{2f}}\!/_{C_2}}{{}^{C_{1f}}\!/_{C_1-1}} = \frac{{C_1}^2(C_1+5C_2)}{4{C_2}^2} \tag{2.33}$$

For bending in square tube where, $C_1 = C_2 = C$ equation (2.33) becomes

$$\frac{1-{}^{C_{2f}}\!/_{C_2}}{{}^{C_{1f}}\!/_{C_1-1}} = 1.5 \tag{2.34}$$

This shows that the amount of vertical shrinkage is 1.5 time the lateral stretch of square tube.

2.3.3 Maximum Bending Moment on Cross Sectional Flattening

In bending deformation of square tube, because of cross-sectional flattening, bending stiffness of the tube decrease and thus the relationship between bending moment and bending curvature become non-linear. The maximum bending moment shows in figure 2.17.

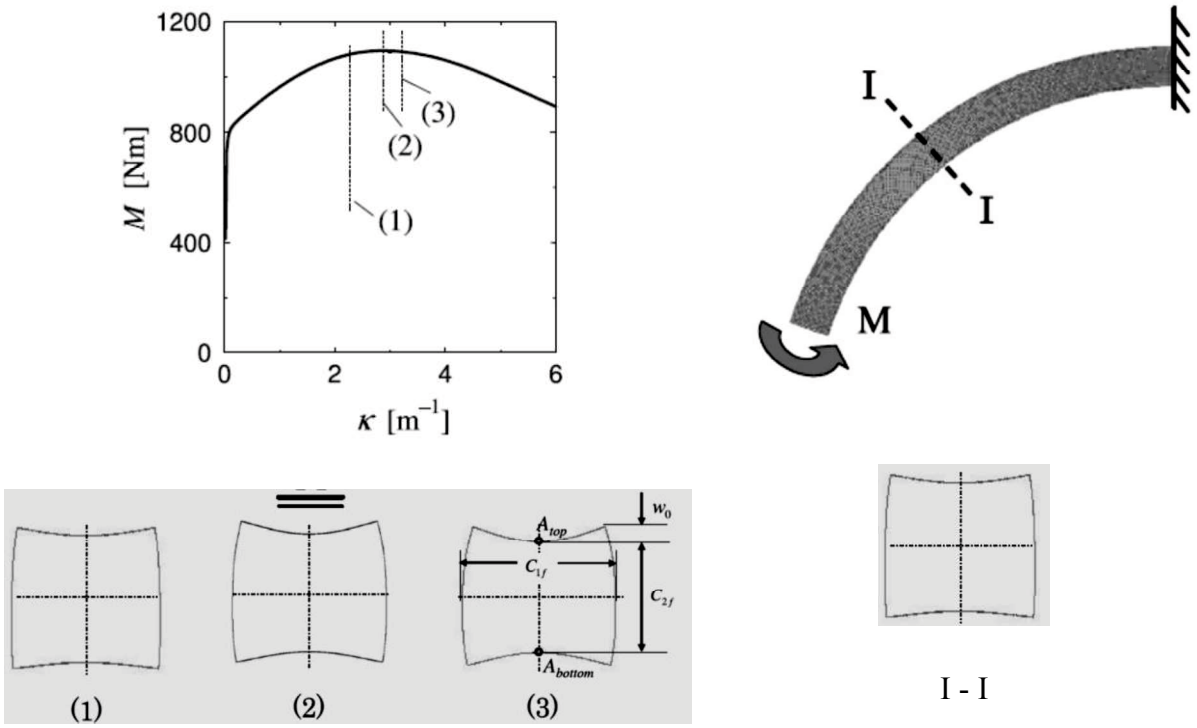

(a). Momen – curvature curve and square tube deformation step.

(b). Deformation of cross section area on square tube at bending.

Figure 2.18. Collapse of square tube due to flattening at bending.

2.4 Axial Compression of Tube

Thin walled structures was involve in various type of automobiles, crash elements and others supporting structures. Behavior of this element under compression was studied in extensive area. Deformation behavior of circular and square shape due to axial compression has many theoretical and experimental studies.

2.4.1 Axial Compression of Circular Tube

Thin walled circular tubes under axial compression are classified into two types:

1. Progressive folding collapse, where wrinkle are identified by local buckling of the tube wall and then the circular tube collapses while standing straight up as local buckles are formed progressively one after another.
2. Global bending/ Euler buckling, where the circular tube flexes and collapses by buckling. For engineering design purposes it is preferable to choose progressive buckling condition.

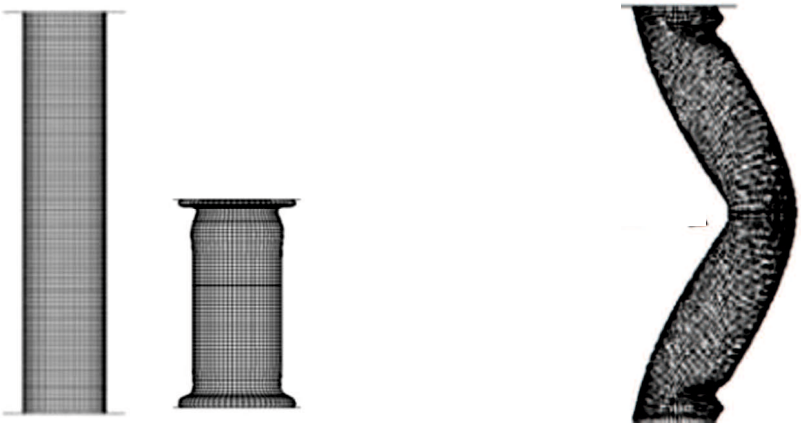

(a). Progressive folding mode. (b). Global buckling mode.

Figure 2.19. Axial compressions mode of circular tubes.

Progressive folding collapse of circular tubes has main features of the compressive force variation. The parameters are widely used: Peak force (P_{peak}), average crushing force (P_{ave}) or force efficiency, and absorbed energy, see figure 2.20.

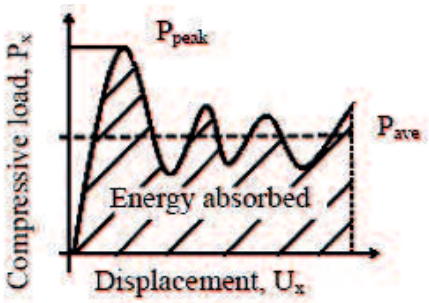

Figure 2.20. Main characteristic axial compressive in progressive folding collapse of circular tubes.

Progressive folding collapse of circular tubes divides into two groups: axisymmetric deformation mode and non-axisymmetric deformation mode. The non-axisymmetric deformation mode is normally found in thin walled circular tubes, while axisymmetric often found in relatively thick walled circular tubes (ordinarily $R/t \leq 40$ in aluminum alloy).

Below is several tubular member collapse characteristic:

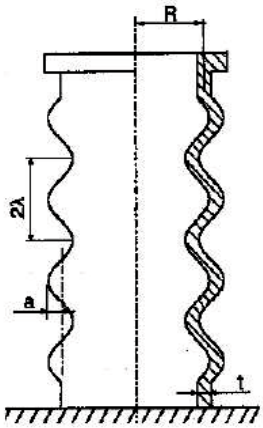

(a). Cylindrical tube with corrugated surface.

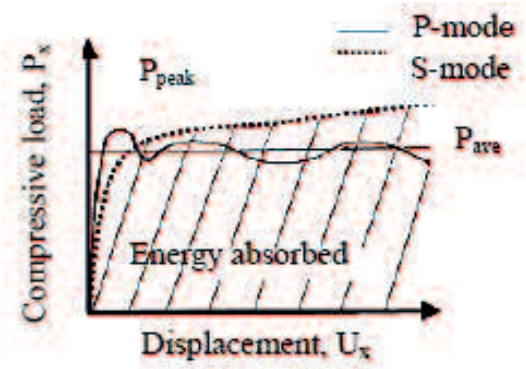

(b). Load – displacement curve for cylindrical corrugated tube.

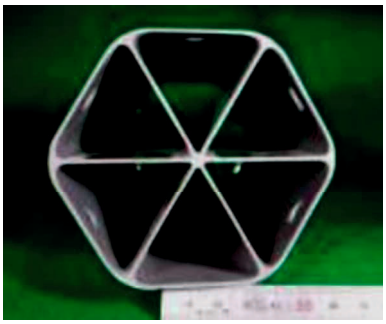

(c). Hexagonal tubes with partition.

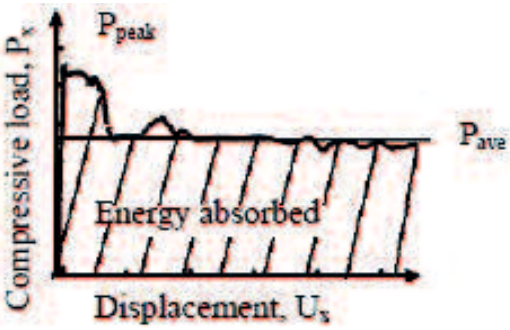

(d). Load – displacement curve for hexagonal tubes with partition.

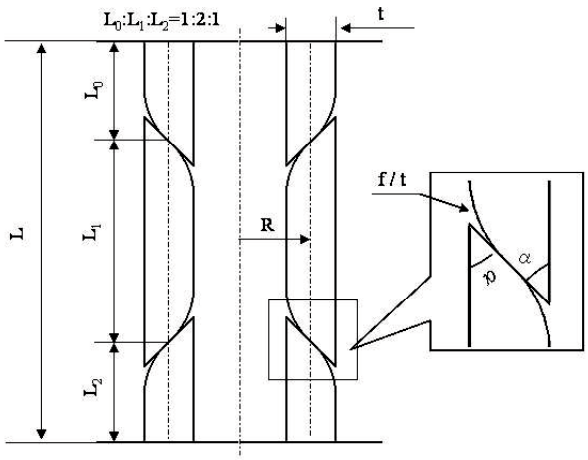

(e). Compress-expand tube.

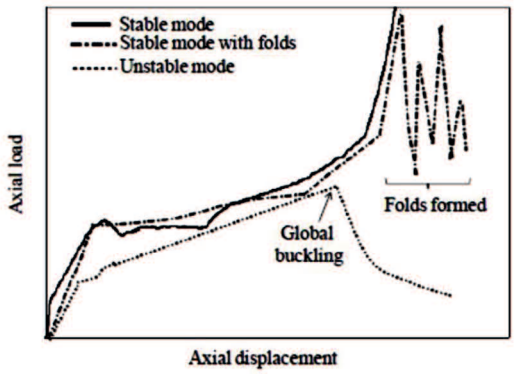

(f). Load – displacement curve for compress-expand tube.

Figure 2.21. Several thin-walled structure tubes characteristic under axial compressive load.

2.4.2 Axial Compression Of Compress-Expand Tube

For the compress–expand member, when subjected to axial loading, three collapse modes have been identified:

a. Axial collapse parallel to the axial axis where compress members penetrate into the expand member with no folds formed.
b. Axial collapse parallel to the axial axis where compress members penetrate into the expand member with folds formed at the end of the penetration.
c. Expand member bends during penetration of compress members.

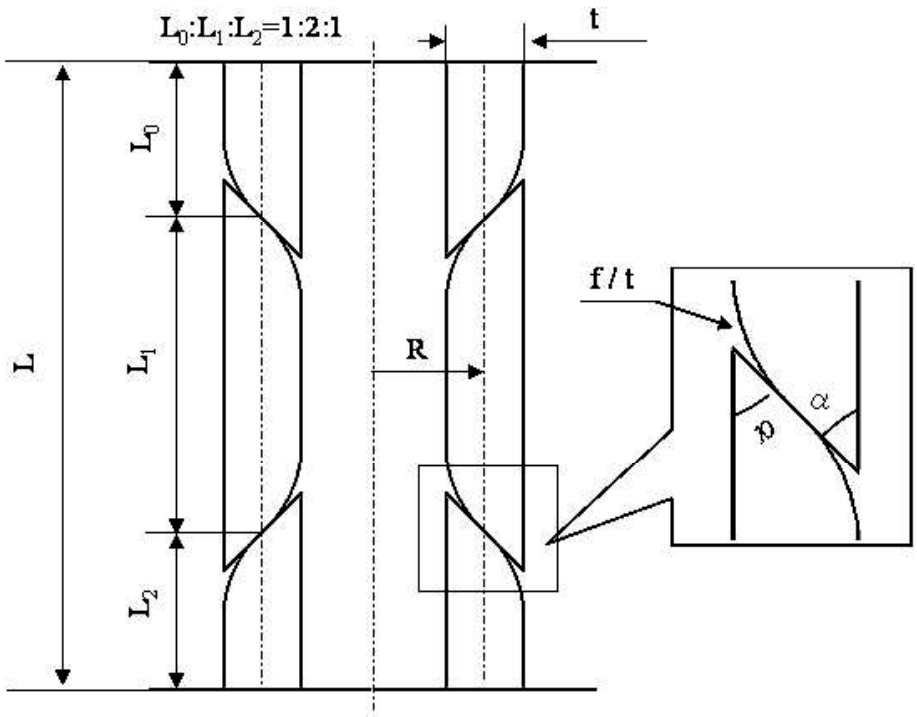

Figure 2.22. Parameter of compress-expand tube.

From the numerical analyses and experiments conducted, the collapse mode of compress-expand member divided into:

(a) Stable mode: axial collapse parallel to the axial axis where compress members penetrate into the expand member with no folds formed.
(b) Stable mode with folds: axial collapse parallel to the axial axis where compress members penetrate into the expand member with folds formed at the end of the penetration.
(c) Unstable mode: expand member bends during penetration of compress members

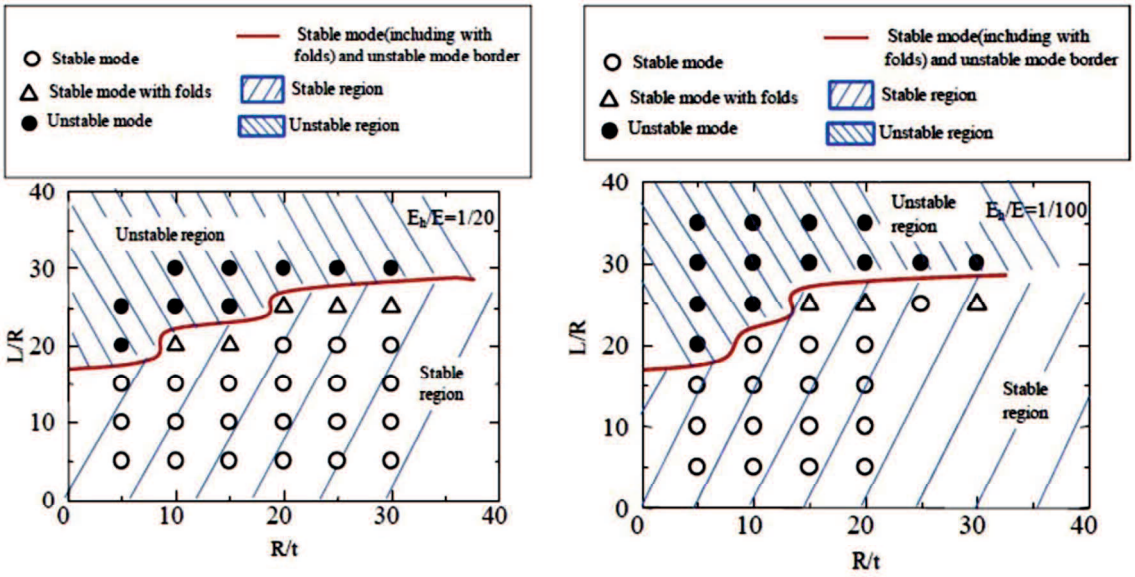

(a). Deformation map hardening ratio (Eh/E=1/20).

(b). Deformation map hardening ratio (Eh/E=1/100).

Figure 2.23 Deformation map of compress-expand tube with work hardening ratio E_h/E=1/20 and E_h/E=1/100.

2.5 Roll-Over Protective Structure (ROPS)

Rollover protection system or rollover protective structure (ROPS) is a system or structure purposed for protects equipment and operators from injuries caused by vehicle overturn or rollover. ROPS involves bars attached to the frame that maintain a space for operator's body when accident happens. Commonly found on heavy equipment, earth moving machineries, construction, agriculture, and mining. ROPS structures are defined by various regulatory. The regulation includes both a strength requirement and energy absorption requirement of the structure.

ROPS was identified based on its number on vertical pillars by;

1. Single-post ROPS

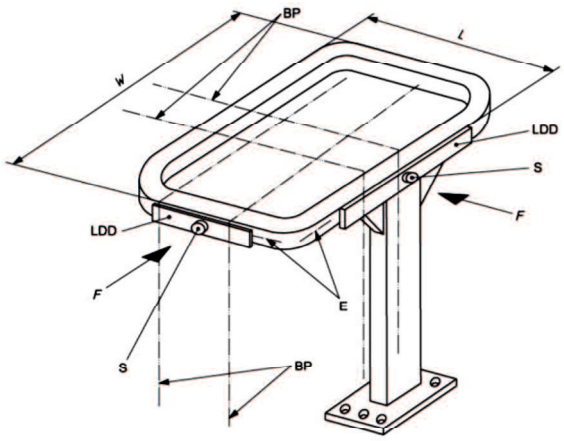

Figure 2.24. Single-post ROPS.

2. Two-post ROPS

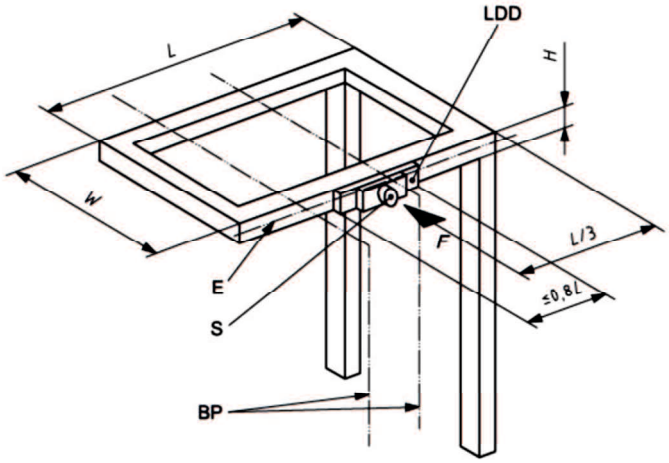

Figure 2.25. Two-post ROPS.

3. Four-post ROPS

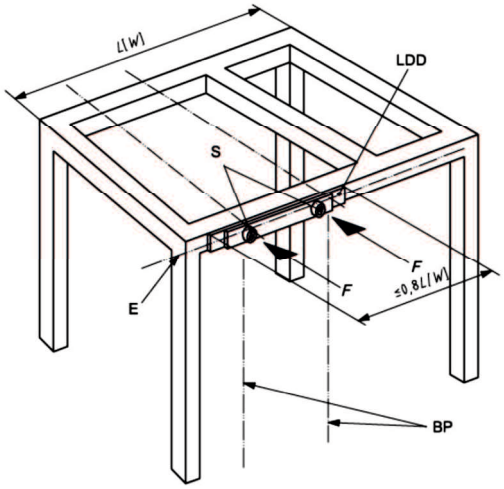

Figure 2.26. Four-post ROPS.

4. Six-post ROPS

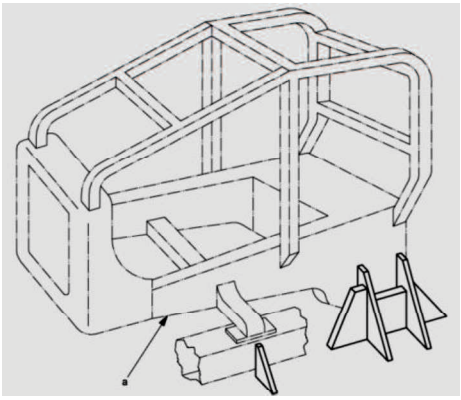

Figure 2.27. Six-post ROPS.

2.6 Finite Element Model

2.6.1 Finite Element Model in MSC MARC

Mentat Graphic User Interface is an interactive computer program that prepares and processes the finite element method. Mentat can process both two- and three-dimensional meshes to do the following:

- Generate and display a mesh
- Generate and display boundary conditions and loadings
- Perform post-processing to generate contour, deformed shape, and time history plots

The data that is processed in MARC system includes:

- Nodal coordinates
- Element connectivity
- Nodal boundary conditions
- Nodal coordinate systems
- Element material properties
- Element geometric properties
- Element loads
- Nodal loads/nonzero boundary conditions
- Element and nodal sets

2.6.2 MARC for Analysis

You can use Marc to perform linear or nonlinear stress analysis in the static and dynamic regimes, to perform heat transfer analysis and electromagnetic analysis. Physical problems in one, two, or three dimensions can be modeled using a variety of elements. These elements include trusses, beams, shells, and solids.

The Marc system contains a series of integrated programs that facilitate analysis of engineering problems. The Marc system consists of the following programs:

- Marc for analysis
- Mentat or Patran for GUI

2.6.3 Material Library

The material library includes many material models that represent most engineering materials. Examples of materials library are:

- Linear elastic material
- Composite material
- Gasket
- Nonlinear material
- Elastomer
- Low tension material
- Soil model
- Nonstructural material
- Etc.

2.6.4 Element Type

The element library contains any geometry under any linear or nonlinear loading conditions. Examples of element library are:

- Truss
- Membrane
- Continuum
- Beam
- Plate
- Shell
- Heat transfer
- Soil analysis
- Fluid analysis
- Incompressible
- Etc.

2.6.5 Solution Procedures for Non-linear System

Nonlinear system contains lots of issues which have been expressed in several solution procedures. Equation systems of convergence controls, singularity ratio, and available solvers for linearized system of equation according to:

1) Newton-Raphson method

The Newton-Raphson method can be used to solve the nonlinear equilibrium equations in structural analysis by considering the following set of equations:

$$K(u)\delta u = F - R(u) \tag{2.35}$$

Where u is the nodal-displacement vector, F is the external nodal-load vector, R is the internal nodal-load vector (following from the internal stresses), and is K the tangent-stiffness matrix. The internal nodal-load vector is obtained from the internal stresses as:

$$R = \sum_{elem} \int_V \beta^T \sigma \, dv \tag{2.36}$$

Both R and K are functions of u . In many cases, F is also a function of u (for example, if F follows from pressure loads, the nodal load vector are a function of the orientation of the structure). The equations suggest that use of the Newton-Raphson method is appropriate. Suppose that the last obtained approximate solution is termed u^i , where ^{i} indicates the iteration number. Equation (2.35) can then be written as:

$$K\left(u_{n+1}^{i-1}\right)\delta u = F - R(u_{n+1}^{i-1}) \tag{2.37}$$

This equation is solved for δu^i and the next appropriate solution is obtained by:

$$\Delta u^i = \Delta u^{i-1} + \delta u^i \; and \; u_{n+1}^i = u_n + \Delta u^i \tag{2.38}$$

Solution of this equation completes one iteration, and the process can be repeated. The subscript n denotes the increment number representing the state t = n . Unless stated otherwise, the subscript n+1 is dropped with all quantities referring to the current state.

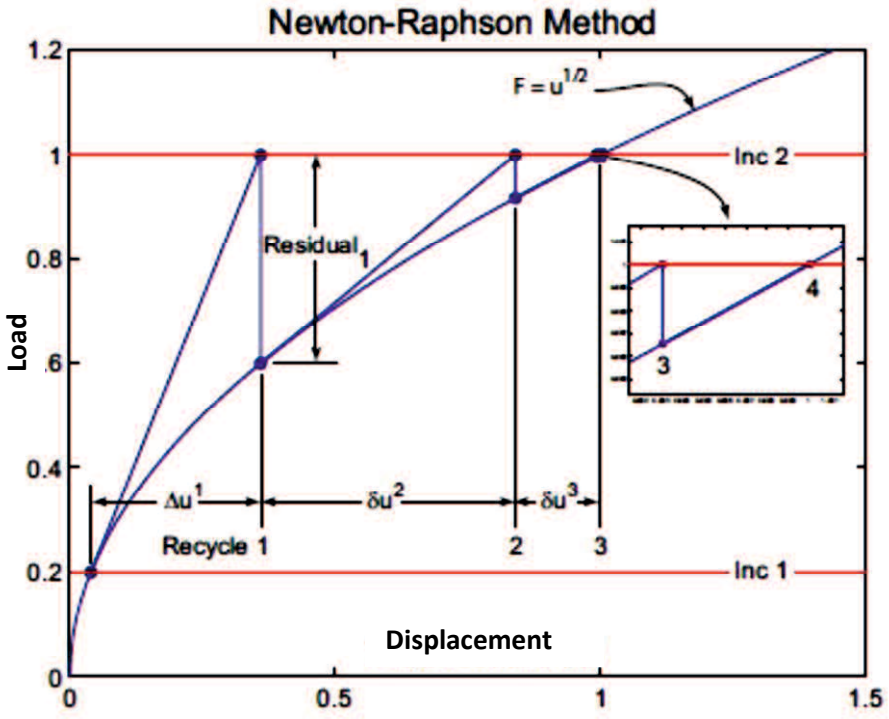

Figure 2.28. Newton-Raphson method curved.

CHAPTER III

SIMULATION ENVIRONMENT SYSTEM

3 1. Rollover Protecting Structures (ROPS) Standard Testing

3.1.1 ISO 3471: 2008

Earth Moving Machinery Roll Over Protecting Structures Laboratory Tests And Performance Requirements.

1. Scope

This document establishes a consistent, repeatable means of evaluating the load-carrying characteristic of ROPS under static loading and prescribes performance requirements of representative specimens under such loading.

2. Normative reference.

The following referenced documents are indispensable for the application of this document. For dated references, only the edition cited applies. For undated references, the latest edition of the referenced document (including any amendments) applies.

- ISO 148-1:2006, Metallic materials — Charpy pendulum impact test (V-notch) — Part 1: Test method
- ISO 898-1:1999, Mechanical properties of fasteners made of carbon steel and alloy steel — Part 1: Bolts, screws and studs
- ISO 898-2:1992, Mechanical properties of fasteners — Part 2: Nuts with specified proof load values — Coarse thread
- ISO 3164:1995, Earth-moving machinery — Laboratory evaluations of protective structures — Specifications for deflection-limiting volume
- ISO 5353:1995, Earth-moving machinery, and tractors and machinery for agriculture and forestry — Seat index point
- ISO 6165:2006, Earth-moving machinery — Basic types — Identification and terms and definitions
- ISO 9248:1992, Earth-moving machinery — Units for dimensions, performance and capacities, and their measurement accuracies

3. Term and definition

(1) Bedplate. A substantially rigid part of the testing fixture to which the machine frame is attached for the purpose of the test.

(2) Boundary plane. Plane defined as the vertical projected plane of the back, side, or knee area of the DLV. The boundary planes are used to determine the load application point.

(3) DLV. Deflection limiting volume, orthogonal approximation of a large, seated, male operator wearing normal clothing and a protective helmet.

(4) Deflection of ROPS. Movement of the ROPS, mounting system and frame section as measured at the load application point (LAP), excluding the effect of any movement of the test fixture(s).

(5) FOPS. Falling-object protective structure, system of structural members arranged in such a way as to provide operators with reasonable protection from falling objects (e.g. trees, rocks, small concrete blocks, and tools).

(6) Head portion of DLV. Upper 270 mm by 330 mm rectangular section of the DLV, whose dimensions are in accordance with ISO 3164.

(7) LSGP. Lateral simulated ground plane, plane defined as where the machine comes to rest on its side, where the plane is 15° away from the DLV. It is created by rotating a vertical plane parallel to the machine's longitudinal centerline about a horizontal line through the outermost point of the upper ROPS member, to which the lateral load is applied (see Figure 3.12). The LSGP is established on an unloaded ROPS and moves with the member to which the load is applied while maintaining its 15° angle with respect to the vertical.

(8) LDD. Load distribution device, device used to prevent localized penetration of the ROPS members at the load application point (LAP).

(9) LAP. Load application point, point (or a point within a defined range) on the ROPS structure at which the test load force (F) is applied.

(10) Machine frame. Metallic main chassis or main metallic load-bearing member(s) of the machine that extend(s) over a major section of the machine and upon which the ROPS is directly mounted.

(11) Mounting system. All brackets, welding, fasteners or other devices whose function is to attach the ROPS to the machine frame.

(12) Representative specimen. ROPS, mounting system and machine frame (complete or partial) used for test purposes that is within the range of material and manufacturing variances designated by the manufacturer’s production specifications.

(13) ROPS. Roll-over protective structure, system of structural members whose primary purpose is to reduce the possibility of a seat-belted operator being crushed in the event of a machine roll-over.

(14) ROPS structural member. Metallic member designed to withstand an applied force or absorb energy.

(15) SGP. Simulated ground plane, plane simulating the flat ground surface on which a machine is assumed to come to rest after rolling over.

(16) S. Socket, test component that allows unrestricted point loading of the load distribution device (LDD).

(17) Vertical projection of DLV. Cross-sectional area of the column formed by vertically projecting the outside corners of the deflection limiting volume (DLV), with dimensions according to ISO 3164, excluding the foot section.

(18) VSGP. Vertical simulated ground plane, plane defined by contact with a top cross-member of the ROPS and that front or rear part of the machine capable of supporting an overturned machine.

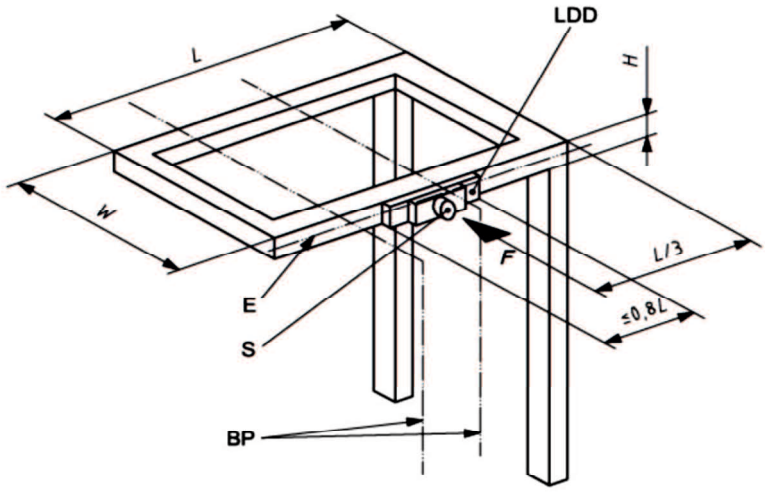

(a). Position load distribution device at two post ROPS.

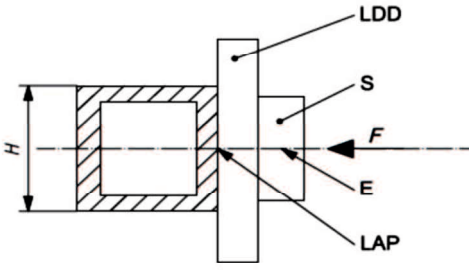

(b). Detail Load distribution device.

Figure 3.1. Lateral load application point (LAP) of two post ROPS.

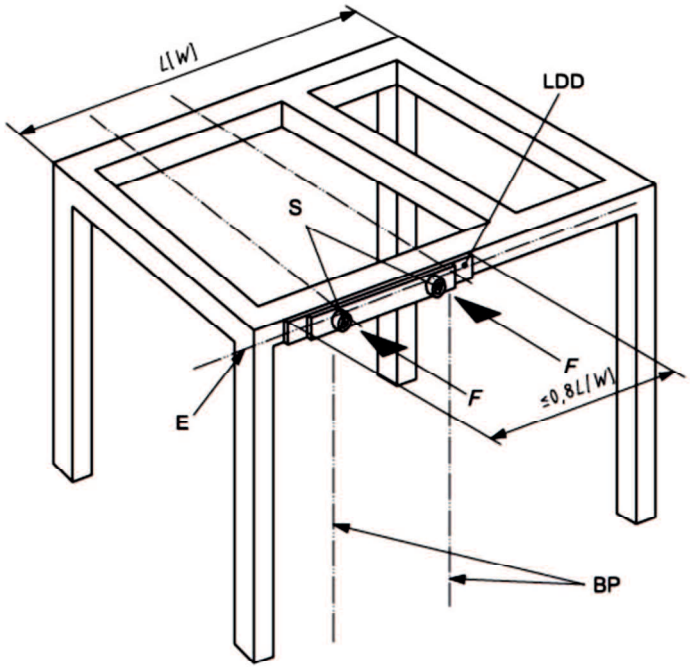

Figure 3.2. Lateral load application point (LAP) of four post ROPS.

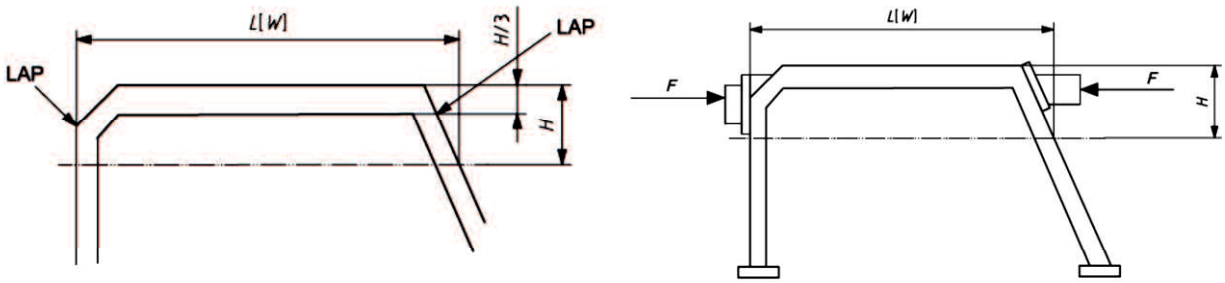

(a). Curved ROPS

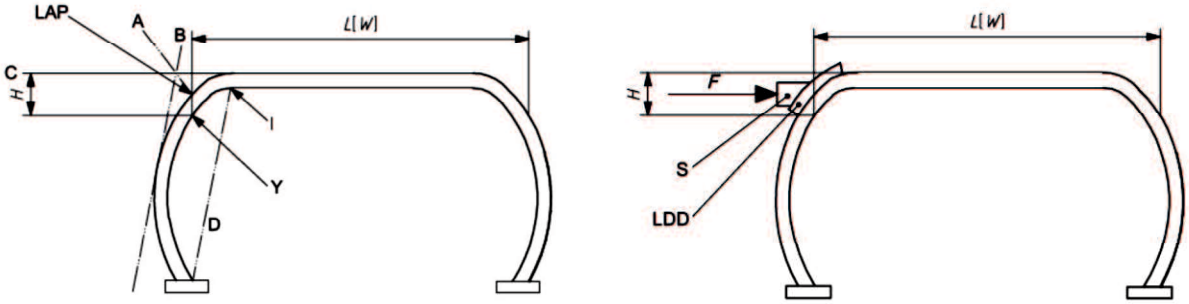

(b). Shaped ROPS

Figure 3.3. Lateral load application point (LAP) of curved and shaped ROPS.

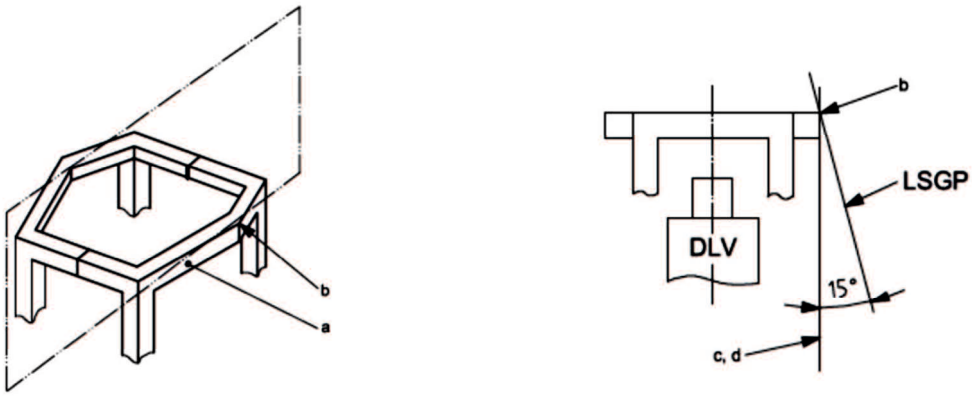

(a). Middle point of DLV (b). Slope deflection of LSGP to DLV

Figure 3.4. Determination of lateral simulated ground plane (LSGP).

3 2. Test Method and Test Facilities

1. General requirements. The requirements are force resistance in the lateral, vertical and longitudinal directions, and energy absorption in the lateral direction. There are limitations on deflections under the lateral, vertical and longitudinal loading.
2. Instrumentation. Systems used to measure mass, force and deflection shall be in accordance with ISO 9248, except that the force and deflection measurement capability shall be within $\pm 5\%$ of the maximum values.
3. Test facilities. Fixtures shall be adequate to secure the representative specimen to a bedplate and to apply the required lateral, vertical and longitudinal loads as determined by the formulae given in Table 3.1.

Table 3.1. Force and energy equation.

Machine mass [m] (kg)	**Lateral load [F] (N)**	**Lateral load energy [U] (J)**	**Vertical load [F] (N)**	**Longitudinal load [F] (N)**
1) Crawler earth-moving machine: dozer, loader, pipelayer and trencher type				
$700 < m \leqslant 4\,630$ $4\,630 < m \leqslant 59\,500$ $m > 59\,500$	$6m$ $70\,000\,(m/10\,000)^{1,2}$ $10m$	$13\,000\,(m/10\,000)^{1,25}$ $13\,000\,(m/10\,000)^{1,25}$ $2{,}03m$	19.61m	$4{,}8m$ $56\,000\,(m/10\,000)^{1,2}$ $8m$
2) Grader				
$700 < m \leqslant 2\,140$ $2\,140 < m \leqslant 38\,010$ $m > 38\,010$	$6m$ $70\,000\,(m/10\,000)^{1,1}$ $8m$	$15\,000\,(m/10\,000)^{1,25}$ $15\,000\,(m/10\,000)^{1,25}$ $2{,}09m$	19.61m	$4{,}8m$ $56\,000\,(m/10\,000)^{1,1}$ $6{,}4m$
3) Wheeled earth-moving machine: loader, tractor-dozer, pipelayer, landfill compactor, skid-steer loader, backhoe loader and trencher type				

$700 < m \leqslant 10\,000$ $10\,0000 < m \leqslant 128\,600$ $m > 128\,600$	$6m$ $60\,000\,(m/10\,000)^{1,2}$ $10m$	$12\,500\,(m/10\,000)^{1,25}$ $12\,500\,(m/10\,000)^{1,25}$ $2{,}37m$	19.61m	$4{,}8m$ $48\,000\,(m/10\,000)^{1,2}$ $8m$
4) Tractor section of combined earth-moving machine: tractor scraper, articulated frame dumper				
$700 < m \leqslant 1\,010$ $1\,010 < m \leqslant 32\,160$ $m > 32\,160$	$6m$ $95\,000\,(m/10\,000)^{1,2}$ $12m$	$20\,000\,(m/10\,000)^{1,25}$ $20\,000\,(m/10\,000)^{1,25}$ $2{,}68m$	19.61m	$4{,}8m$ $76\,000\,(m/10\,000)^{1,2}$ $9{,}6m$
5) Roller [a]				
$700 < m \leqslant 10\,000$ $10\,000 < m \leqslant 53\,780$ $m > 53\,780$	$5m$ $50\,000\,(m/10\,000)^{1,2}$ $7m$	$9\,500\,(m/10\,000)^{1,25}$ $9\,500\,(m/10\,000)^{1,25}$ $1{,}45m$	19.61m	$4m$ $40\,000\,(m/10\,000)^{1,2}$ $5{,}6m$
6) Rigid frame dumper — Excluding dump body [b]				
$700 < m \leqslant 1\,750$ $1\,750 < m \leqslant 22\,540$ $22\,540 < m \leqslant 58\,960$ $58\,960 < m \leqslant 111\,660$ $m > 111\,660$	$6m$ $85\,000\,(m/10\,000)^{1,2}$ $10m$ $413\,500\,(m/10\,000)^{0,2}$ $6m$	$15\,000\,(m/10\,000)^{1,25}$ $15\,000\,(m/10\,000)^{1,25}$ $1{,}84m$ $61\,450\,(m/10\,000)^{0,32}$ $1{,}19m$	19.61m	$4{,}8m$ $68\,000\,(m/10\,000)^{1,2}$ $8m$ $330\,800\,(m/10\,000)^{0,2}$ $4{,}8m$
7) Rigid frame dumper — Including dump body [c]				
$700 < m \leqslant 10\,000$ $10\,000 < m \leqslant 21\,610$ $21\,610 < m \leqslant 93\,900$ $93\,900 < m \leqslant 113\,860$ $m > 113\,860$	$6m$ $60\,000\,(m/10\,000)^{1,2}$ $7m$ $420\,000\,(m/10\,000)^{0,2}$ $6m$	$6\,000\,(m/10\,000)^{1,25}$ $6\,000\,(m/10\,000)^{1,25}$ $0{,}73m$ $16\,720\,(m/10\,000)^{0,63}$ $0{,}68m$	19.61m	$4{,}8m$ $48\,000\,(m/10\,000)^{1,2}$ $5{,}6m$ $336\,000\,(m/10\,000)^{0,2}$ $4{,}8m$
8) Rigid frame dumper — Combination of ROPS and dump body [d]				
$700 < m \leqslant 10\,000$ $10\,000 < m \leqslant 21\,610$ $21\,610 < m \leqslant 93\,900$ $93\,900 < m \leqslant 113\,860$ $m > 113\,860$	$3{,}6m$ $36\,000\,(m/10\,000)^{1,2}$ $4{,}2m$ $252\,000\,(m/10\,000)^{0,2}$ $3{,}6m$	$3\,600\,(m/10\,000)^{1,25}$ $3\,600\,(m/10\,000)^{1,25}$ $0{,}44m$ $10\,000\,(m/10\,000)^{0,63}$ $0{,}41m$	11.77m	$2{,}9m$ $28\,800\,(m/10\,000)^{1,2}$ $3{,}4m$ $202\,000\,(m/10\,000)^{0,2}$ $2{,}9m$

a. Mass m excludes mass of loosely contained ballast, which can separate from machine in the event of a roll-over.

b. Mass m includes machine mass but not dump body or payload mass.

c. Mass m includes machine and dump body mass but not payload mass. The body sections on which the loads are applied shall totally cover the vertical projection of the DLV. Lateral and vertical LAP shall be on the body overhang portion in the same relative locations outlined for separate ROPS. Longitudinal load shall be applied at that face producing the greatest change of deformation toward the operator.

d. Mass m includes machine and dump body mass but not payload mass. Lateral, longitudinal or vertical loading of the ROPS and/or body need not be applied simultaneously to both members of a combination. The only limitation on the order of the six loadings is that the vertical loading of members shall be applied after the lateral loading and the longitudinal loading of members shall be applied after the vertical loading.

Table 3.2. Force and energy equation according to cab's height.

	With low cab riser up to 500mm	With medium height greater than 500 up to 1300mm cab riser	With greater than 1300mm high cab riser (TOPS)
Lateral load energy U_x [J]	$13000\ (M/10000)^{1.25}$	$13000\ (M/10000)^{1.25}$	$13000\ (M/10000)^{1.25}$
Lateral load force F_x [N]	$35000\ (M/10000)^{1.2}$	$50000\ (M/10000)^{1.2}$	$50000\ (M/10000)^{1.2}$

3 3. Test Loading Procedures

A. General requirements

1. All LAP shall be determined and marked on the structure before any loading is applied.
2. The loads shall be calculated according to Table 3.1 and the loading sequence shall be lateral, vertical and longitudinal.
3. No straightening or repair is permitted during or between loading sequences.
4. The load shall be applied through S and LDD. The socket shall provide unrestricted movement of the ROPS during the loading process. LDD is used to prevent localized penetration of ROPS structural members. S and LDD shall not impede rotation of the ROPS.
5. LDD shall not contact a ROPS structural member beyond H.

B. Lateral loading

1. LDD shall span L, in cases where no rear cross-member exists that would be capable of transferring the load without buckling. In all other cases, the device shall not distribute the load over a length greater than 80 % of the ROPS length L. For the length, L, of curved surfaces.
2. For roll bar ROPS, the LAP shall be on the same plane with the upper lateral cross-member.
3. For all other one-post or two-post ROPS, the LAP shall be dictated by the length, L, and the vertical projection of the closest side or edge of the DLV. The LAP shall not be within a distance L/3 measured from the rear outside face of the ROPS structure. If the L/3 point is situated between the back face of the ROPS at the post side and the intersection of the DLV boundary plane (BP) closest to the post(s) with the lateral

structural member, the LAP shall be moved away from the post side until it reaches at least the BP of the DLV.

4. For a ROPS with more than two posts, the LAP shall be located between vertical projections of the front and rear BP of the DLV.
5. Where the operator's seat is off the machine longitudinal center-line, the loading shall be against the external side of the lateral structural member closest to the seat. Where the operator's seat is on the machine longitudinal center-line, if the ROPS structure and mounting are such that different force-deflection results are likely by loading from left or right, the side that is loaded shall be that which will place the most severe loading requirements on the representative specimen.
6. The initial direction of the loading shall be horizontal and perpendicular to a vertical plane through the machine longitudinal center-line. As loading continues, representative specimen deformations can cause the direction of loading to change. This is permissible.
7. The loading may be considered static if the rate of deflection at the LAP is not greater than 5 mm/s. The values of force and deflection, at the LAP, shall be recorded at deflection increments no greater than 15 mm. The loading is to continue until the force and energy levels in accordance with Table 1 have been reached. The method of calculating the energy, U. The measured deflection used in calculating the energy is that of the ROPS along the line of the applied force. Deflection of the ROPS mounting system and machine frame may be included in the total deflection; however, deflection of all test fixture arrangements shall be excluded.

3 4. Finite Element Analysis

3.4.1 Finite Element of Cab Frame Model

This study using several model of finite element according to:

Table 3.3 Finite element properties of cab frame

Meshing size	10 x 10 [mm]
Meshing type	3D Shell, Quadrilateral, Isotropic
Simulation type	Static
Increment/ step size	2 [mm]

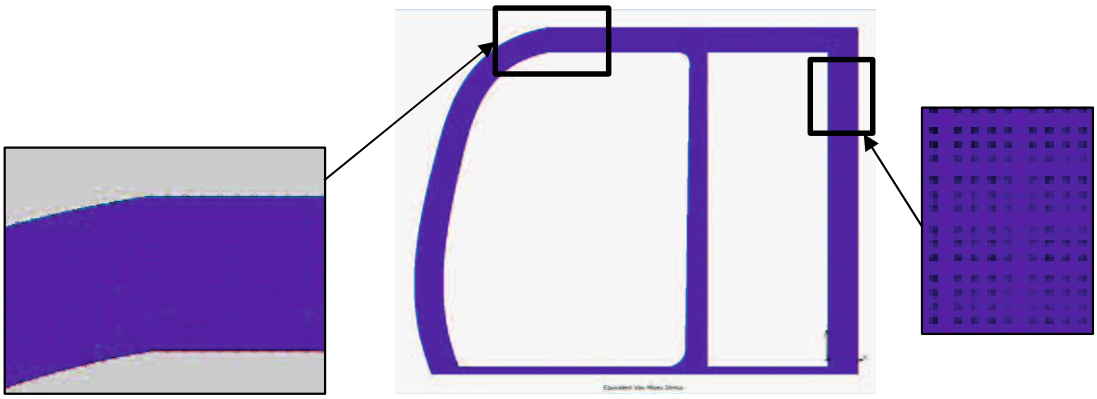

Figure 3.5. Finite element of cab frame model.

3.4.2 Boundary Condition and Material Properties of Cab Frame

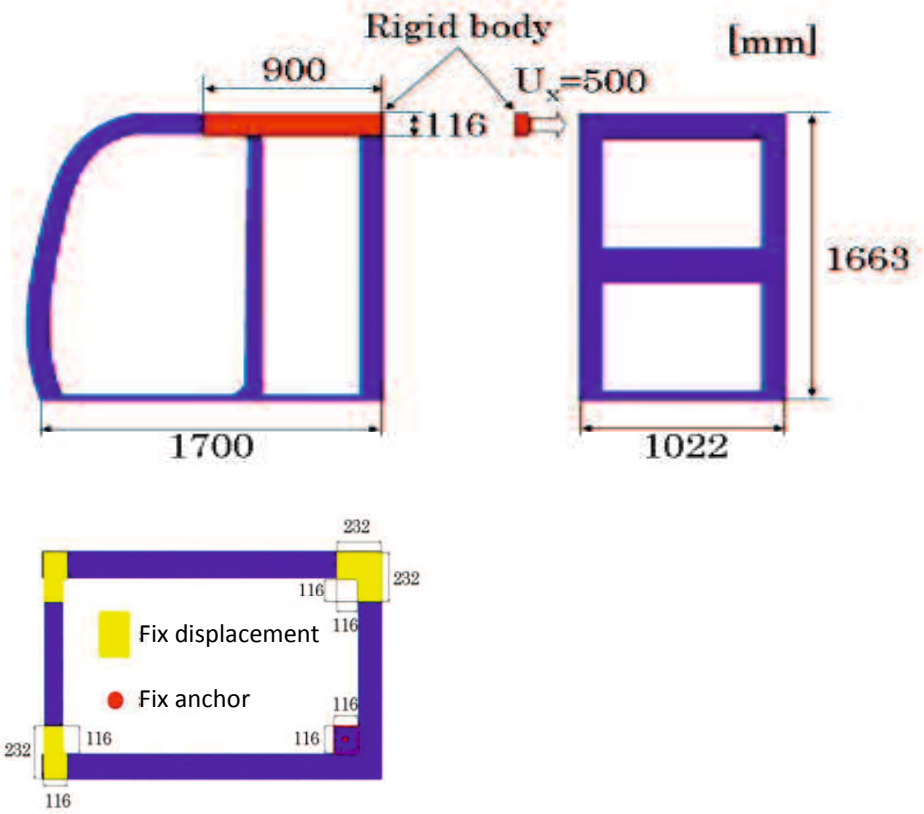

(a). Boundary condition of cab frame.

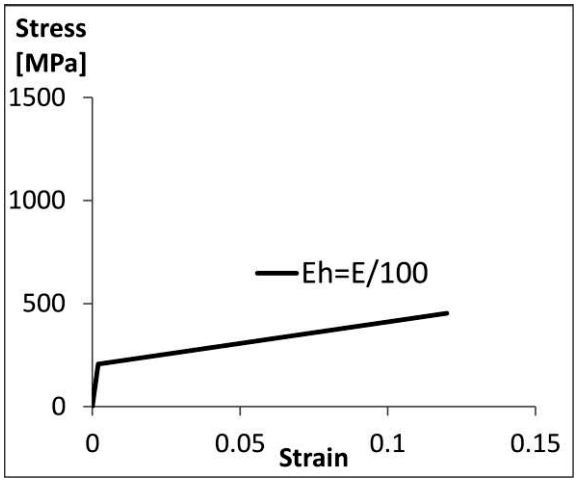

(b). Material condition of cab frame (bilinear).

Figure 3.6. Boundary condition and material condition of cab frame.

3.4.3 Finite Element Simulation Process of Cab Frame

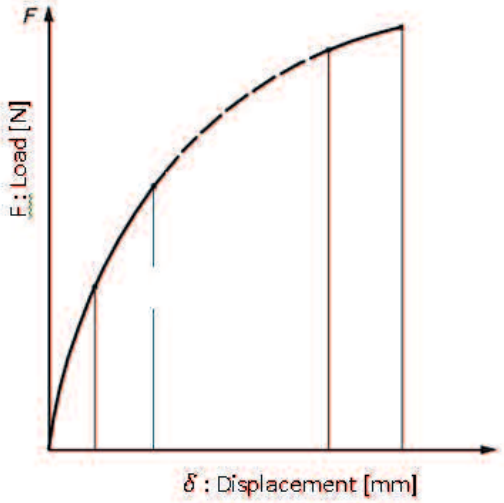

(a). Load-Displacement curve of cab frame on roll over.

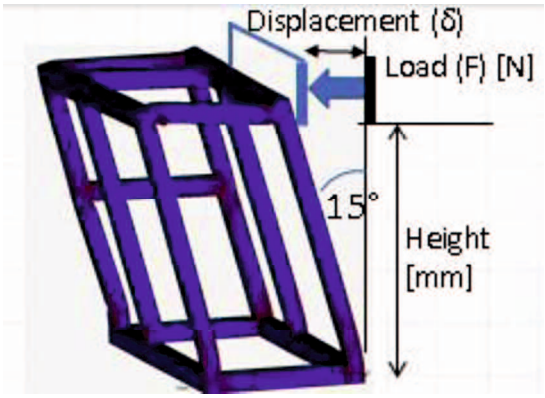

(b). Deformation step of cab frame on roll over.

Figure 3.7. Load-Displacement curve and deformation step of cab frame.

Table 3.4. Material properties of cab frame.

	Properties
Elastic	E = 205.9 [GPa] σ_y = E/1000 [MPa] Ɛ = 0.002 v = 0.3
Plastic	Eh= E/100 [GPa]

Simulation process considered as static condition, simulation control is displacement and starts from point of rigid body in Ux direction. Total Ux displacement is 500[mm], and incremental step is 2[mm]. Rigid body acts as a ground pressure to cab frame in rollover condition. Simulation will stop when 1 cycle time is complete in 500[mm] within 250 steps. Outputs of simulation are rigid body load in [kN] and displacement in [mm].

3.4.4 Finite Element Model of Square Tube

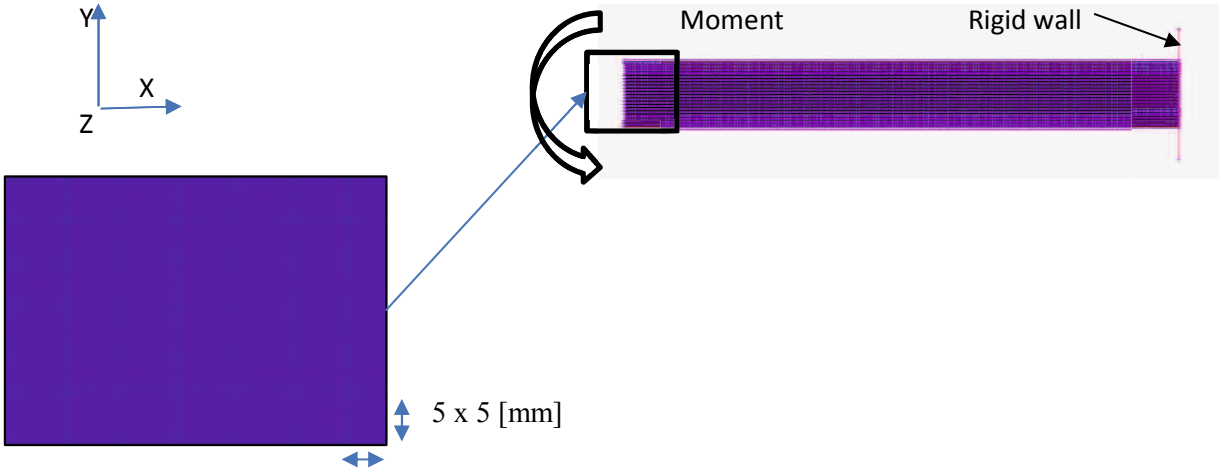

Figure 3.8. Finite element model of square tube.

Table 3.5 Finite element properties of square tube

Meshing size	5 x 5 [mm]
Meshing type	3D Shell, Quadrilateral, Isotropic
Simulation type	Static

3.4.5 Boundary Condition and Material Properties of Square Tube

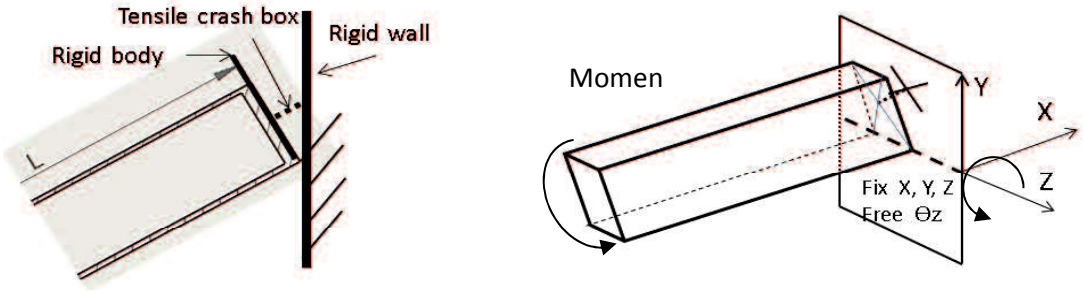

(a). Square tube using tensile crash box.

(b). Boundary condition of square tube with tensile crash box.

Figure 3.9. Square tube with tensile crash box model.

Square tube body was attached by moment of rotation at front end. Direction of rotation is Z axis and the center of rotation is at end side of tube with rigid body. Rigid body acts as rigid wall where the square tube connected by tensile crash box as energy absorber. Material properties of square tube similar with cab frame condition in Figure 3.8 (b) and Table 3.2. One increment rotation is 0.3 [degree], total 200 rotations. Total increment is 60 [degree]. Load [N] was result on rigid body during rotation from MSC Marc software, while stress [MPa] result from nodes on whole square tube body, spring work [N.mm] result from contact between tensile crash box and square tube rigid body.

3.4.6 Material Condition of Finite Element Simulation

Material condition in Finite Element Simulation is considered as isotropic as follows: The linear elastic model is the most commonly used to represent engineering materials. This model is represented by Hooke's Law. It shows that stress is proportional to strain in a uniaxial tension test.

$$\sigma = E \times \varepsilon \qquad \left[\varepsilon < \frac{\sigma_y}{E.\varepsilon}\right] \qquad (3.1)$$

$$\sigma = \sigma_y + E_h\left(\varepsilon - \frac{\sigma_y}{E}\right) \qquad \left[\varepsilon > \frac{\sigma_y}{E.\varepsilon}\right] \qquad (3.2)$$

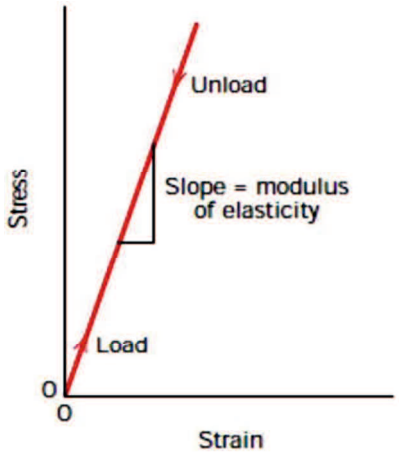

Young modulus (E) for metals:
(Magnesium – Tungsten) → 45 [GPa] – 407 [GPa]
FE simulation using (E) = 205,6 [GPa]
Poisson ratio (υ) for metals:
(Tungsten - Magnesium) → 0,28 – 0,35
FE simulation using (υ) = 0,3

Figure 3.10. Material condition of FEM in elastic region.

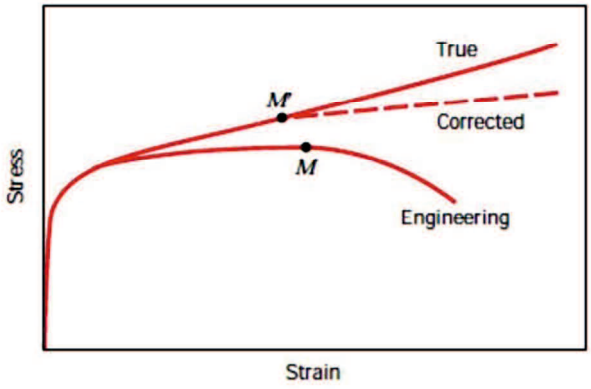

Figure 3.11. Material condition of FEM in plastic region.

This simulation using stress strain curve which follow bilinear hardening law. Because engineering curve not exhibit real condition of material under high deformation condition, this type only proper for small deformation material. While true stress-strain curve will only reflects single material properties which is not suitable for develop dimensionless parameter of simulation.

CHAPTER IV

STUDY ON ENERGY ABSORPTION CHARACTERISTIC OF CAB FRAME WITH FEM

4.1 Introduction

Recently, construction machines have been commonly provided with a cab structure that is configured to protect an operator when the machines fall down. Hydraulic excavator scaffolds may use in unstable land or slopes, with a tipped over or roll over risk. Roll-Over Protective Structure (ROPS) standards have been established and considered as an important factor to protect occupant when hydraulic excavator falls. Operator's seat must be secured to passenger space in cab frame. It is necessary to withstand impact because of fall with increasing frame strength [41]-[45].

Cab frame of hydraulic excavator which was intended to isolate the occupants from wind and rain, will crushed upon fall, and this may be dangerous to passenger. The danger comes from the impact energy that transmitted to the excavator occupant. To increase passenger safety, the impact energy transmitted should be as low as possible. To minimize the impact energy, it is necessary to dissipate the energy that comes because of tipped over or rolled over by absorbing the energy through deformation of excavator structure.

To increase cab frame strength, the structural change by adding the thickness and material change has been done. Nevertheless, then, the production cost of cab frame will increase. The necessity to perform analysis during development to reduce development period and cost are discussed [46]. In this study, we use a model of cab frame with varying thickness and we performed elastoplastic numerical analysis with FEM. While generating local wrinkle, a thin cylindrical tube that is mainly used as automotive body structure, can absorb energy [47]. Residual stresses are the stresses that remained in a solid material after the original cause of the stresses has been removed. Residual stresses can occur through a variety of mechanisms such as bending, welding etc. Residual stresses due to bending process is discussed and analyzed [48], [49]. In this study, local buckling occurrence effect to energy absorption in deformation mode on each part is investigated. Effect of energy absorption characteristics by residual stress that generated upon bending process is discussed.

4.2 Research Purpose

Many type of cab frame in the market around the world has typical characteristic and advantage. Cab frame for heavy machines has many types, such as 2 posts, and multi posts (vertical pillar). Mostly excavator using at least 4 posts to secure the operator inside, due to operating weight of excavator was tent to high mass. Developing cab frame was difficult because it has to follow the safety standard of ROPS. This research develop cab frame model according to ROPS standard, and investigate characteristic deformation of cab frame. There are 3 type deformation of cab frame, see figure 4.1

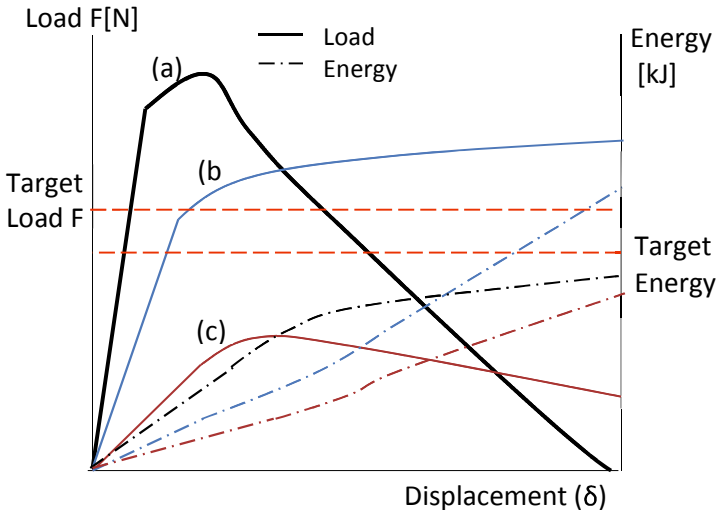

Figure 4.1. Load-Displacement curve of deformation type on cab frame

Deformation type of cab frame:

(a) Over stiff or too strength cab structure. This cab frame has high stiffness of structure with low displacement. Target load is achieved but target energy is not satisfied the ROPS standard. Example model was collect from cab of JCB Sweden, see figure 4.2.

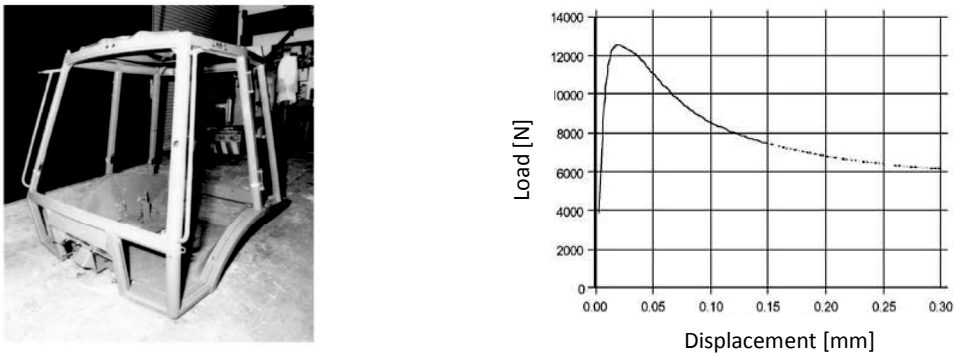

(a). Cab frame of JCB Sweden. (b). Load-Displacement curve of JCB cab.

Figure 4.2. Over stiff cab frame of JCB Sweden [15].

(b) Optimum cab structure. The cab frame has achieved both target load and energy in ROPS standard. Example model was collect from cab of Hitachi excavator, see figure 4.3.

(a). Cab frame model of Hitachi.

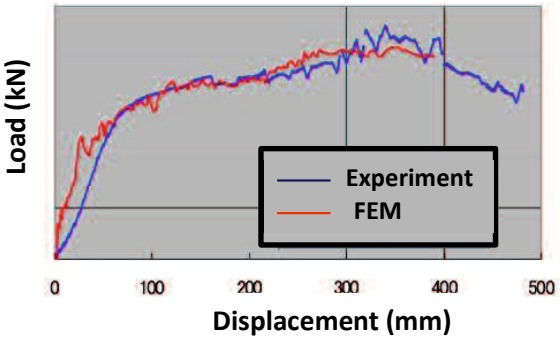

(b). Load-displacement curve of Hitachi cab.

Figure 4.3. Optimal cab frame of Hitachi [64].

Hitachi cab frame optimum condition achieved by:

- Using special design at center pillar (CRES).
- Using special part (casting part at rear horizontal pillar).
- Different machine weight required different cab's design.

(c) Too low cab structure. This cab's model not achieved both target load and energy in ROPS standard testing.

To investigate characteristic of over stiff cab frame we develop basic shape of cab using square tube with high strength in vertical pillar for finite element simulation, because there is no information about JCB cab frame for the cab size and configuration, the only information is that cab was assembly from square tube, see figure 4.4.

(a). cab frame initial condition.

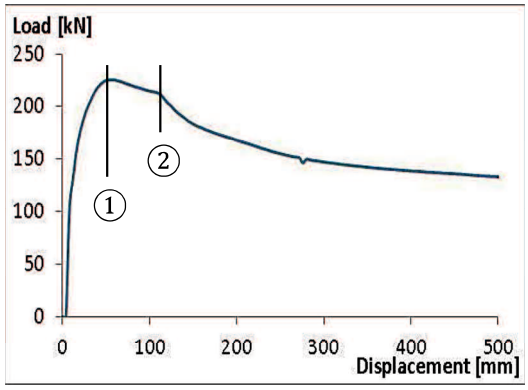

(b). Load-displacement curve of finite element simulation.

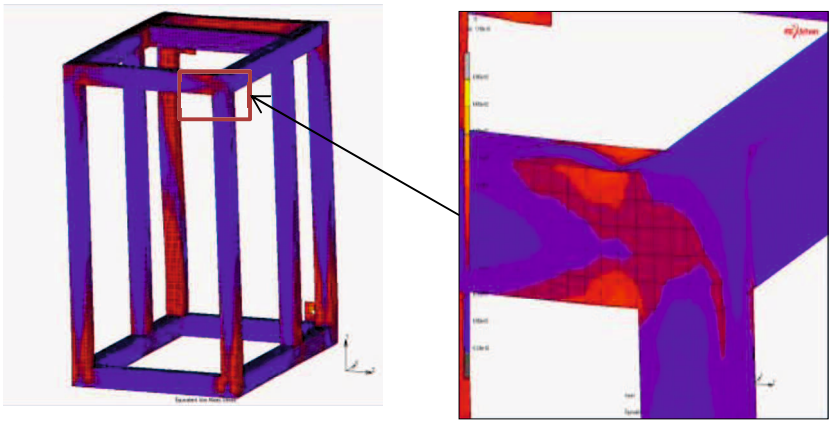

(c). local buckling at point ①

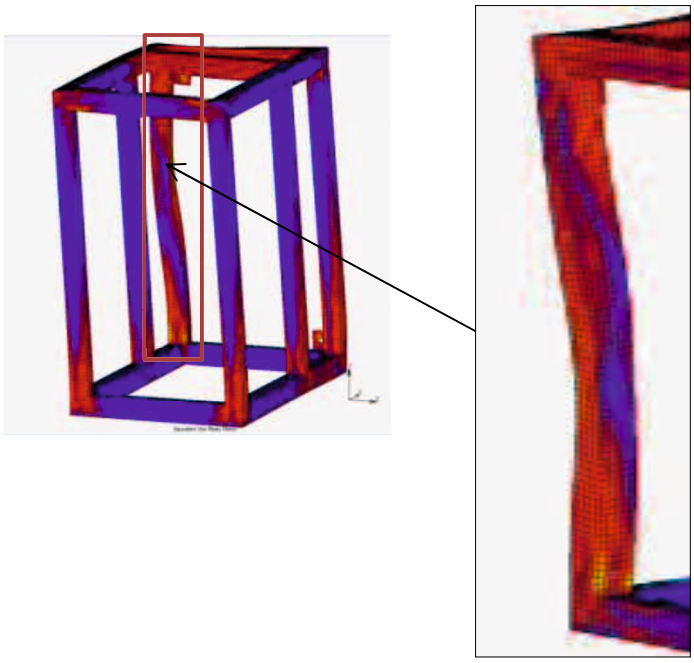

(d) global buckling at point ②

Figure 4.4. Investigate characteristic of over stiff cab frame.

From finite element simulation there are 2 importance points in such cab deformation. Cab start deformation with high slope of load and short displacement until peak condition, then start occurs local buckling at front up side cab frame (point ①). This makes load decrease slowly, until point ② occurs global buckling at back side of vertical pillar. Global buckling makes load decrease fast until deformation stop. There are important results in over stiff cab frame; local buckling and global buckling.

To investigate optimum cab frame we develop finite element simulation using Hitachi model. Size and shape of cab frame was get from Hitachi data but not all configurations were

published due to confidential information. Cab frame using square tube and the thickness condition of tube arrange using Taguchi orthogonal array, see figure 4.5.

4.3 Finite Element Analysis of Cab Frame

4.3.1 Material Properties and Boundary Condition

An elastoplastic numerical analysis of cab frame with general-purpose analysis software is performed by using MSC Marc software. The cab frame model is shown in Figure 4.5. Analysis model is created by combining a cylindrical part of quadrilateral axisymmetric shell elements. The frame is classified into 11 parts namely A ~ K. The boundary condition of frame bottom surface in 4 corners is completely restrained as shown in Figure 4.6. A rigid wall (116 × 900 [mm]) beside part D with displacement 500 [mm] is allowed to collapse the model. The material properties of cab frame are homogeneous and isotropic of elastic-plastic. Stress-strain relationship is assumed according hook's law in elastic condition, and bilinear hardening rules in plastic condition as shown in equation 4.1.

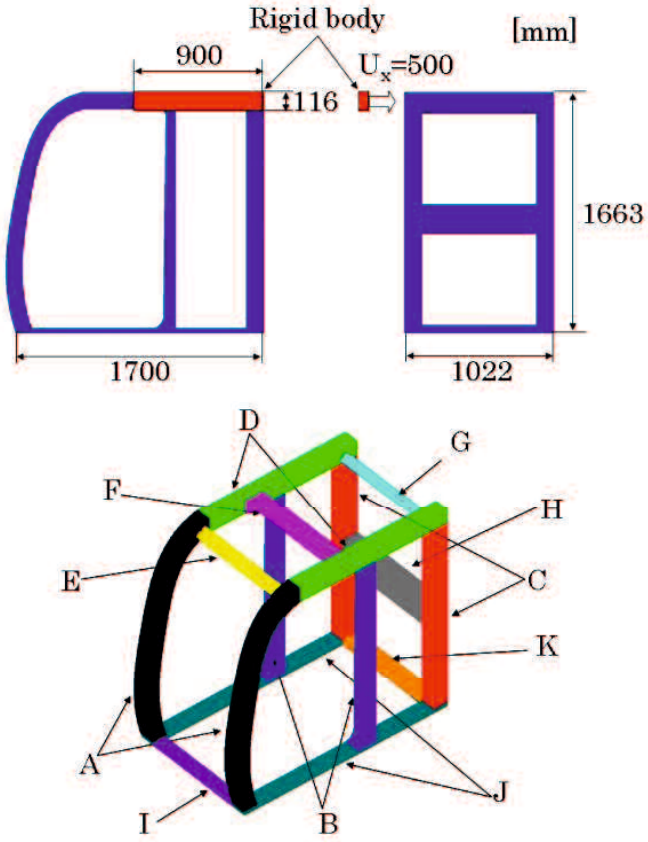

Figure 4.5. Cab frame model.

$$\sigma = E\varepsilon \qquad \left[\varepsilon < \frac{\sigma y}{E\varepsilon}\right] \qquad (3.1)$$

$$\sigma = \sigma y + Eh\left(\varepsilon - \frac{\sigma y}{E}\right) \qquad \left[\varepsilon > \frac{\sigma y}{E\varepsilon}\right] \tag{3.2}$$

Where E is Young's modulus, Eh is the work-hardening coefficient, and σ_y is the yield stress. In this study, σ_y = E /1000, E = 205.9 [GPa], and hardening ratio (E_h/E) = 1/100.

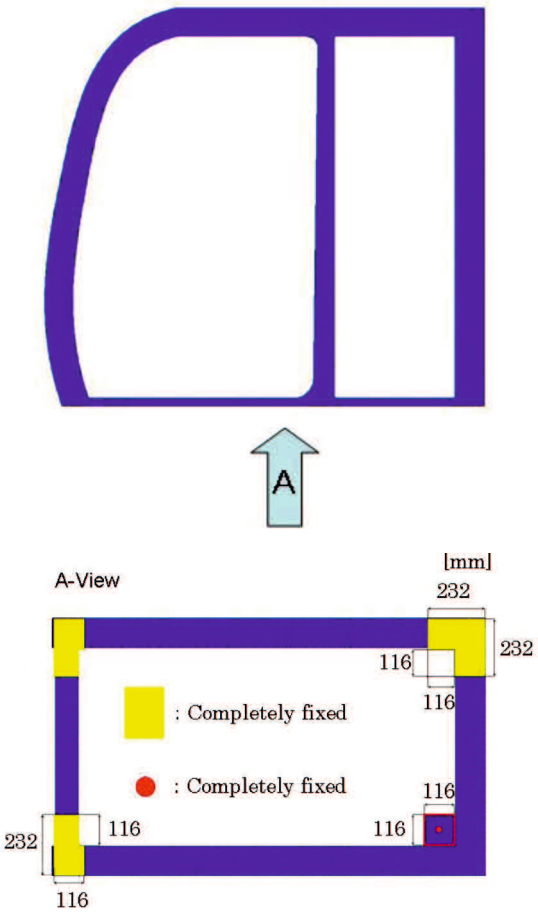

Figure 4.6. Boundary condition of cab frame

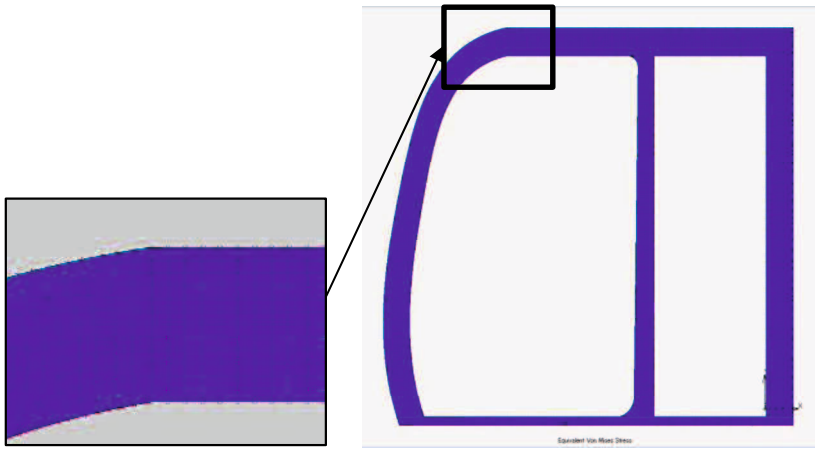

Figure 4.7. Finite element model of cab frame.

Finite element model of cab frame is quadrilateral, where 1 element consists of 4 nodes. Element type of cab frame is shell type and the thickness as the parameter. Meshing size is 10 x 10 [mm]. MSC Marc register this finite element as ID class Quad4 type 75.

Simulation process considered as static condition, simulation control is displacement and starts from point of rigid body in Ux direction. Total Ux displacement is 500 [mm], and incremental step is 2 [mm], rigid body acts as a ground pressure to cab frame in rollover condition. Simulation will stop when 1 cycle time is complete in 500 [mm] within 250 steps. Outputs of simulation are rigid body load in [kN] and displacement in [mm].

4.3.2 Simulation Result and Analysis

Evaluation method of energy absorption of cab frame is by comparing the deformation mode and load in each specimen. Parameter in this simulation is thickness of part. The thickness conditions of part are 2 [mm] and 4 [mm], with 12 variations using L12 orthogonal array of Taguchi. The combination of thickness in each specimen is shown in Table 4.1.

From FEM analysis results, the thickness conditions are evaluated which generate wrinkling of the cab frame. It is observed that there are 4 locations with wrinkle or local buckling. Figure 4.8 shows the characteristic of deformation at each area. Each deformation mode (each local buckling location) is as follows:

- Area (a): Local buckling mode at junction of part A and J.
- Area (b): Local buckling mode at junction of part D and G.
- Area (c): Local buckling mode at both ends of part H.
- Area (d): Local buckling mode at junction of part C and J.

Table 4.1. Thickness condition of parts according L12 orthogonal array.

Pillars / Specimens	A	B	C	D	E	F	G	H	I	J	K
L12-1	2	2	2	2	2	2	2	2	2	2	2
L12-2	2	2	2	2	2	4	4	4	4	4	4
L12-3	2	2	4	4	4	2	2	2	4	4	4
L12-4	2	4	2	4	4	2	4	4	2	2	4
L12-5	2	4	4	2	4	4	2	4	2	4	2
L12-6	2	4	4	4	2	4	4	2	4	2	2
L12-7	4	2	4	4	2	2	4	4	2	4	2
L12-8	4	2	4	2	4	4	4	2	2	2	4
L12-9	4	2	2	4	4	4	2	4	4	2	2
L12-10	4	4	4	2	2	2	2	4	4	2	4
L12-11	4	4	2	4	2	4	2	2	2	4	4
L12-12	4	4	2	2	4	2	4	2	4	4	2

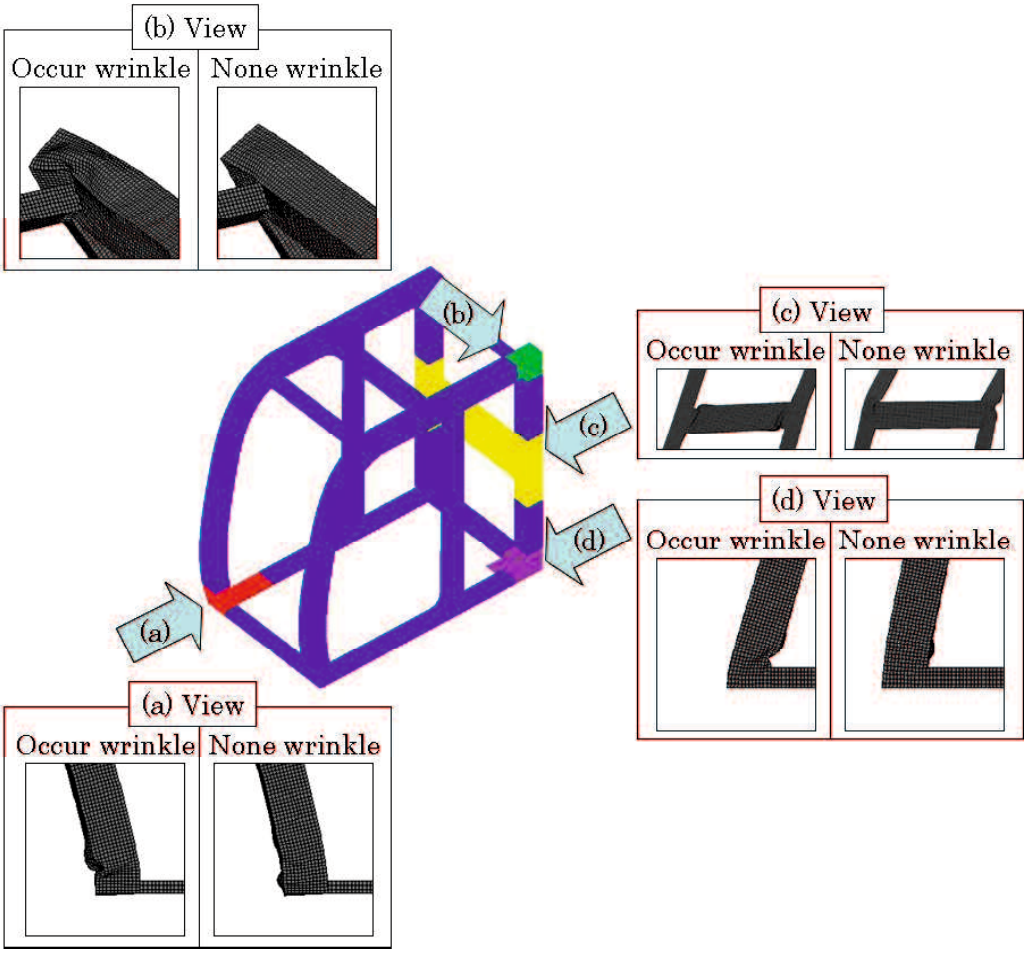

Figure 4.8. Deformation location view.

Figure 4.9 shows the comparison of deformation condition on Area (c). Load-Displacement diagram are shown in Figure 4.12. From the load-displacement curve, it can be seen that the occurrence of local buckling could reduce the energy absorption as the following condition:

- Area (a): It has a lower peak load between specimen L12-1 (local buckling) and specimen L12-7 (no local buckling). The energy absorption specimen L12-1 is 16.08 [kJ] reduced (66.65%) than specimen L12-7.
- Area (b): Specimen L12-2 obtain wrinkle and energy absorption is 17.78 [kJ] reduced (63.11%) than specimen L12-7.
- Area (c): Specimen L12-3 obtain wrinkle at area (c) and energy absorption is 33.80 [kJ]. The energy absorption reduced (29.88%) than specimen L12-7.
- Area (d): Specimen L12-11 obtain wrinkle at area (d) and energy absorption is 30.93 [kJ]. Energy absorption reduced (35.83%) than specimen L12-7.

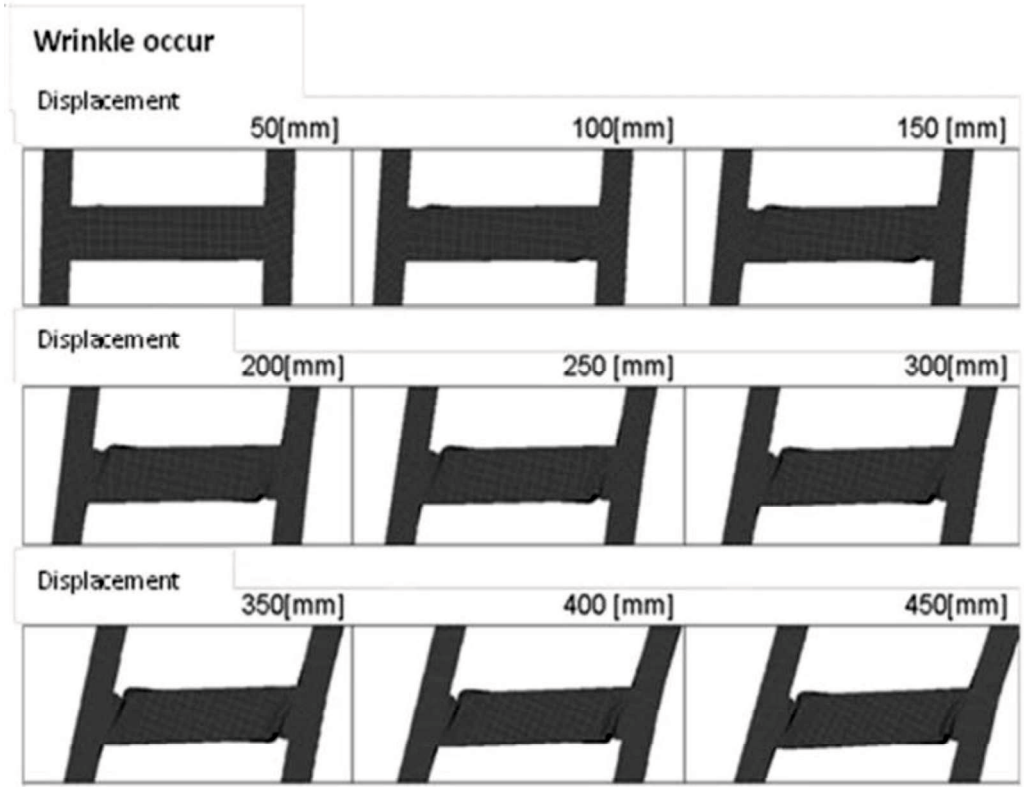

(a). wrinkle at area (c).

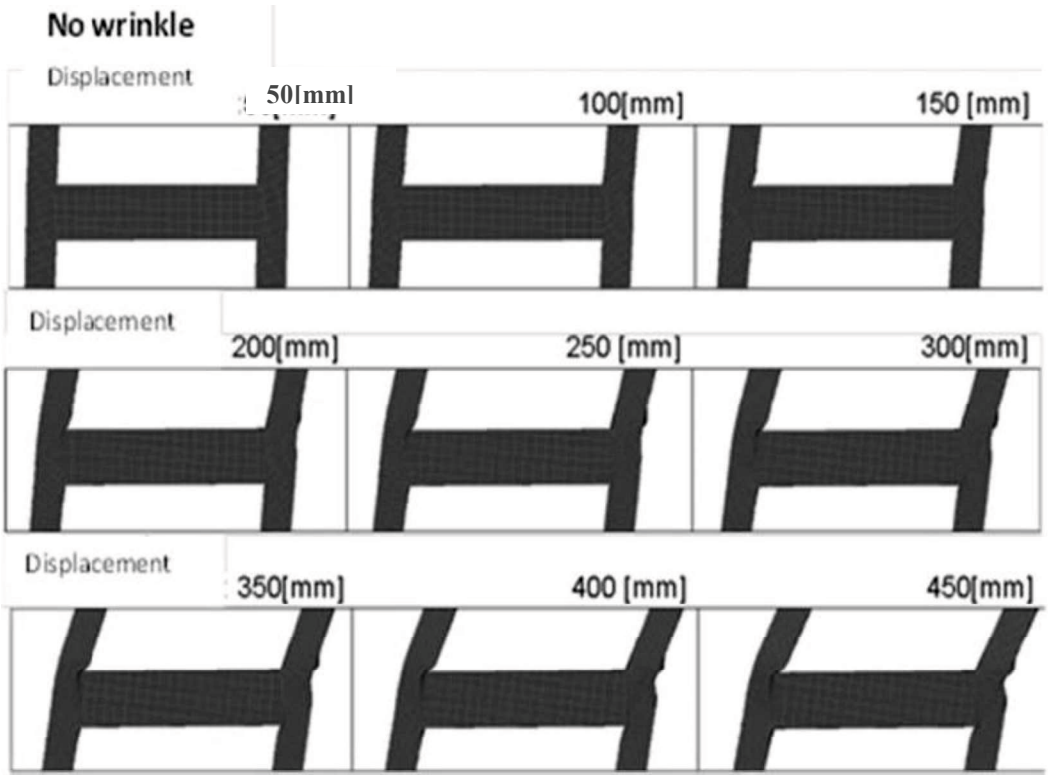

(b). No wrinkle at area (c).

Figure 4.9 Comparison deformation cab frame on area (c).

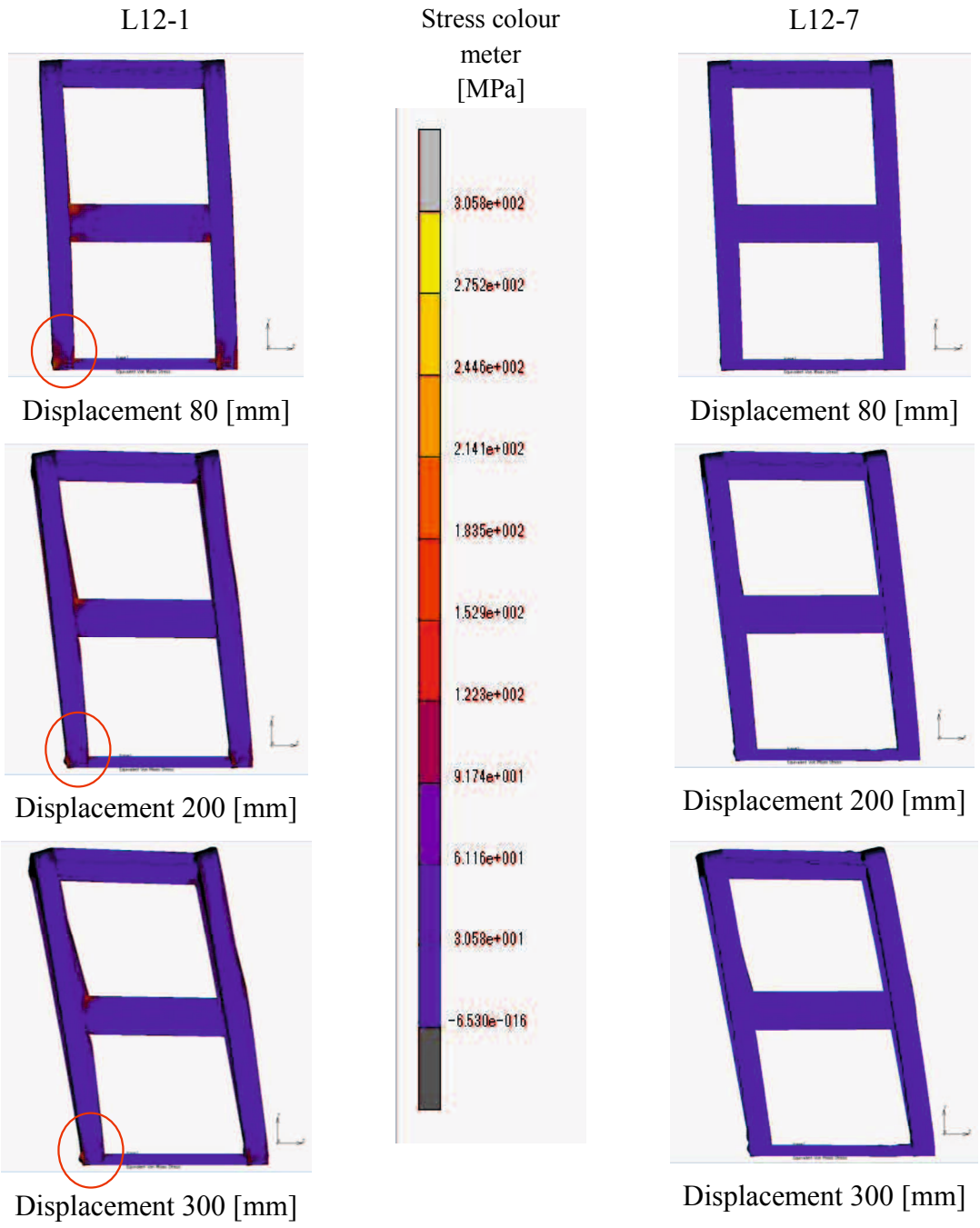

Figure 4.10. Deformation condition of specimen L12-1 and L12-7 at area (a).

Figure 4.10 show different deformation condition between specimen L12-1 and L12-7 at area (a). Wrinkle at L12-1 start occurs at displacement 80 [mm] and continue until deformation stop, while L12-7 not occurs wrinkle. Wrinkle condition examine by flattening ratio at equation (2.33). Square tube ($C_1 = C_2 = C$) will have ratio vertical shrinkage and lateral stretch 1.5. Wrinkle/ local buckling consider if the ratio less than 1.5, see table 4.4.

Table 4.2. Local buckling condition in each specimen.

	area(a)	area(b)	area(c)	area(d)	Energy [kJ]
L12-1	O	O	-	O	16.08
L12-2	O	O	-	O	17.78
L12-3	O	-	O	-	33.80
L12-4	O	-	-	O	21.80
L12-5	O	O	-	-	39.04
L12-6	O	-	O	-	30.58
L12-7	-	-	-	-	48.20
L12-8	O	O	O	-	29.32
L12-9	O	-	-	O	24.47
L12-10	O	O	-	-	37.28
L12-11	-	-	-	O	30.93
L12-12	-	O	-	O	25.07

O: local buckling

Wrinkle parameter determined from flattening condition due to bending. Flattening condition obtain from ratio between vertical shrinkage (C_{2f}) and lateral stretch (C_{1f}). See figure 4.7.

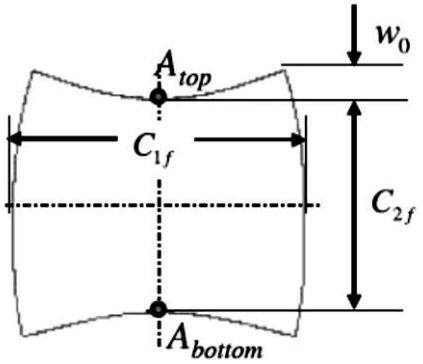

Figure 4.11. Flattening parameter [50].

Cross area flattening in bending deformation of rectangular tube can be evaluated by compared vertical shrinkage and lateral stretch using equation (2.33) and (2.34) at chapter 2. This shows that the amount of vertical shrinkage is 1.5 time the lateral stretch of square tube. Cross sections of wrinkle condition are measure from FEM simulation. Appropriate flattening ratios of each part from area (a) until (d) calculate using equation (2.33). If the flattening amount is under the ratio then consider as local buckling, otherwise more than the ratio is consider as no local buckling. Table 4.3 shows the flattening ratio of each part.

Table 4.3. Flattening ratio of area.

area	(a)		(b)		(d)	
Pillars	A		D		C	
Size (mm)	C1	C2	C1	C2	C1	C2
	117	117	117	117	117	117
Ratio	1.5		1.5		1.5	

Table 4.4. Flattening condition at area (a) at specimen L12-1 and L12-7.

Specimen	L12-1	(a)	FR
Displacement [mm]	C1f	C2f	
0	117.00	117.00	∞
50	118.28	115.35	1.29
100	119.44	112.15	1.99
150	119.02	109.25	3.84
200	115.48	106.44	-6.93
250	112.04	104.08	-2.60
300	109.68	102.16	-2.03
350	107.56	100.47	-1.75
400	105.39	98.92	-1.56
450	103.08	97.57	-1.40

Specimen	L12-7	(a)	FR
Displacement [mm]	C1f	C2f	
0	117.00	117.00	∞
50	117.13	115.59	11.16
100	117.43	113.23	8.75
150	118.04	110.88	5.89
200	119.00	108.81	4.09
250	119.86	107.08	3.46
300	120.48	105.64	3.27
350	120.54	104.48	3.54
400	119.32	103.78	5.70
450	117.20	103.46	68.50

Table 4.5. Flattening condition at area (d) at specimen L12-1 and L12-7.

Specimen	L12-1	(d)	FR
Displacement [mm]	C1f	C2f	
0	117.00	117.00	∞
50	119.43	115.98	0.42
100	128.07	114.97	0.18
150	133.94	114.34	0.16
200	137.49	114.00	0.15
250	140.30	113.78	0.14
300	142.75	113.64	0.13
350	144.92	113.58	0.12
400	146.84	113.59	0.11
450	148.52	113.68	0.11
500	150.01	113.86	0.10

Specimen	L12-7	(d)	FR
Displacement [mm]	C1f	C2f	
0	117.00	117.00	∞
50	117.25	115.32	6.80
100	117.47	113.70	7.01
150	117.61	112.59	7.22
200	117.57	111.73	9.29
250	117.42	110.89	14.58
300	117.23	109.99	30.71
350	117.05	109.08	175.58
400	117.69	108.17	12.84
450	117.33	107.24	29.54
500	115.88	106.31	-9.54

From table 4.5 shows that flattening ratio specimen L12-1 from displacement 50mm until 500 [mm] in ratio lower than 1.5. During that range area (d) at specimen L12-1 obtain local buckling with flattening ratio less than appropriate. The contrast result shows by specimen L12-7 at area (d), flattening ratio of L12-7 more than 1.5. It shows that specimen L12-7 not obtains local buckling at area (d).

Wrinkle occurrence of each condition is shown in Table 4.2. The condition with wrinkle occurrence is indicated by **(O)**. Wrinkle conditions are as follows:

- Area (a): specimen L12-1 part A and part J is 2 mm,

- Area (b): specimen L12-2 part D is 2 mm,
- Area (c): specimen L12-3 part C is 4 mm and part H is 2 mm,
- Area (d): specimen L12-11 part C is 2mm.

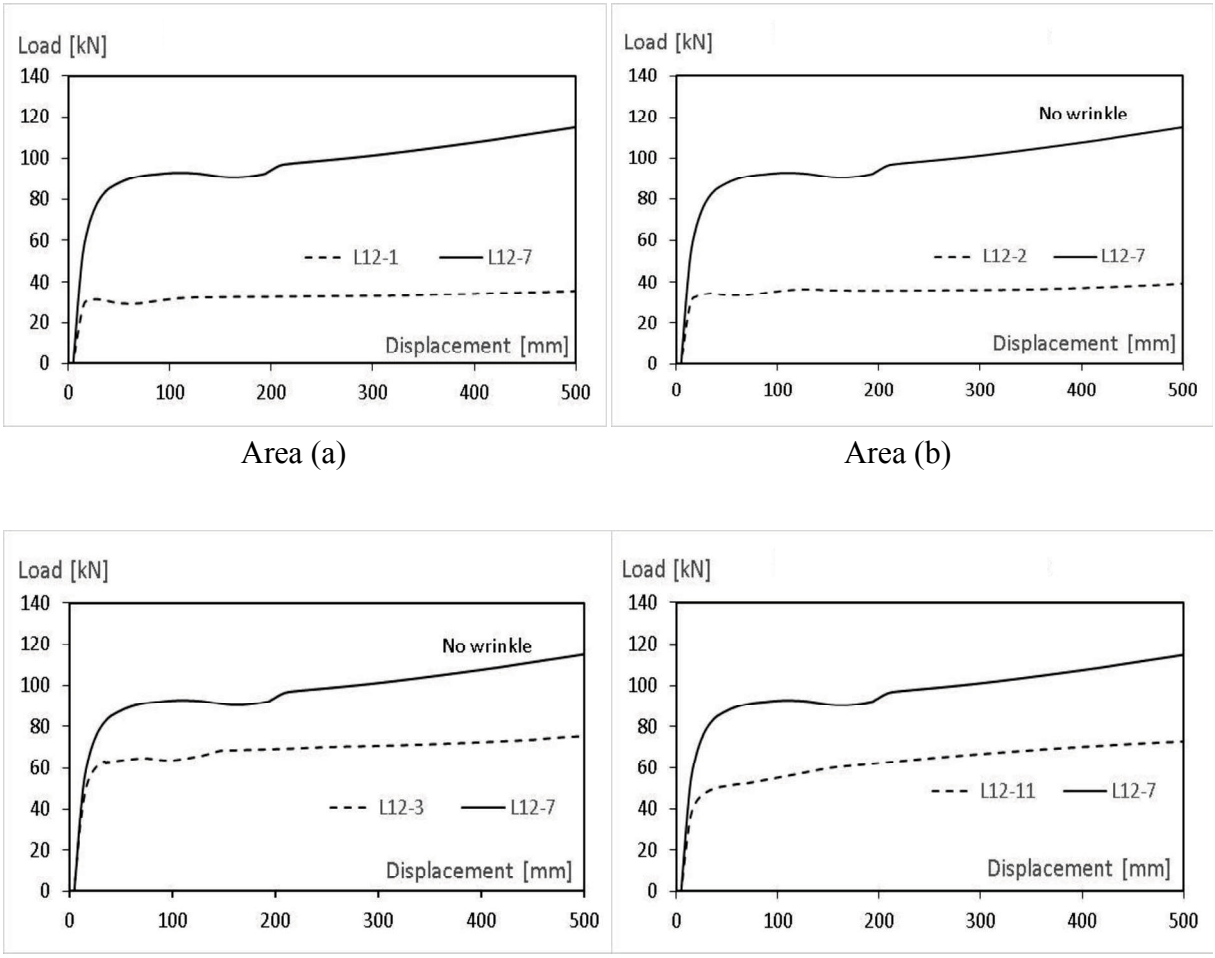

Area (a) Area (b)

Area (c) Area (d)

Figure 4.12 Comparison load-displacement curve for area (a), (b), (c), and (d).

Figures 4.13 – 4.16 show the comparison of energy absorption due to difference of deformation mode for areas (a), (b), (c), and (d). All specimens compare with L12-7, because this specimen has no wrinkle at those positions.

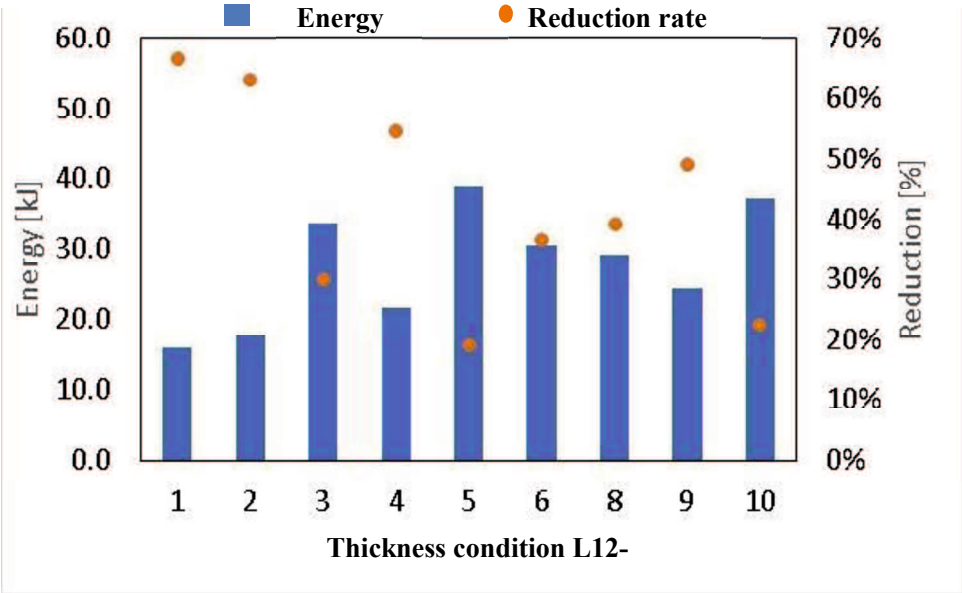

Figure 4.13 Comparison energy absorption due to different deformation mode – area (a).

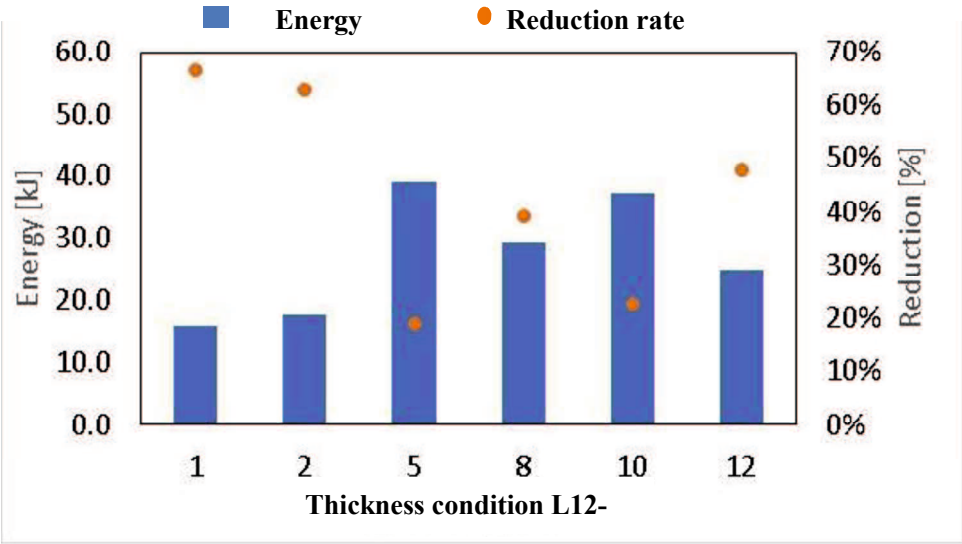

Figure 4.14 Comparison energy absorption due to different deformation mode – area (b).

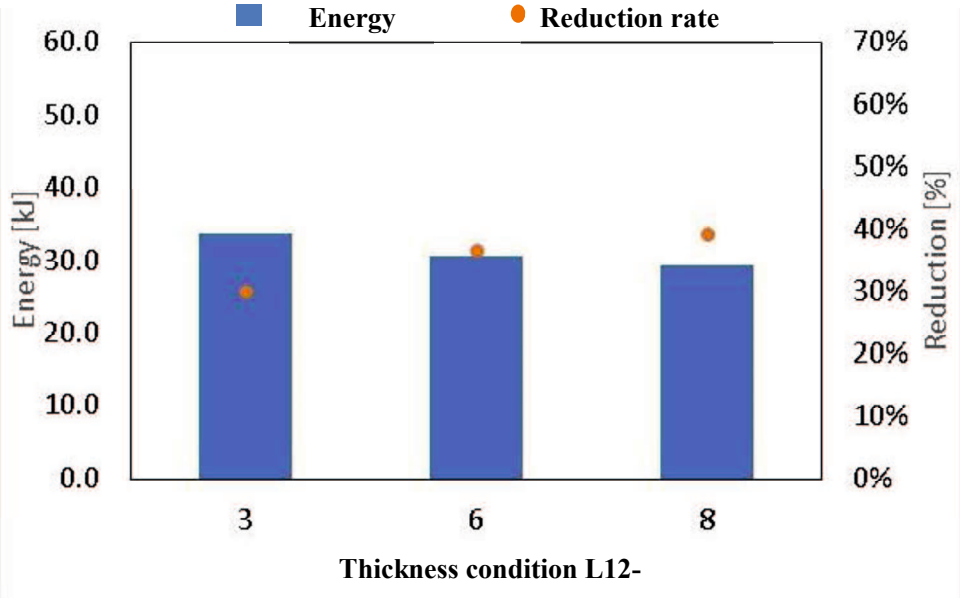

Figure 4.15 Comparison energy absorption due to different deformation mode – area (c).

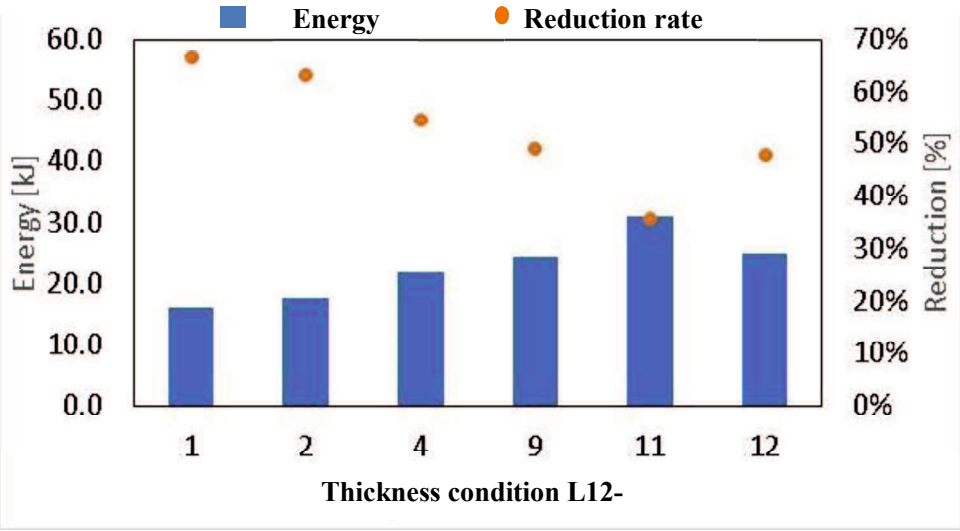

Figure 4.16 Comparison energy absorption due to different deformation mode – area (d).

4.4 Modification on Part C

4.4.1 Condition Analysis of Modification

From analysis results, it is obtained that part C has many point interfere with wrinkle area (b), (c), and (d). The modification shape in part C is analyzed. With this modification, new shape can shorten overall length of hydraulic excavator, and it will be easier to pivot in a narrow space. This part is created by bending a straight part (part C), as shown on Figure 4.17.

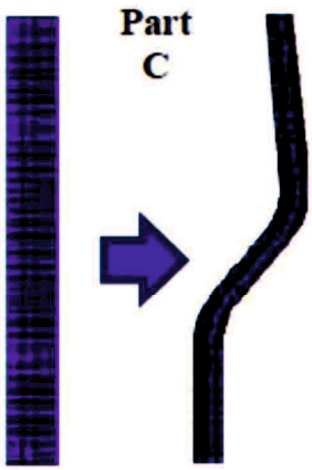

Figure 4.17. New improvements on part C.

Boundary conditions and material properties are equal with previous analysis (for straight shape of part C). Using L12 orthogonal array, condition of each part with different thickness is analyzed and the condition with highest energy absorption is used for subsequent analysis. The thickness of part C for all conditions is 6 mm, and the other parts are variations of 2 mm and 4 mm. From FEM analysis results, thickness and wrinkling occurrence of cab frame is evaluated. Different variant is observed at three positions as shown on Figure 4.18. Each of the deformation modes (each wrinkle occurrence location) are as follows.

- Area (a): Part A, wrinkles at junction of J or I.
- Area (b): Part B, wrinkles at junction of D.
- Area (c): Part H, wrinkles at both ends of part H.

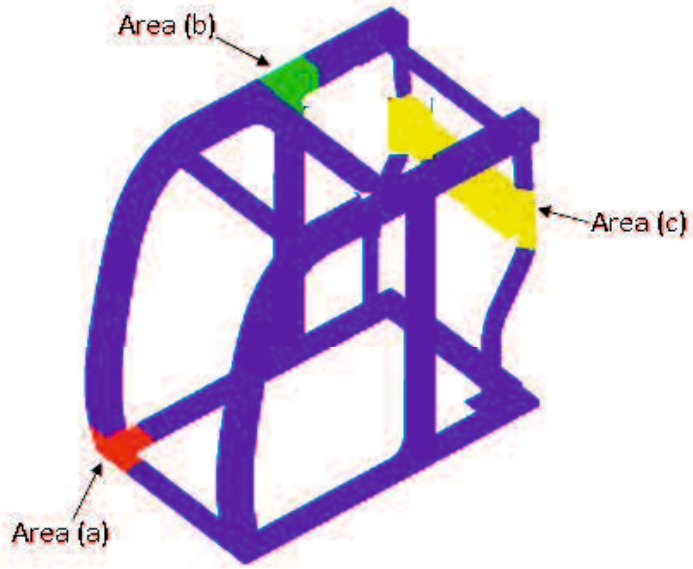

Figure 4.18. Modification cab frame on part C.

Table 4.6. Deformation mode after modification.

Specimens	Area (a)	Area (b)	Area (c)
L12-1	○	○	○
L12-2	○	○	-
L12-3	○	-	○
L12-4	○	-	-
L12-5	○	○	-
L12-6	○	-	○
L12-7	-	-	-
L12-8	○	○	○
L12-9	○	-	-
L12-10	○	○	-
L12-11	-	-	○
L12-12	-	○	○

○: Local buckling

4.4.2 Evaluation of Energy Absorption

Part thickness which wrinkles occurred for each area is area (a): part A or J is 2 mm, Area (b): part D is 2 mm, Area (c): part H is 2 mm. The characteristic of displacement and load due to wrinkling location is shown in Figures 4.19 - 4.20. Regardless of occurrence point, load was decreased by occurrence of wrinkles. On areas (a) and (b), we can see similar trend on load. The increment of a load for no wrinkle occurrence at displacement more than 200 mm is slightly different.

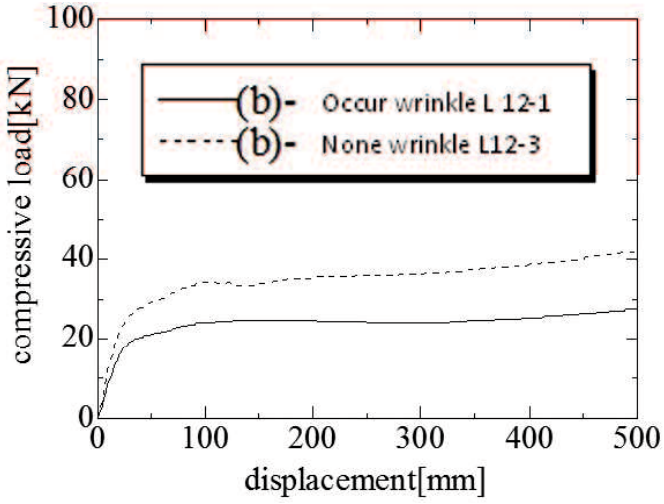

Figure 4.19. Effect of wrinkle on area (b) on modification.

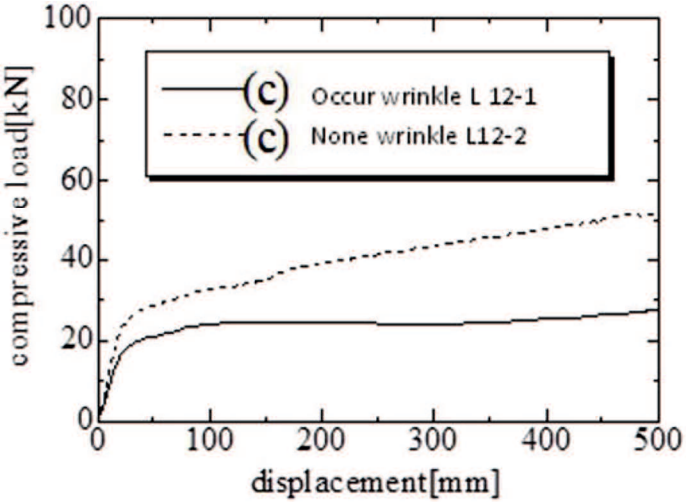

Figure 4.20. Effect of wrinkle on area (c) on modification.

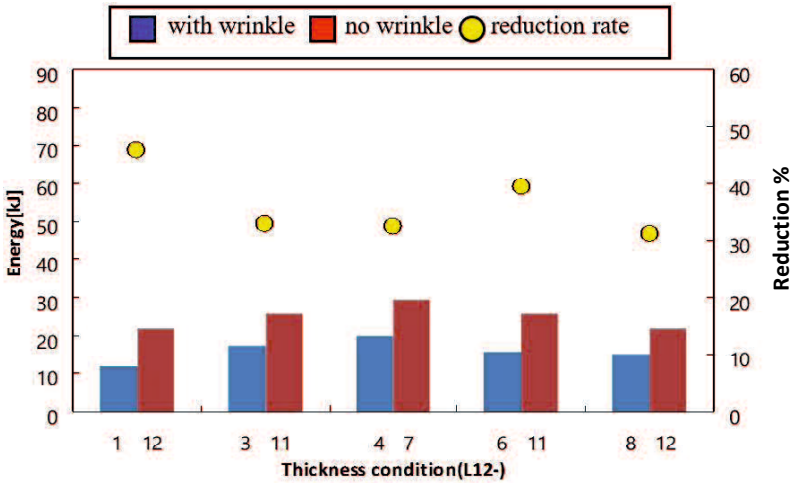

Figure 4.21. Comparison energy absorption after modification at area (a).

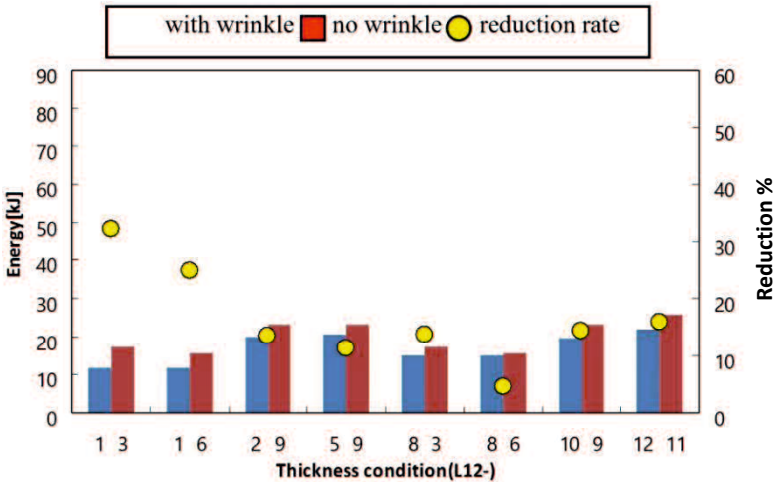

Figure 4.22 Comparison energy absorption after modification at area (b).

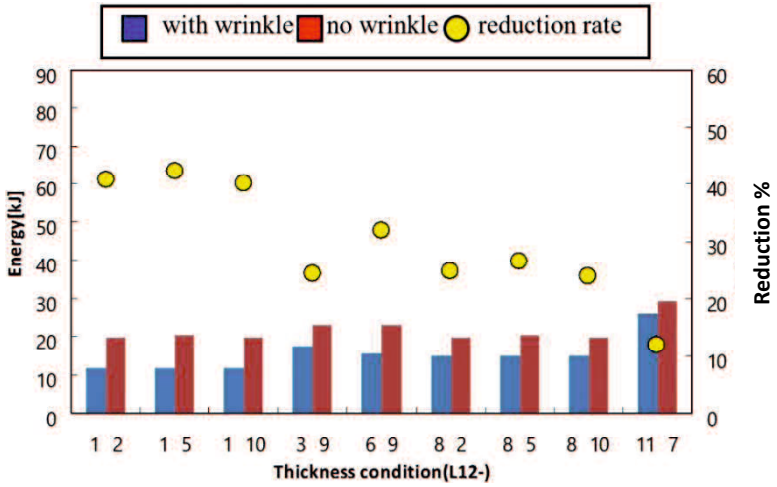

Figure 4.23 Comparison energy absorption after modification at area (c).

Figures 4.21 – 4.23 show the comparison of reduction rate and energy absorption amount of each part respectively. If wrinkle occurs, energy absorption was reduced. In area (a), wrinkling make energy absorption amount significantly decreased (about 45%). Conversely, energy absorption decrease by wrinkling area (b) is lower. Thickness conditions that showed the highest energy absorption is L12-7 without occurrence of wrinkles in respective part. Therefore, analysis of energy absorbing characteristics due to residual stress using the wall thickness at L12-7.

4.5 Conclusion

Study on absorption characteristic of cab frame was performed in this chapter using finite element analysis. Load – displacement curve of cab frame was divided into three type; over stiff, optimum, and too low cab frame condition. This study used optimum cab model to study the characteristic in roll over condition. Parameter of thickness condition and its effect on cab frame characteristic investigated. The conclusions of energy absorption characteristic of cab frame are:

1. There are 3 main type of cab frame load-deformation characteristic, there are; over stiff, optimum, and too low cab frame condition.
2. Deformation on cab frame occur local buckling (wrinkle) in 4 area; (a), (b), (c), and (d).
3. Cab frame with no local buckling occur has high energy absorption than with local buckling.
4. Flattening ratio (FR) is importance parameter to identify local buckling at cab frame
5. It is confirmed that residual stress generated from forming part C is possible to increase the energy absorption.

CHAPTER V

STUDY OF BENDING CHARACTERISTICS ON ENERGY ABSORPTION PART BY USING SQUARE TUBE

5.1 Introduction

A system with supported by reinforcing structures was widely used everywhere. Many construction buildings, machinery, and engineering system deploy structures support as the structure. Structure has many shapes; square, tubular, polygonal, and others. Engineers have to increase the ability of structure over the strength through its mechanical properties. Experiments were conducted many ways to produce high strength material as supported structure. The solid material has most strength compare with hollow, however, high density of solid consume more material and lead to high initial cost [29]-[31]. High strength with low weight was a superior combination as various structures. Tube shape was preferred to reduce weight and pretends as solid strength [32].

Square tubes behavior has many studies as theoretically and experimentally. Kecman studied about bending collapse behavior subjected to bending load of square tubes [33]. A theoretical analysis was compared with experimental result and found that plastic deformation was obtained between two stable segments. Johnson showed a mathematical solution of the bending and torsion of an anisotropic elastic beam [23]. It is shown that the bending stiffness is greater when twisting is banned. Kim et al. also reported his studied and suggested a new approach of collapse mechanism that improved the relationship between moment-rotation. The new solution determines two unknown constants, half-length of folding wave and rolling radius by reducing a mean crumpling moment [34]. Further studied about bending was specifically observed about flattening deformation in rectangular hollow structure [35]. The relationship between flattening ratio and non-dimensional curvatures was influenced by tube thickness [36], [38]-[40].

Haruyama et al. explored modes of an axially crushed compress-expand member to investigated energy absorption using FEM and experiments [37]. Thin wall cylindrical tube crushed impact was used and modeled as absorption energy at impact test. Collapse mode can be divided into three groups, stable mode, stable with a folding mode, and unstable mode. Moreover, [22] studied about compress-expand part under axial loading using finite element analysis and plotted various modes of member's collapse according to the geometric and

material parameter. It seems that compress-expand member had most efficiency in the smaller radius.

In this chapter, the study was focused on bending behavior of square tubes using attached part to absorb bending stress at lateral side and transmit to attach part at axial side of stress. Energy absorption of attached part investigated to influence buckling point of square tube and rigidity force of absorption part.

5.2 Research Purpose

Bending on square tube caused deformation on cross section area, this deformation trigger collapse on tube. Similar condition obtain at cab frame when withstand load in rolling over accident. Vertical pillar of cab frame deformed due to lateral force and trigger local buckling which leading to decrease strength of the structure. Buckling on square tube was highly influenced by geometric parameter of thickness and width (t/C). Higher thickness on square tube will reduce buckling but more weight on the structure. The concept to delay buckling on square tube by add crash box will improve bending performance of tube because crash box absorb energy during bending in plastic deformation and provide more displacement of tube, see figure 5.1. High stress on cross section area of square tube removes to crash box part, this give square tube more deformation.

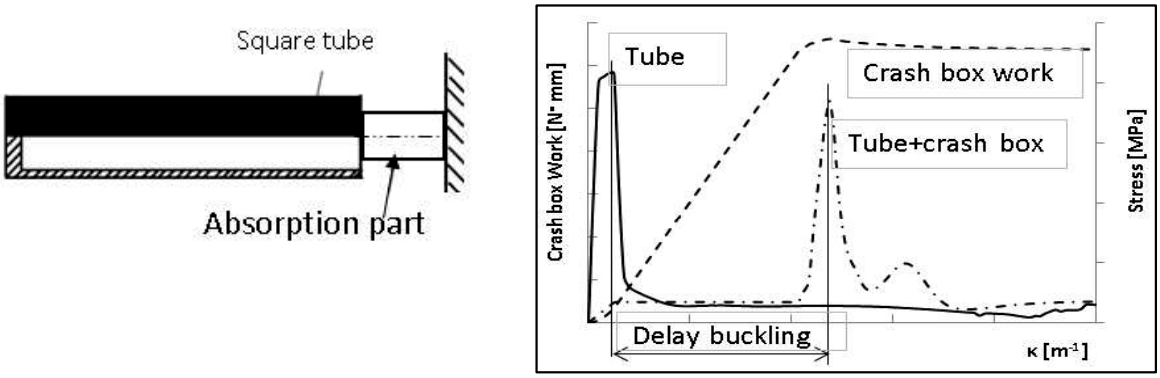

(a). Square tube using absorption part. (b). Delay buckling using absorption part.

Figure 5.1. Square tube concept using absorption part to delay buckling.

5.3 Finite Element Analysis of Square Tube

This research developed a basic model of the square tube for bending loading analysis. A compress-expand part was attached at end side of tube as absorption energy when deflection occurs during bending. Figure 5.2 shows the square tube model.

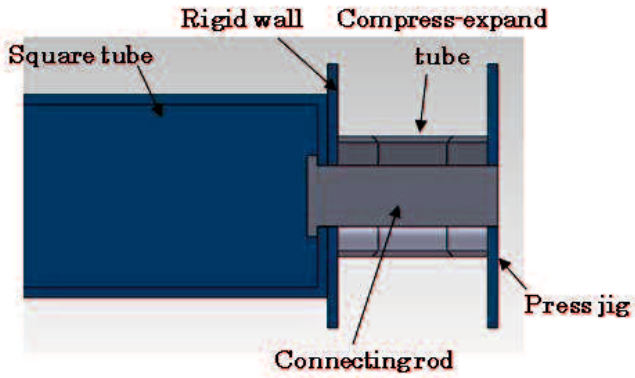

Figure 5.2. Square tube using tensile crash box (half cut model).

For analysis purposes, we develop a model of square tube with tensile crash box as absorption part which its characteristic followed compress-expand tube with three pieces section. Figure 5.3 shows model of square tube with tensile crash box.

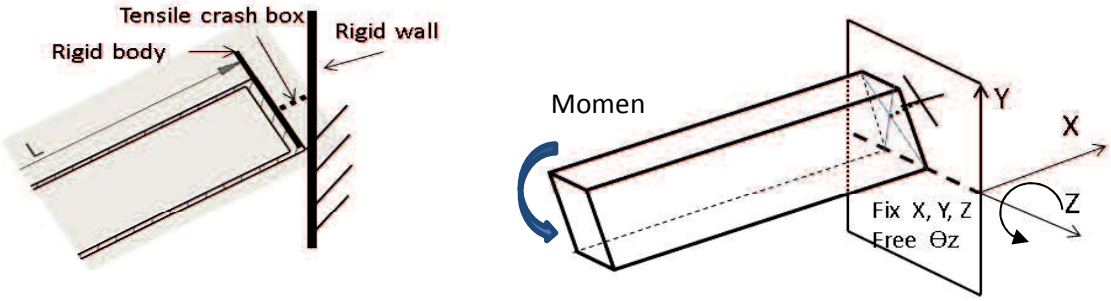

(a). Square tube with tensile crash box.

(b). Boundary condition of square tube with tensile crash box.

Figure 5.3. Square tube with tensile crash box model.

Finite element model of square tube is quadrilateral, where 1 element consists of 4 nodes. Element type is shell type and the thickness as the parameter. Rigid body is considered fixed without movement. Meshing size of square tube is 5x5 [mm], meshing type 3D shell, material condition is isotropic, and MSC Marc register this finite element as ID class Quad4 type 75.

Simulation process considered in static condition, simulation control is rotation in Z axis (counter clockwise) and attached at free end of cantilever beam. Total rotation is 200 rotation, and 1 incremental rotation is 0.3(degree). Rigid body acts as a wall which holds the cantilever body of square tube and the rigid body is fixed. Simulation will stop when 1 cycle time is complete in 200 rotations. Outputs of simulation are rigid body moment in [N.m] and time in [s].

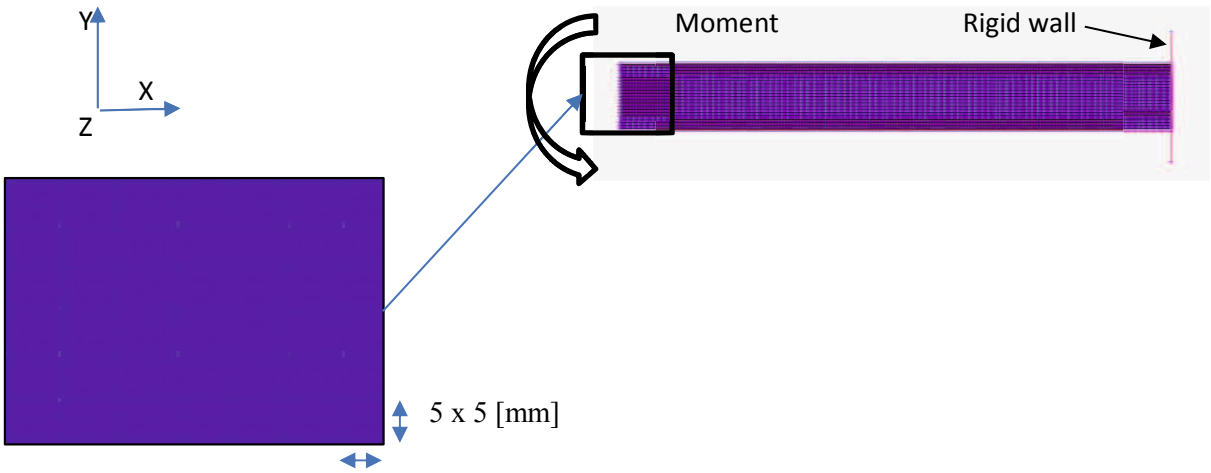

Figure 5.4. Finite element model of square tube.

Material properties of square tube considered as homogeneous and isotropic elastic-plastic, stress-strain relationship as seen at equation (5.1). Modulus of elasticity (E) is 205.9 [GPa], yield stress (σ_y) is E/1000 [MPa], strain (Ɛ) is 0.002, and Modulus hardening (E_h) is E/100 [GPa].

$$\sigma = E \times \varepsilon \qquad \left[\varepsilon < \frac{\sigma y}{E\varepsilon}\right] \qquad (5.1)$$

$$\sigma = \sigma y + Eh\left(\varepsilon - \frac{\sigma y}{E}\right) \qquad \left[\varepsilon > \frac{\sigma y}{E\varepsilon}\right] \qquad (5.2)$$

Parameters of square tube are followed table 5.1. Absorption part model are followed characteristic at figure 5.5. Absorption part was identical to crush box with three pieces (compress-expand tube). Absorption part parameters are follow table 5.2.

Table 5.1. Parameter of square tube.

Parameter	Value
Length L (mm)	1000
Width (C1= C2 = C) (mm)	100
Thickness t (mm)	1, 2, 3, 4, 5

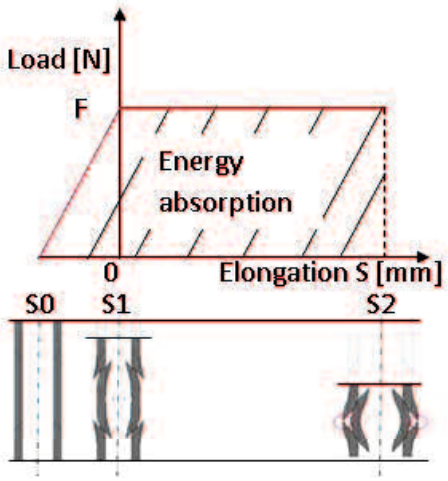

Figure 5.5. Absorption part curve characteristic.

Table 5.2. Absorption part parameters.

Parameter	Value
Constant (a)	0.2; 0.4; 0.6; 0.8
Elongation (S) [mm]	10; 20; 30
(t/C)	0.01; 0.02; 0.03; 0.04; 0.05

Absorption model was characterized as seen at equation (5.3)

$$U = F \times S \tag{5.3a}$$

$$F = a \times P_{buc} \tag{5.3b}$$

$$P_{buc} = \sigma_{buc} \times A_{sq} \tag{5.3c}$$

Where F is load of absorption part, P_{buc} is buckling load at square tube, σ_{buc} is buckling stress of square tube, and A_{sq} is the cross section area of the square tube. Parameters for absorption part are considered as table 5.2. Using MSC Marc software to perform finite element simulation, this produced importance graphic result of stress due to bending loading of square tube as seen at figure 5.7. The horizontal axis represents curvature (m^{-1}) and vertical axis shows bending moment [N.m] and secondary vertical axis is stress [MPa]. From that figure, each result was examined and compare between stress and curvature for each rigidity force. A square tube without absorption part was analysed as the basic comparison for tube equipped with absorption part.

5.4 Bending Collapse Mode

There are several buckling collapse mode of the square tube; side collapse, bottom collapse, and flat type. Each collapse figures was obtained from section A-A of square tube, see figure 5.6.

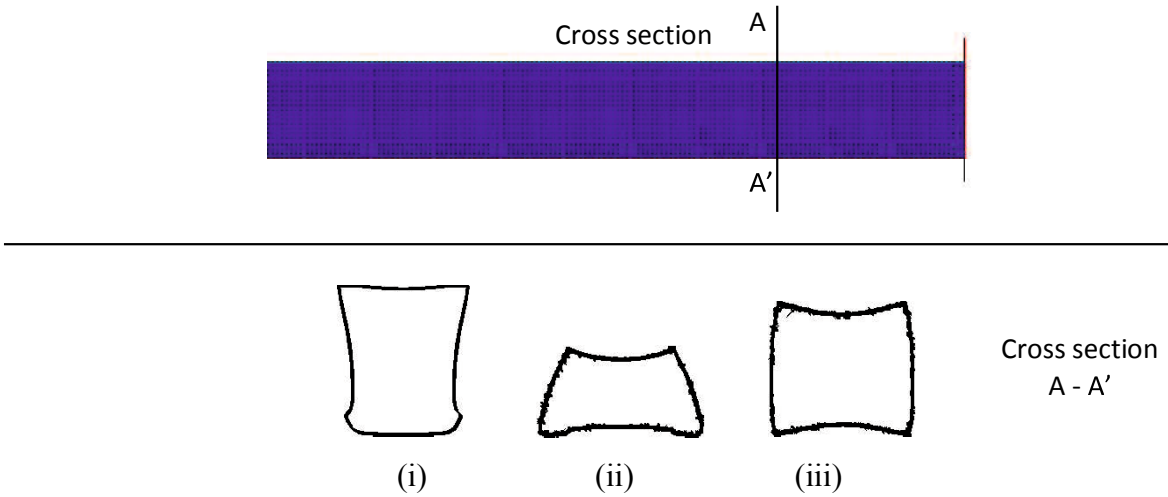

Figure 5.6. Collapse mode, (i) side collapse, (ii) bottom collapse, (iii) flat collapse mode.

Side collapse and bottom collapse produce local buckling at specific area in bending simulation, while flat collapse not occurs. Maximum bending stress obtained through table 5.3 for different rigidity force.

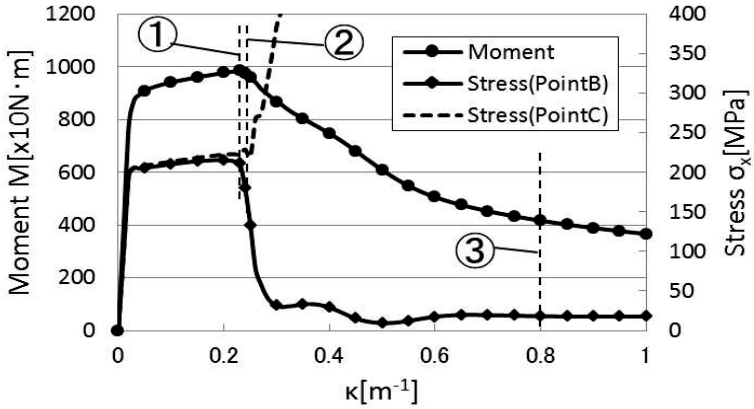

Figure 5.7. Moment-Stress comparison at local buckling collapse (E_h/E=0.01; t/C=0.03).

Figure 5.7 shows the transition of axial compressive stress between the center point (B) and corner point (C) on the compression side of the bending moment and the surface where wrinkles are generated. The bending moment and the axial stress of the point B are both highest at ①. When the bending moment starts to decrease in ②, immediately the deformation of the center section (B) progresses and the stress at the point B decreases. It is

considered that the maximum bending moment appeared mainly determined by buckling at center section (B) of the compression side surface.

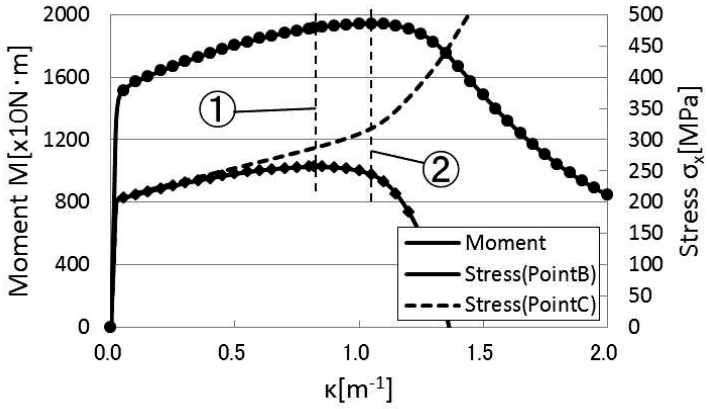

Figure 5.8. Moment-Stress comparison at flat collapse mode (E_h/E=0.01; t/C=0.05).

Figure 5.8 shows the relationship between the bending moment and the curvature and the transition of the compressive stress in the axial direction at the center point (B) and the corner point (C) on the compression side. It shows the bending moment continues to increase even when point (B) reaches the maximum stress in ①. Then, stress at the point (B) decreases, but the stress at the corner point (C) rises. From this, it is considered that the bending moment increased even after the stress at the point (B) decreased since the rate of stress rise was greater than the rate of stress reduction at the compression side.

Each absorption part with rigidity force produced different maximum bending stress compared with square tube without absorption part. Comparisons of bending stress are show at table 5.3. From table 5.3 maximum bending stress were obtained at square tube without absorption part and smallest obtained from a square tube with rigidity force $0.2P_{buc}$. The result of bending on square tube also classified base on collapse mode. Effects of the rigidity force are obtained as follows.

Table 5.3. Bending stress comparison.

Rigidity force F = a . P_{buc} [kN]	**Max Bending Stress [MPa]**	**Curvature [m^{-1}]**
Square tube only	215.5	0.19
0.2 P_{buc}	202.2	0.61
0.4 P_{buc}	207.2	0.54
0.6 P_{buc}	207.2	0.52
0.8 P_{buc}	206.5	0.14

5.4.1 Side Collapse Mechanism

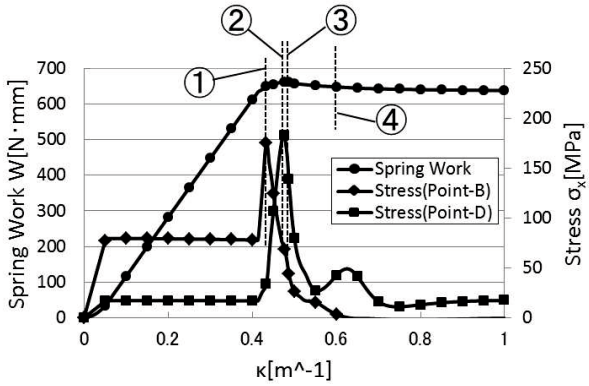

Figure 5.9. Side collapse mechanism.

Figure 5.9 shows the transition of the axial compressive stress of the spring (absorption part) work, the center point (B) and the edge point (D). Compressive stress was taken as positive. A deformed line (1-4) created to show specific deformation of square tube. The stress value at the center point (B) of the compression side reaches its maximum at ① and turns into decrease, but the spring work continues to increase. This indicates that the cause of collapse is not due to deformation of the point (B). Thereafter, when the spring work reaches the maximum in ②, the axial stress at the point (D) on the side becomes the maximum, and when the spring work turns to decrease ③ the stress at the point (D) also decreases. From this, it is considered that the spring work maximized the buckling point at the edge surface.

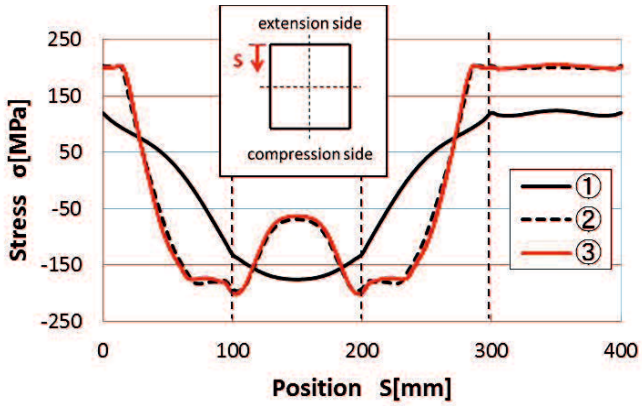

Figure 5.10. Cross-sectional stress of side collapse.

Figure 5.10 shows a cross-sectional stress diagram at ① - ③. The stress at the center side (B) decreases after reaching the maximum, but the stress on the side surface (D) rises from the corner on the compression side, so that the stress on the center side exceeds the decrease

amount and the spring work increases. It seems that the resultant force on the side surface becomes the maximum at ②, the spring work becomes the maximum.

5.4.2 Bottom Collapse Mechanism

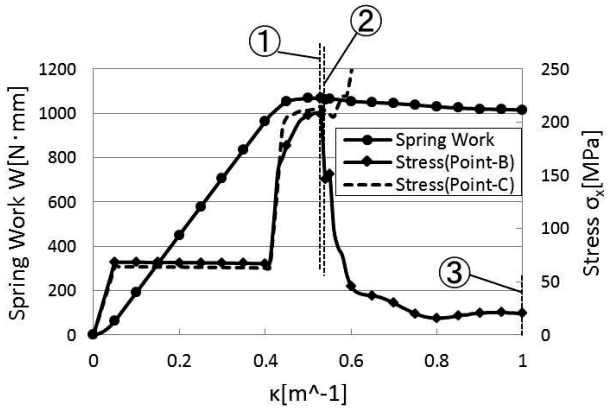

Figure 5.11. Bottom collapse mechanism.

Figure 5.11 shows the transition of axial compressive stress between the center point (B) and corner point (C) on the compression side of the surface where spring work and wrinkles are generated. The spring work and the axial stress of the point (B) are reach maximum at ①. When the spring starts to decrease at ②. Immediately the stress at the point B decreases. From this, it is considered that the spring work increased buckling point of the center side surface.

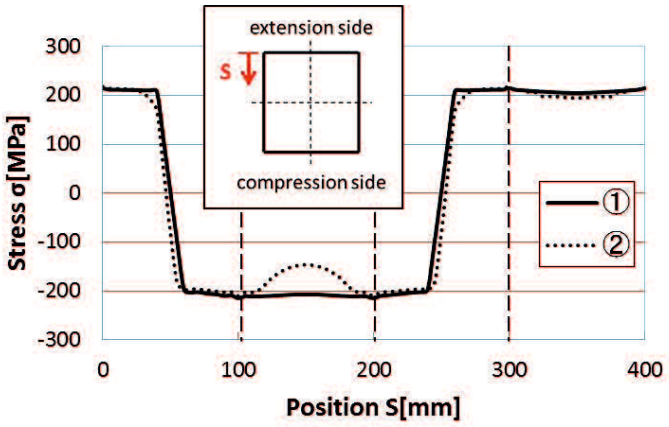

Figure 5.12. Cross-sectional stress of bottom collapse.

In order to confirm that the stress at point B decreased, figure 5.12 shows the stress distribution diagram at the buckling surface in ①, ②. It is found that the absolute values of the stresses of the extension surface and the compression surface are equal and uniformly distributed. Thereafter, in ②, the stress distribution of the extension surface hardly changes, but the absolute value of the stress of the compression surface decreases, which indicates that

buckling occurs. And as deformation progresses, wrinkles are generated as shown in the deformation chart in ③.

5.4.3 Flat Collapse Mechanism

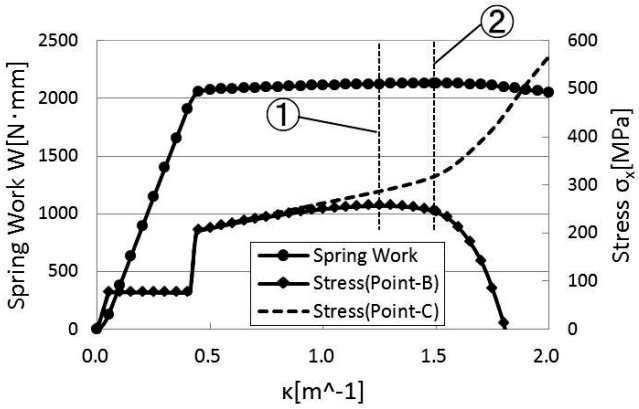

Figure 5.13. Flat collapse mechanisms.

Figure 5.13 shows the relationship between spring work and curvature and the transition of axial compressive stress. The spring work continues to increase even after point (B) has reached the maximum stress in ①. While spring work start to decrease at ②, compressive stress at point (C) continues increases.

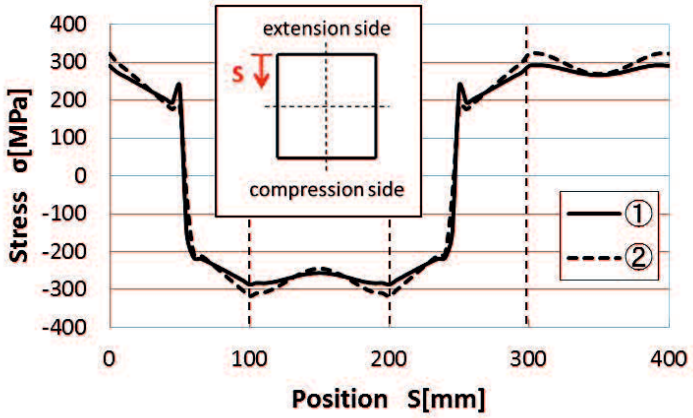

Figure 5.14. Cross-sectional of flat collapse.

As shown in figure 5.14, when ① and ② are compared, the stress at the compression side decreases but the stress at the corner point (C) rises. From this, it is considered that the spring work increased even after the stress at the point (B) decreased, since the rate of stress increase was larger than the rate of stress reduction on the compression side. Also, it can be seen that the deformation of the extension side and the compression side is the same. The

stress distributions of the extension side (S = 300 to 400 [mm]) and the compression side (S = 200 to 300 [mm]) are substantially the same. From this, it is clearly that no buckling occurs.

Since the spring element is used instead of the energy absorbing member, it is impossible to evaluate the energy after collapse where the elongation of the spring decreases. Therefore, we investigate the amount of energy absorption up to the collapse. The energy absorption E is evaluated by the sum of the strain energy (U) of the rectangular tube and the spring energy (W) performed by the absorption element. Equation of the energy absorption follows at (5.4) and (5.5). Where, V is the volume, P is the force of the spring, and δ is the elongation of the spring.

$$U = V \int \sigma_{ij} \varepsilon_{ij} \tag{5.4}$$

$$W = \int P d\delta \tag{5.5}$$

We compare the energy absorption amount of each deformation mode in the square tube where the spring element is applied. Figure 5.15 shows the relationship between the energy increment ΔE/κ and the curvature κ until each deformation mode leads to collapse.

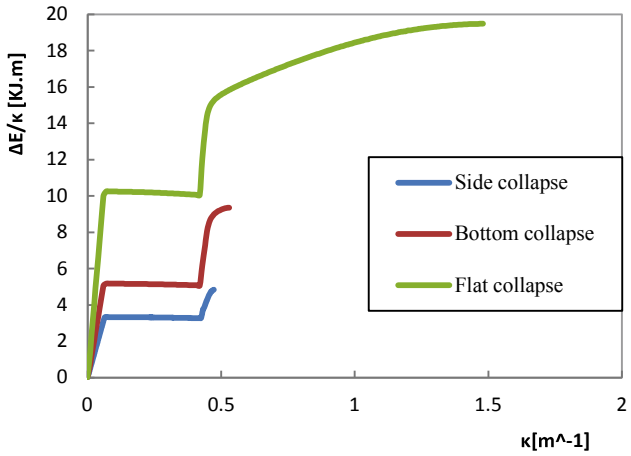

Figure 5.15. Energy base on collapse mode.

From figure 5.15, the increasing trend is the same in all deformation modes up to ②. Specifically, in ① the spring extends to h, ① ~ ② while h is increase, the spring force is constant. After that, the elongation of the spring becomes x in ② (elongation of h and x follow figure 3). After ② the deformation of the rectangular tube starts, leading to the collapse. As compared with the energy absorption amount, it is clear that the flat type has a larger amount of energy than the bottom type. Because the flat type wall thickness is thicker than the bottom type, and therefore the rigidity is high.

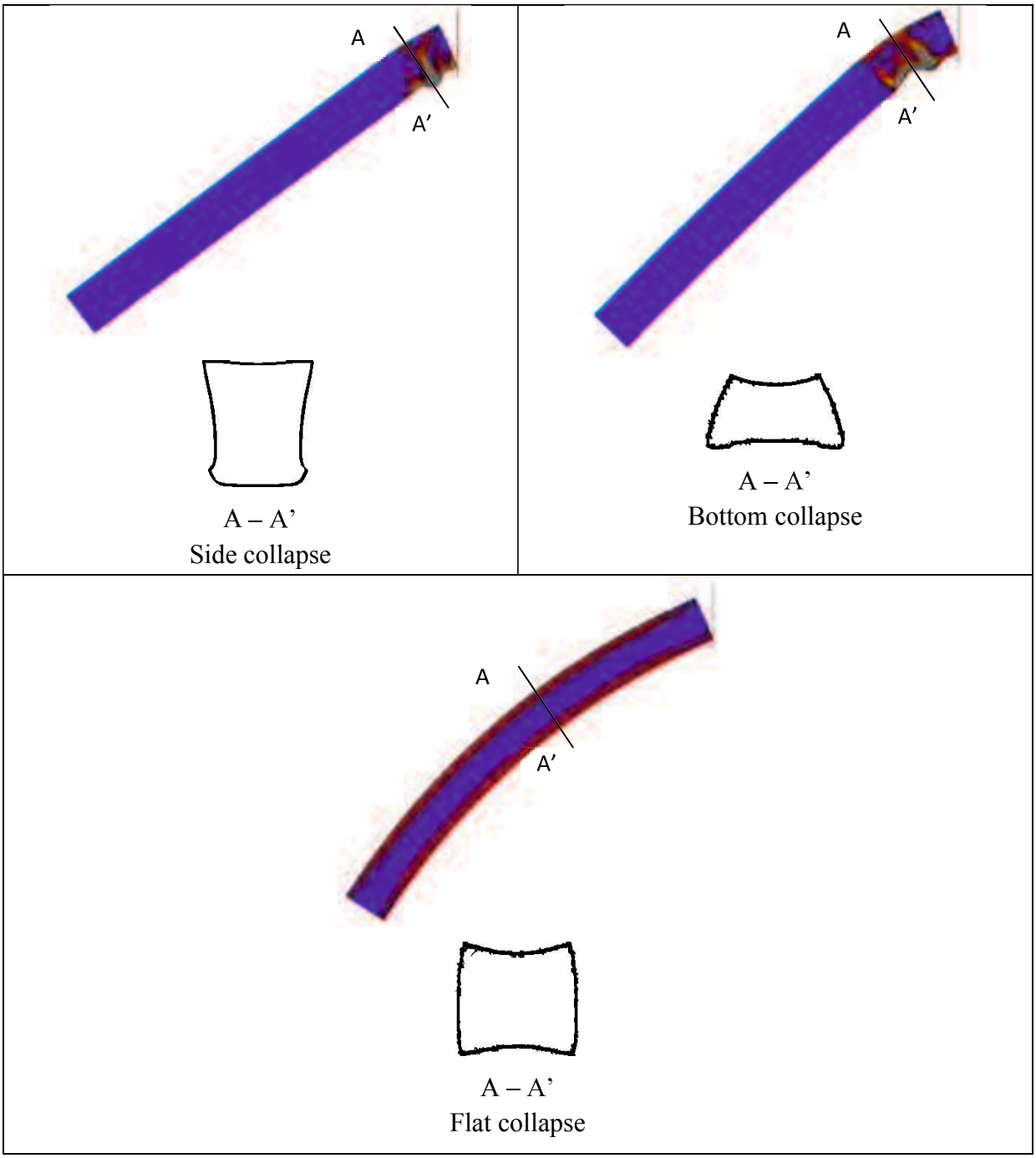

Figure 5.16. Comparison deformation shape of square tube.

From Figure 5.16, it can be seen that the buckling type locally concentrates the strain, whereas the flat type has the distortion occurring in the wide range. Influence on the amount of energy absorption due to the presence or absence of a spring obtained at figure 5.17.

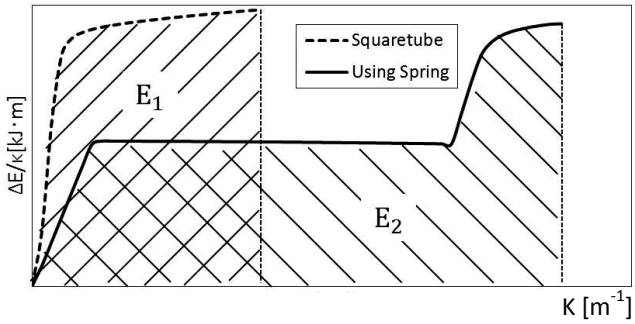

Figure 5.17. Influence of crash-box at square tube bending.

Figure 5.17 shows the relationship between the increment of energy and the curvature in a rectangular. From this, it can be seen that applying the spring increases the amount of deformation required until the collapse, but the maximum value of the energy increase is decreasing.

In order to confirm this fact, the changes of the total energy absorption amount and the spring work increment ΔE/κ, ΔW/κ in the bottom type and the flat type are shown in figures 5.18 and 5.19.

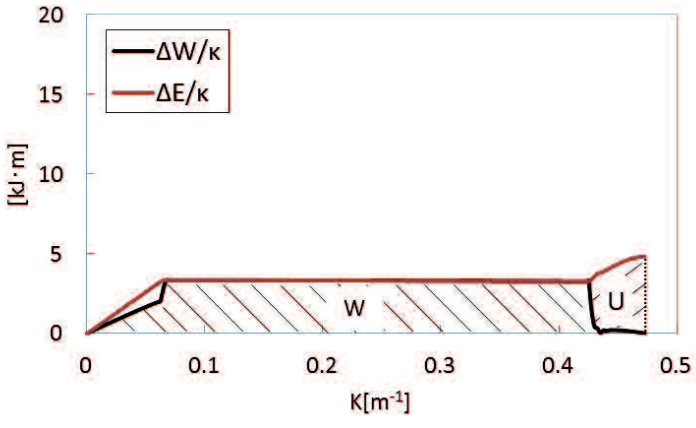

Figure 5.18. Absorption energy at side collapse mode.

In the flat type, the strain energy increases due to deformation of the spring. Then spring deformation continues decrease then deformation at tube start occurs. Result of the total energy absorption increase until collapse.

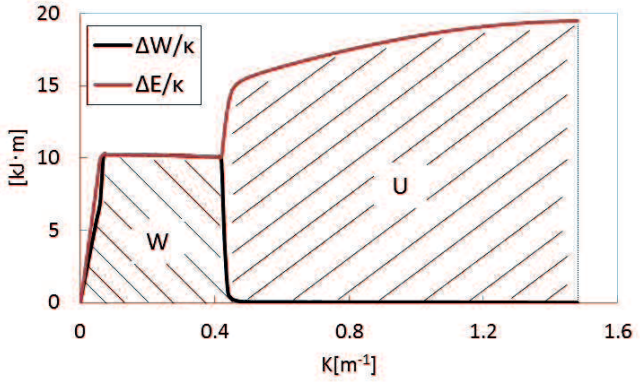

Figure 5.19 Absorption energy at flat collapse mode.

Deformation at side collapse mode shows contrast result than flat collapse mode. According to figures 5.18 and 5.19, relation between the spring work W and the strain energy U at flat collapse is W<U. The bottom collapse is W>U. Therefore, it can be said that the bottom type has a potential area of absorption energy applying the spring.

Further search then pointing at square tube with spring force F = 0,2Pcr and F = 0,6Pcr. Figure 5.20 shows the energy increment ΔE/κ and the increment ΔW/κ of spring work up to the collapse at two spring force amount. It seems that the transition of ΔE/κ and ΔW/κ has different pattern of increment energy.

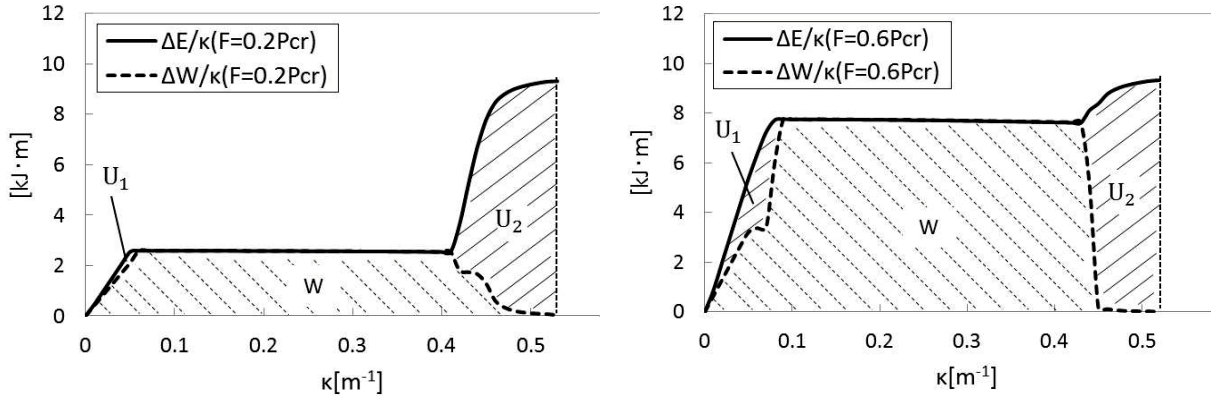

(a). Energy-Curvature curve at $F=0.2P_{cr}$. (b). Energy-Curvature curve at $F=0.6P_{cr}$.

Figure 5.20. Comparison energy between $F=0,2P_{cr}$ and $F=0,6P_{cr}$.

Since the strain energy U at this time becomes larger while F becomes larger, it is considered that the amount of the energy increase becomes different. Comparing the energy absorption, it is obvious that the energy absorption amount ($E = W + U_1 + U_2$) also increasing. Since the strain energy U ($= U_1 + U_2$) up to the collapse is not affected by the magnitude of F, the difference in energy absorption is determined by the work W by the spring.

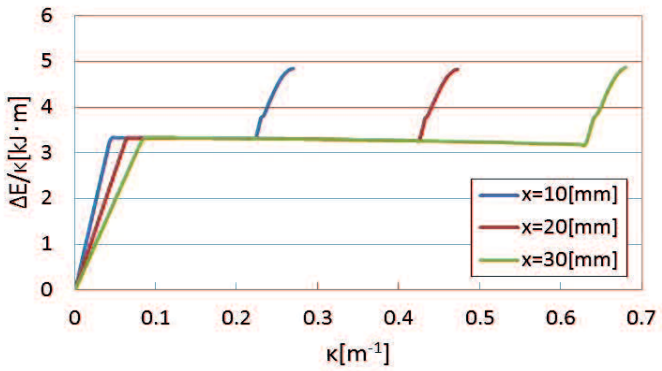

Figure 5.21. Energy characteristic due to change (x).

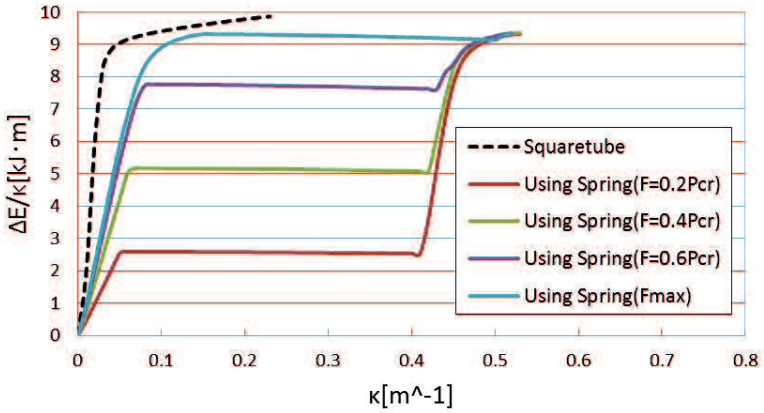

Figure 5.22. Increase total energy using F_{max} .

Also exploring for the relationship between the amount of energy absorption and deformation behavior to some extent functions (the elongation of the spring reaches x). The energy absorption becomes possible to absorb more energy when the rectangular tube deforms more base on x amount. See figure 5.21.

The increment of the total energy absorption rate ΔE/κ increases while spring force (F) becomes higher. It is a possible to increase total energy since it was affected by spring force (F). Using spring force ($F = F_{max}$) it produces new deformation and highest total energy even applied at low thickness ratio (t/C_1). See figure 5.22.

Figure 5.22 shows that square tube using (F_{max}) produces higher energy compares with determined spring force (F). Even, when it applied on low thickness ratio energy absorption is still higher than the others.

5.5 Conclusion

This chapter study about bending characteristic of square tube using finite element analysis. Deformations due to bending at square tube obtain in three deformation mode. Buckling obtain at square tube causing bending capacity reduce. The concept delay buckling was introduce in this chapter using absorption energy part to improve square tube. According to finite element analysis of square tube using absorption part the conclusion of this study are:

1. Square tube with lower spring force produce longer elongation and reduce buckling point at same condition than the others.
2. Collapse mode on square tube due to bending was divide into 3 condition; side collapse, bottom collapse and flat collapse mode. Buckling was occurs at side and bottom collapse, but not occur at flat collapse mode.
3. Square tube with higher spring force produces better energy absorption compares with the others at type 1 collapse mode.
4. It is possible to increase square tube energy even when using low thickness ratio by install new spring force (F_{max}) which resulted higher energy. In other word square tube with absorption part prove that it is able to increase energy absorption at bending test.

CHAPTER VI

OPTIMIZED DESIGN OF CAB FRAME TO IMPROVE ENERGY ABSORPTION PERFORMANCE

6.1 Introduction

Safety is the most important issue on the environment. Heavy equipment such as excavator should comply with safety standard procedure [3]. Design of cab frame in rollover protecting structure (ROPS) should pass the standard to protect human during accidents. The inner area of cab frame was design as a strong shelter withstands the kinetic energy. Whole structure should able to absorb the energy so it will minor effect to the operator [13], [52].

Design of cab frames should aim at absorption rollover energy without sacrificed strength and stiffness [14]. Cab frame undergo high deflection was not appropriate to absorb energy due to buckling phenomenon [5]. ROPS mainly not equipped with special part to absorb collision energy except for the structure itself. Standard for evaluating ROPS performance was first developed in Sweden in the 1950s [53], it regulates agricultural tractors. There are several types of ROPS such as two-post ROPS, four-post ROPS, and enclosed cab [54]. Cab was assembled by bundle of tubular bars which connected by various joining method. Performance of cab frame should pass the standard test. The SAE static test was developed to collect data for determining whether structures are reliable and accurate [55]. The static test considers succeed if ROPS absorbs predefined level of energy and tolerate particular load without obtain any member rupture.

The testing method which performs real vehicle roll-over tests is close to the real accident, it provides the basic and comprehensive method for evaluating vehicle performance [2]. But, it is poor repeat ability and each test needs high cost and time-consuming [6]. Increasing energy absorption by modifying member with a various shape is a potential method. [27] Reported that bending of rectangular hollow was influenced by material parameters such as yield stress, strain hardening, and thickness of the tube.

Khorsandi [12] conducted research by modeling the two-post ROPS for static test using finite element simulations. They develop and evaluate the model to predict nonlinear structure behaviour to enhance vehicle safety. Further research in modeling full geometry of the cab frame led by Haruyama [9], obtained that characteristic of the cab frame was influenced by thickness combination and wrinkle which can reduce energy absorption.

Several researchers was developed cab frame for rollover test according to the specific companies design and conducted an FEA analysis to obtain ROPS behaviour [11], [10].

This research objected to performing optimized model of cab frame using combination of thickness of each bar. Those combinations were arranged using design experiment Taguchi. Finite element model was simulated using MSC Marc software to produce the highest energy absorption which valuable for prototyping development.

6.2 Geometry Model of Cab Frame

This research develops model for cab frame according to basic shape for general purposes. Several researchers developed finite element to predict cab frame behaviour based on the organization for the Economic Co-operation and Development (OECD) [56]. The model will represent quadrilateral element type which represents a cab frame in finite element. Cab frame model can be seen at figure 6.1. Numerical analysis conducted using MSC Marc software for static test.

Material properties of cab frame are considered homogeneous and isotropic of elastic-plastic. Work hardening of material is following bilinear isotropic hardening in uniaxial stress. Stress-strain relationship is assumed according to equation (6.1). Material properties of cab frame explain at table 6.1.

$$\sigma = E \times \varepsilon \qquad \left[\varepsilon < \frac{\sigma_y}{E.\varepsilon}\right] \qquad (6.1)$$

$$\sigma = \sigma_y + E_h\left(\varepsilon - \frac{\sigma_y}{E}\right) \qquad \left[\varepsilon > \frac{\sigma_y}{E.\varepsilon}\right] \qquad (6.2)$$

Where E is Young's modulus, Eh is the work-hardening coefficient, and σ_y is the yield stress.

Table 6.1. Material properties of cab frame model.

Properties	Unit	Value
Young Modulus [E]	GPa	205.9
Poisson ratio [υ]	-	0.3
Yield Stress [σ_y]	MPa	205.9
Work hardening modulus [E_h/E]	-	1/100

Finite element model of cab frame is quadrilateral, where 1 element consists of 4 nodes. Element type of cab is shell type and the thickness as the parameter. Meshing size is 10x10 [mm]. MSC Marc registers this finite element as ID class Quad4 type 75.

Simulation process considered as static condition, simulation control is displacement and starts from point of rigid body. Total displacement of rigid body is 500 [mm], and incremental step is 2 [mm]. The rigid body acts as a ground pressure to cab in rollover condition. Simulation will stop when 1 cycle time is complete in 500 [mm] within 250 steps. Outputs of simulation are rigid body load in [kN] and displacement in [mm].

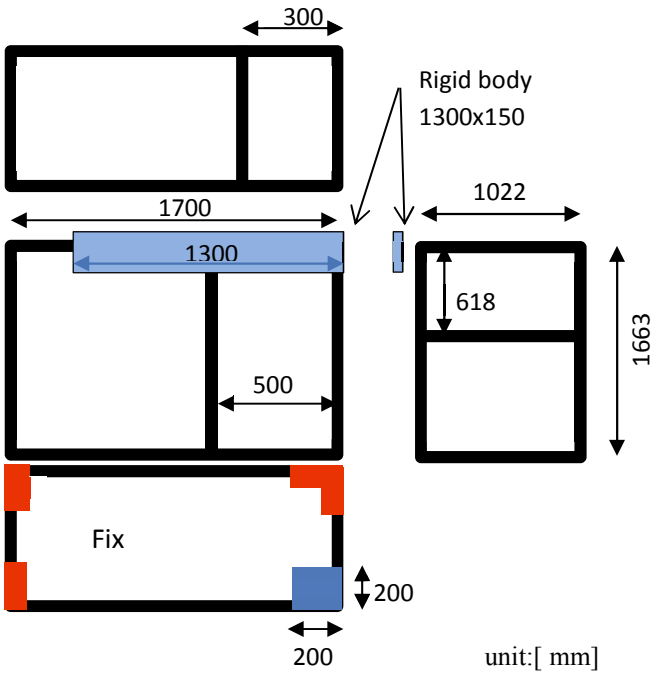

(a). Cab frame boundary condition.

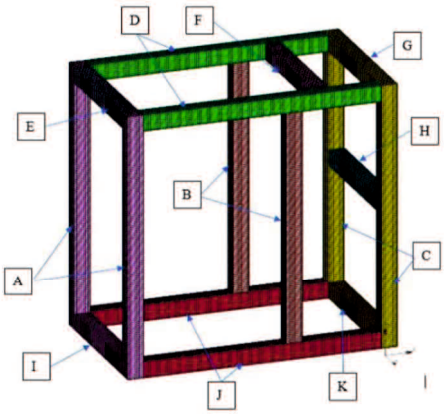

(b). Cab frame model

Figure 6.1. Cab frame model for simulation.

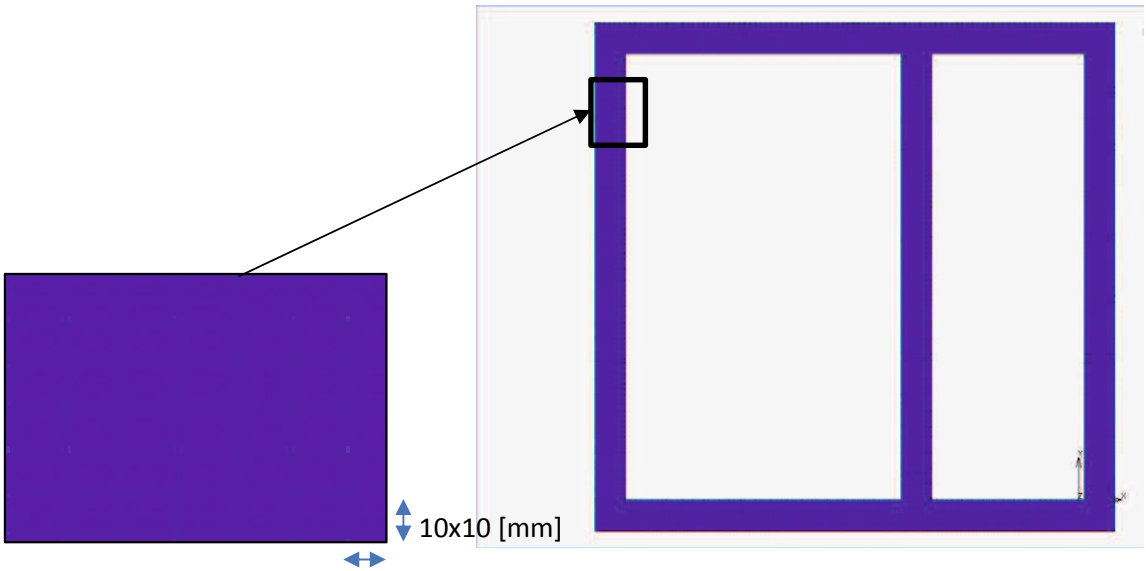

Figure 6.2. Finite element model of cab frame.

6.3 Design Experiment Taguchi

Based on Taguchi's orthogonal arrays, combination of thickness consist of 2 thickness levels and 11 factors. Thickness level 1 is 2 [mm] and level 2 is 4 [mm], number of bar assembly (A-K) is the total of factors. There are 12 finite element simulations conduct in MSC Marc. See table-2 for composition of Taguchi's orthogonal array.

Table 6.2. Thickness condition of parts according L12 orthogonal array.

Pillars / Specimens	A	B	C	D	E	F	G	H	I	J	K
L12-1	2	2	2	2	2	2	2	2	2	2	2
L12-2	2	2	2	2	2	4	4	4	4	4	4
L12-3	2	2	4	4	4	2	2	2	4	4	4
L12-4	2	4	2	4	4	2	4	4	2	2	4
L12-5	2	4	4	2	4	4	2	4	2	4	2
L12-6	2	4	4	4	2	4	4	2	4	2	2
L12-7	4	2	4	4	2	2	4	4	2	4	2
L12-8	4	2	4	2	4	4	4	2	2	2	4
L12-9	4	2	2	4	4	4	2	4	4	2	2
L12-10	4	4	4	2	2	2	2	4	4	2	4
L12-11	4	4	2	4	2	4	2	2	2	4	4
L12-12	4	4	2	2	4	2	4	2	4	4	2

Thickness: [mm]

MSC software performed numerical analysis of cab simulation test to obtain ability of cab frame against force and displacements. A rigid wall acts as ground surface which serve

horizontal force contact to cab frame structure when rollover occurred. Therefore, the dimension of the rigid wall is 1300 [mm] x 150 [mm], and displacement of rigid body is 500 [mm] from basic condition to last conditions. Figure 6.3 shows 3D finite simulation result of cab frame.

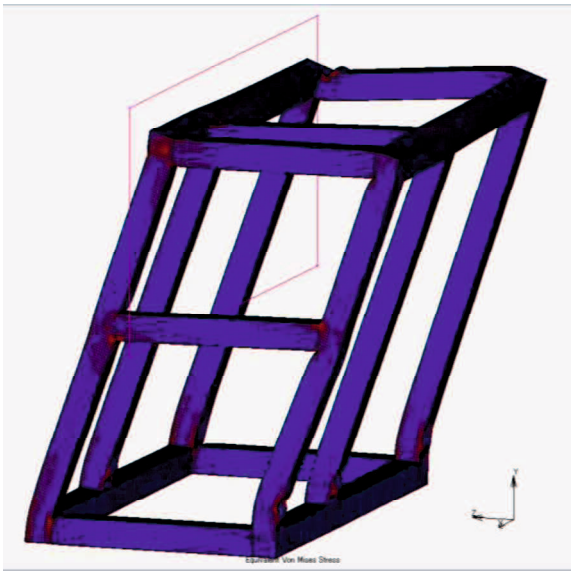

Figure 6.3. Finite element simulation of cab frame.

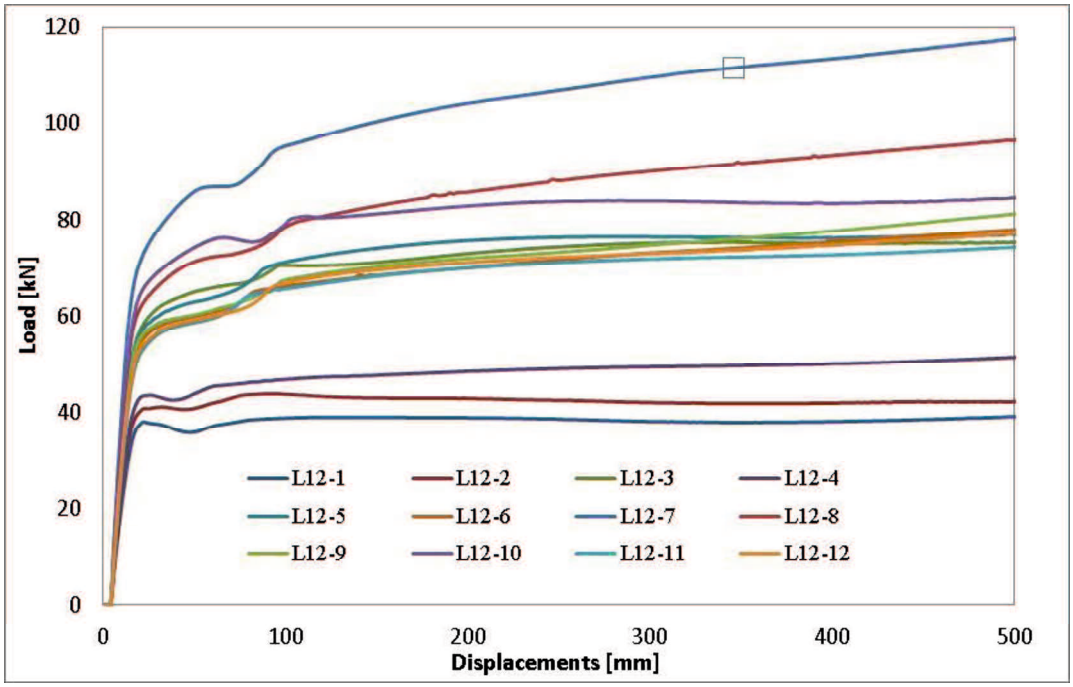

Figure 6.4. Comparison load-displacement curve of cab frame.

Figure 6.4 shows simulation result on load-displacement curve of cab frame against the rigid wall in rollover test. Specimen L12-7 produce the highest strength compare the others. Assembly for L12-7 consist of bars A, C, D, G, H, and J at 4mm thickness and the

others are 2mm. Increasing slope was identical to all specimens until peak level at certain point.

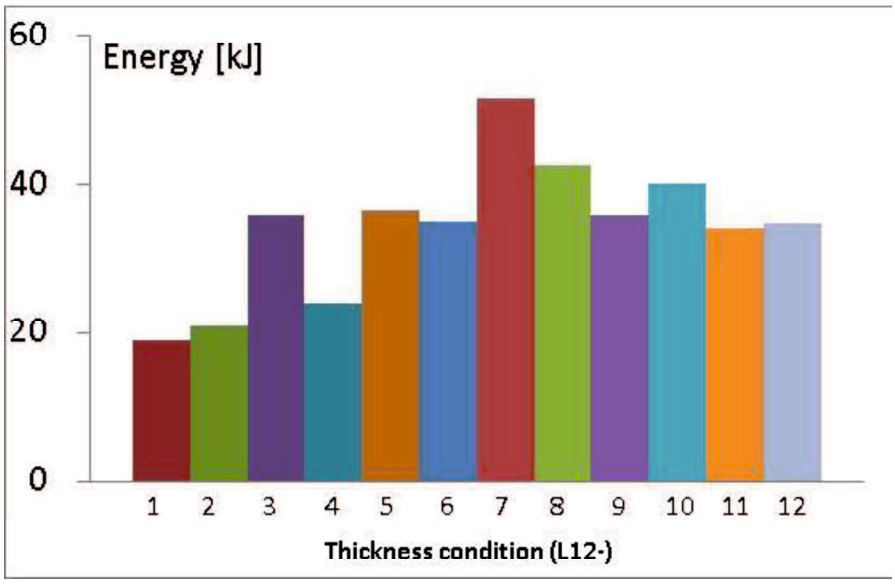

Figure 6.5. Energy comparisons from cab frame simulation.

Specimen L12-7 also produces the highest energy absorption than the others, while specimen L12-1 is the smallest energy absorption. Specimen L12-1 has thickness condition of all bar assembly at 2mm. It is obviously shown that thickness of bar has significant influence on energy absorption during collision. Energy absorption of cab frame for all specimens is shown at figure 6.5.

Based on Taguchi's orthogonal array, specimen L12-7 was reliable to develop into prototyping model of cab frame. Nevertheless, finite simulation still obtained buckling points at certain area of cab frame. Buckling will reduce energy absorption during collision. See figure-5. In accordance to obtain stress distribution at single tube, a set of node was created at cross section area along the axis of the tube. Those nodes were middle point (p), corner point (q), and side point (r). Figure 6.6 shows position of each point at cross section area. In this research C_1 equal with C_2, and thickness-t followed orthogonal Taguchi's array.

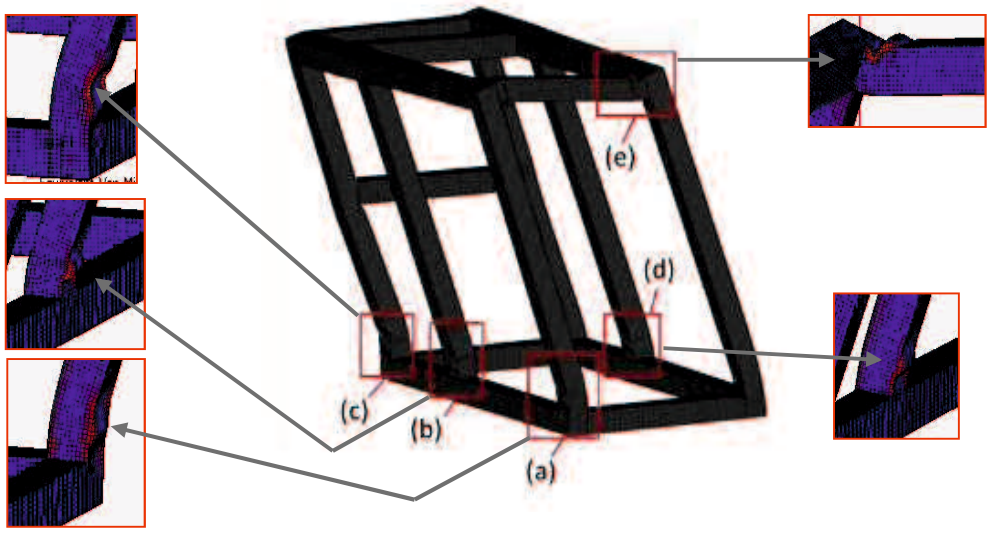

Figure 6.6. Buckling areas at cab frame.

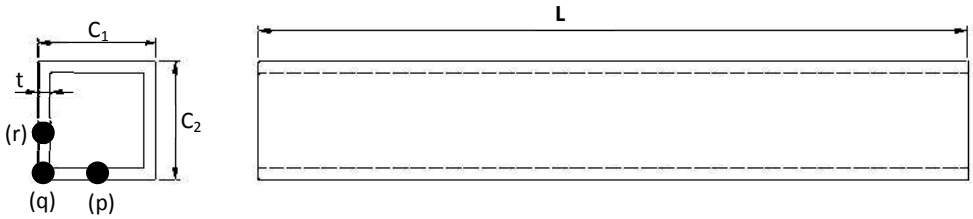

Figure 6.7. Stress distribution of points (p), (q), and (r).

Stress at buckling areas during collision was shown in table 6.3. Those areas indicated a concentration of uneven high stress build up in certain area of material which chosen for simulation. Area (b), (d), and (e) show that specimen needs improvement to increase the ability. See table 6.3 of stress distribution.

Table 6.3 Stress distribution at buckling areas.

Areas	Frame	Stress [MPa]
(a)	A	242,81
(b)	B	203,61
(c)	C	237,19
(d)	B	203,77
(e)	E	151,47

Improvement to increase energy absorption of cab frame was made using optimization pattern of Taguchi's method. Specific average value of thickness level of each bar indicated optimization pattern according to table 6.4.

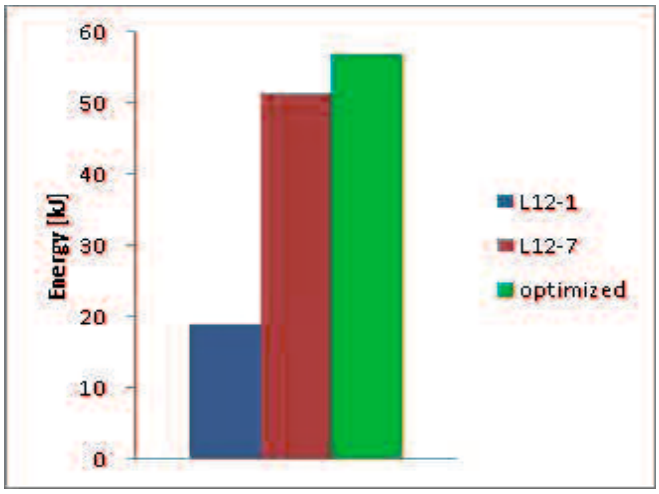

Figure 6.8. Energy comparison of optimized model.

Figure 6.8 shows that optimized specimen has higher energy absorption than L12-7 specimen. Optimized model has 10.4% increase than L12-7, and 199.5% increase than basic model (L12-1).

According to table 6.4, optimized model generated from optimized pattern. Those pattern clarify whether specimen L12-7 corresponding to all thickness level. It is obtained that specimen L12-7 has little difference at bar E level. Optimization pattern indicate of using higher level of thickness level 2 = 4[mm] at bar E while current L12-7 specimen using thickness level 1 = 2 [mm]. New specimen named optimized model was created to perform optimization pattern.

Table 6.4 Optimization pattern of thickness condition on cab frame.

Factors	Levels	Energy [kJ]	Pattern
A	1	28.54	HIGHER A
	2	39.90	
B	1	34.31	SMALLER B
	2	34.14	
C	1	28.17	HIGHER C
	2	40.27	
D	1	32.37	HIGHER D
	2	36.07	
E	1	33.51	HIGHER E
	2	34.93	
F	1	34.27	SMALLER F
	2	34.17	
G	1	33.59	HIGHER G
	2	34.85	
H	1	33.59	HIGHER H
	2	34.86	
I	1	34.65	SMALLER I
	2	33.79	
J	1	32.78	HIGHER J
	2	35.66	
K	1	35.45	SMALLER K
	2	32.99	

6.4 Stress Distribution at Buckling Area

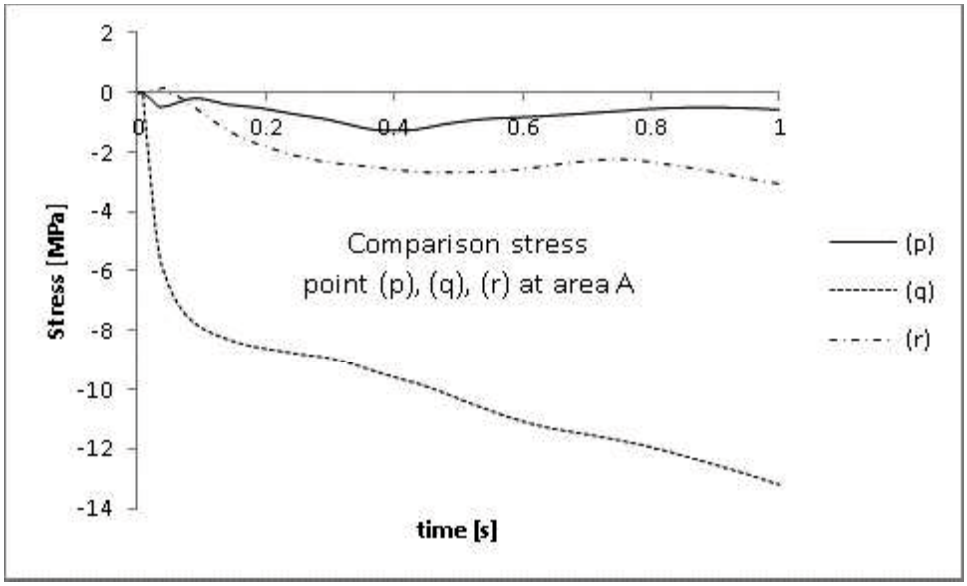

Figure 6.9. Comparison stress at area (a) of optimized model.

Figure 6.9 shows stress distribution at area (a) along three points. It shows that stress at corner point (q) is higher than the other points. This also happens for areas (b) and (d). Different pattern at area (c) and (e), the highest stress was at side point (r). Negative value of stress indicated a compress stress while positive value indicated a tensile stress.

Effect of optimization to stress distribution at three points of whole areas shows significant result. Stress at buckling which occurs before optimized was regenerated by optimization pattern of Taguchi's method.

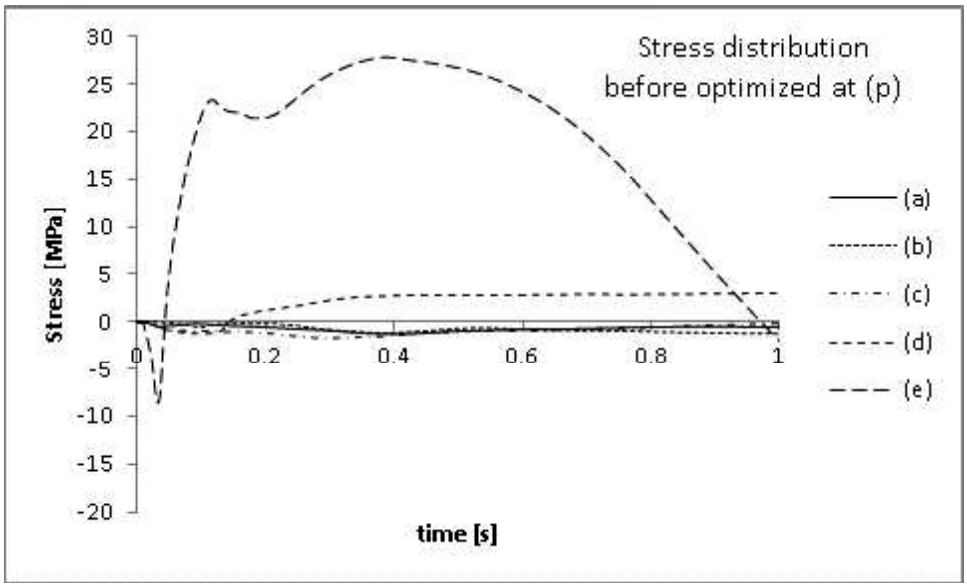

(a). Stress distribution poin (p) before optimized.

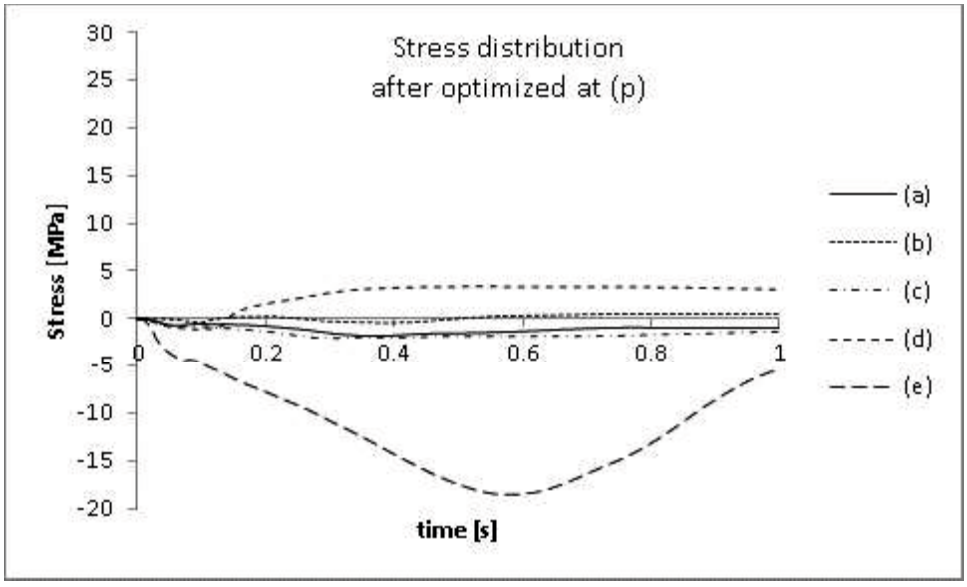

(b). Stress distribution poin (p) after optimized.

Figure 6.10. Stress distributions at point (p) before and after optimized.

Area (e) was significantly improved by optimization pattern. Point (p) before optimized was initially by compression then turn sharply into tensile stress. However, after optimized point (p) start with compression with lower tension than before. Figure 6.10 shows comparison of stress distribution point (p) before and after optimized at all areas.

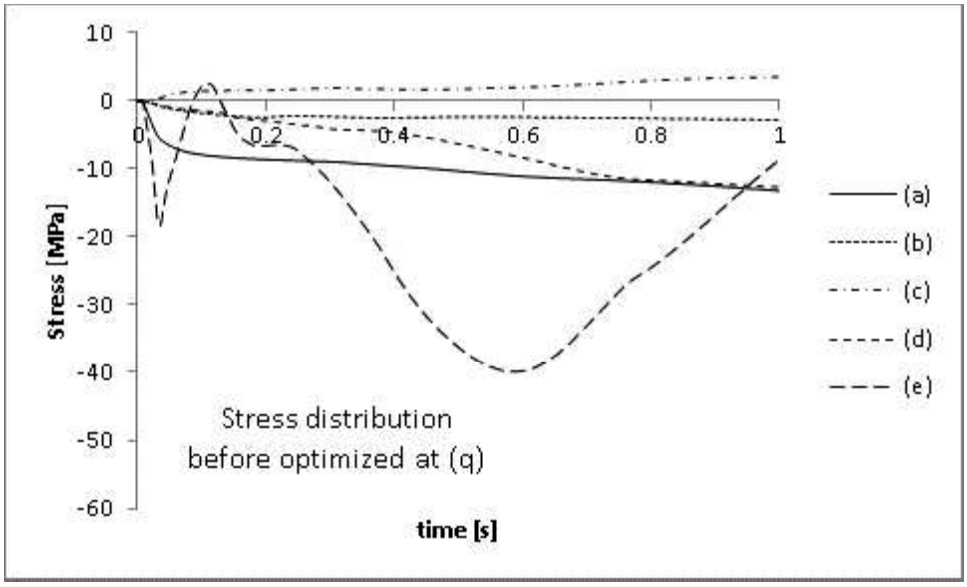

(a). Stress distribution at point (q) before optimized.

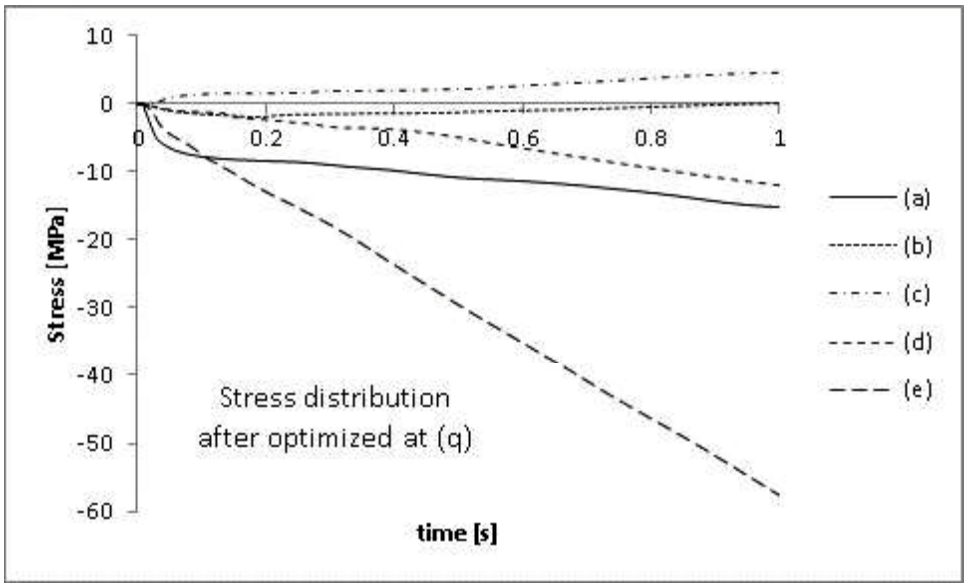

(b). Stress distribution at point (q) after optimized.

Figure 6.11. Stress distribution at point (q) before and after optimized.

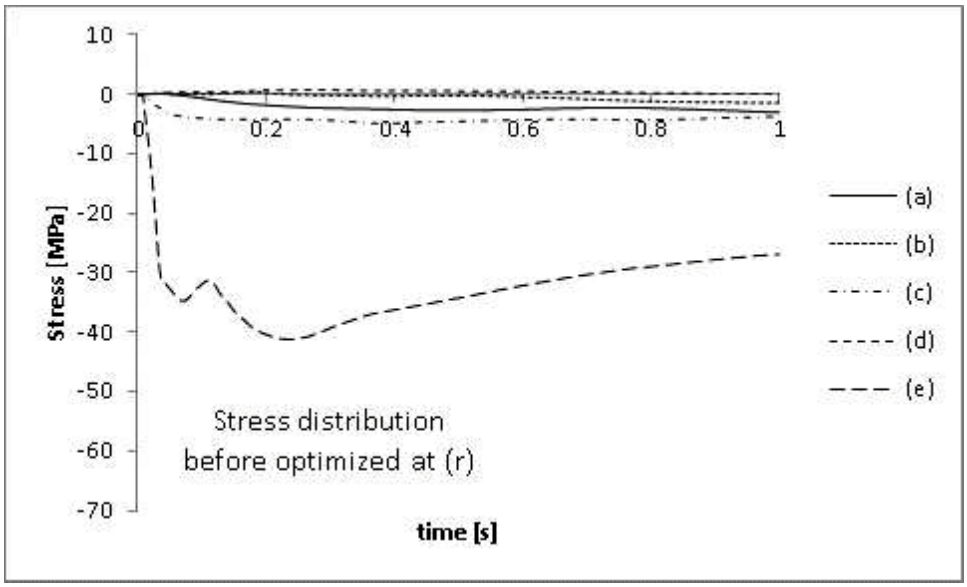

(a). Stress distributions at point (r) before optimized.

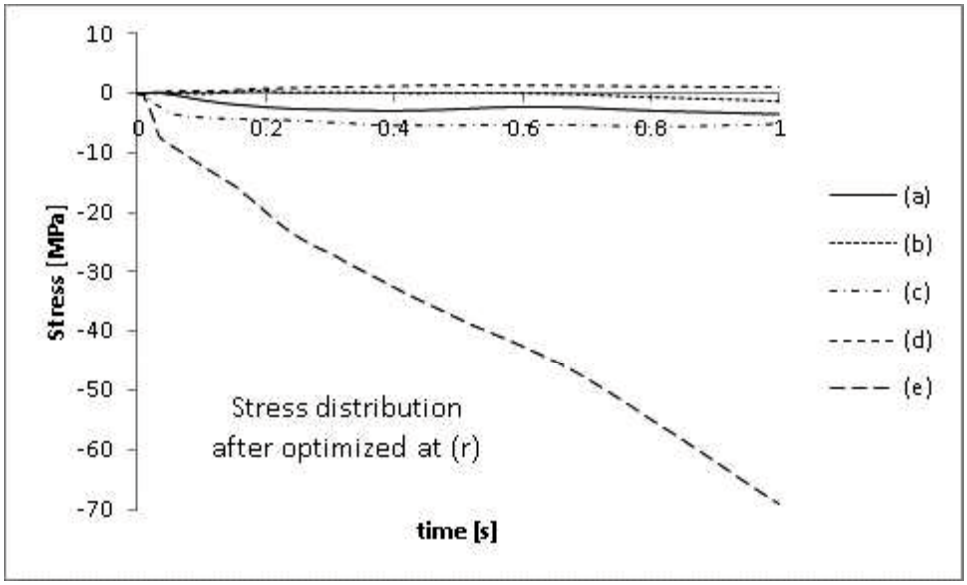

(b). Stress distributions at point (r) after optimized.

Figure 6.12. Stress distributions at point (r) before and after optimized.

Table 6.5. Stress distribution at buckling area after optimized

Areas	Frame	Stress [MPa]
(a)	A	241.96
(b)	B	203.48
(c)	C	237.03
(d)	B	203.59
(e)	E	65.67

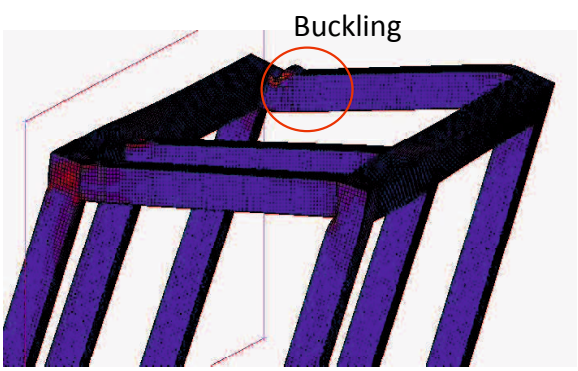

(a). Cab frame occur buckling before optimized.

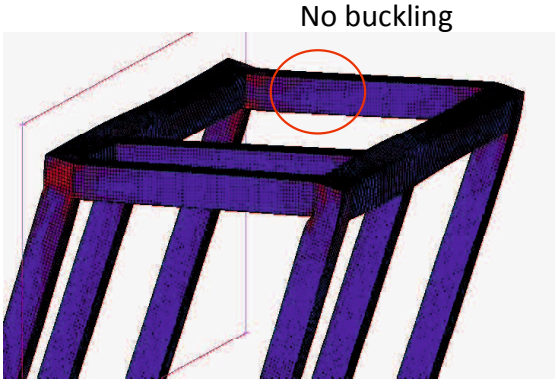

(b). Cab frame no buckling after optimized.

Figure 6.13. Comparison cab frame on pillar E before optimized and after optimized (back view).

Figure 6.11 and figure 6.12 show that point (q) and (r) at area (e) of frame E experienced a considerable change. Stress distribution at buckling areas also influenced significantly after optimized using pattern. As seen on table-5, reduction stress at frame E is a huge drop. Also, on each frame shows similar pattern. This finding indicated that energy from lateral testing was absorbed through all members without excess in specific area. A big difference obtained at frame E on specimen L12-7 after optimized; there was no buckling compare than before. See figure 6.12. Stress at cross section of area (e) after optimized was significantly reduced more than 55%. It seems that optimization reduce buckling at local area.

6.5 Conclusion

The study to improve cab frame performance by optimized thickness condition of cab's pillar using finite element analysis was performed in this chapter. Parameter of thickness condition was used according L12 orthogonal array. Stress distribution at local buckling area was obtained using three observation points (bottom, corner, and side). The result of optimized cab frame was compare with model before optimization and the conclusion of this study are:

1. Thickness of frame was importance factors that can influence energy absorption of cab frame.
2. Stress at several area of cab frame was obtained from three observation point and show under the yield stress of material.
3. Optimization pattern could improve stress distribution at frame E before and after optimization significantly and reduce buckling at frame.

CHAPTER VII

IMPLEMENTATION OF ANALYSIS LED-DESIGN (ALD) IN PRODUCT DEVELOPMENT: STUDY OF CAB FRAME TO IMPROVE ENERGY ABSORPTION PERFORMANCE USING ABSORPTION PART

7.1 Introduction

Cab frame constructed from many types of bar or rod, therefore, specific characteristic of complete assembly was determined by its components. Important points to obtain cab's characteristic are bending and compression strength, those strengths has important role in cab frame collapse condition. Johnson [23] explained about bending rectangular anisotropic elastic beam, a mathematical solution given approach to verify that the bending stiffness is greater when twisting is prevented. Kecman [33] explained that kinematics solution was able to illustrate bending collapse of square section tube. Furthermore, to verify the solution, a series of quasi-static bending experimental of square tube with various shape were conducted. It shows that a good agreement obtained between the solution and experiment. Bending mechanism obtained hinge part which absorb energy by axially collapsing thin walled columns [57], and [32]. Existing methods are then enhanced with new analytical solution that involved two unknown constants determined from minimizing a mean crumpling moment [34]. Further, characteristics of slope deflection for elastic-plastic of multi-frames are investigated by Chi et al. [30]. Assembly of frames could produce additional applied moments, therefore those moments obtained from set of linear algebraic solution which verified by numerical analysis.

Beside square or rectangular shape pillar, cab frame also has cylindrical type pillar. Thin-walled cylindrical tubes for axial impact were investigated by Adachi et al. [4]. Crushing impact test for several cylinders with ribs showed improved energy absorption characteristic. Specific axial crushing of multi compact-impact member to substitute conventional thin-walled cylindrical tube improved load efficiency characteristic. A similar study also conducted for cylindrical tube for axial crushing test called compress-expand member tube. Collapse modes of those members showed stable deformation than single cylindrical tube, therefore energy absorption also increases due to wider range of absorption area [58], and [59].

The comprehensive analysis of vehicle safety device to protect rolling accident was following safety standard procedure ISO 3471 [3]. Roll over protecting structure called ROPS was standard device for protecting operator when collision happens. Various types of ROPS were tested according to standards SAE 2009 [55], and ISO 3471 [3]. Real collision test was the most reliable method to verify ROPS, but it requires huge effort to conduct [6]. There was difficult to predict mathematical solution precisely on crushing load when roll over, due complexity of ROPS assembly and nonlinear characteristic of material [15]. Finite element analysis was ideal to obtain deformation load and perform up-front engineering approach. This method is fully integrated in Analysis-Led Design (ALD) phase [60]. Design of two-post ROPS using finite element analysis showed that buckling could happen due to non-uniform distribution of bending load which concentrated at specific area [12].

This research aims to optimize energy absorption performance of cab frame using series of improvement combinations. Those improvements were arranged using design experiment of Taguchi's method. Series of improvement was adopted from previous researches. It consists of modification of frame, and install new absorption device placed inside cab frame. Result of improvement compared each other to find the highest energy absorption. Finite element method was performed using MSC Marc software to produce simulation and numerical analysis.

7.2 Finite Element Analysis of Cab Frame

Cab frame model was constructed as general shape, used rectangular bars with six-post vertical pillars. Meanwhile, basic shape of frame, which composes full cab frame, was rectangular (C_1=C_2). Finite element model represents quadrilateral element type. Material properties are considered as homogen isotropic elastic-plastic. Work hardening of plasticity material follows bilinear isotropic hardening in uniaxial stress. Roll-over standard test considered as static circumstance according to the International Standardization and Organization (ISO) [3] and, Organization for European Economic Co-operation (OEEC) [53]. Stress-strain relationship is assumed according to equation (7.1) and (7.2).

$$\sigma = E \times \varepsilon \qquad \left[\varepsilon < \frac{\sigma_y}{E.\varepsilon}\right] \qquad (7.1)$$

$$\sigma = \sigma_y + E_h\left(\varepsilon - \frac{\sigma_y}{E}\right) \qquad \left[\varepsilon > \frac{\sigma_y}{E.\varepsilon}\right] \qquad (7.2)$$

Detail of material properties of cab frame are listed in Table 7.1.

Table 7.1 Material properties of cab frame

Modulus Young [E]	205.9 [GPa]
Poisson ratio [v]	0.3
Yield stress [σ_y]	E/1000 [MPa]
Hardening ratio [Eh/E]	1/100

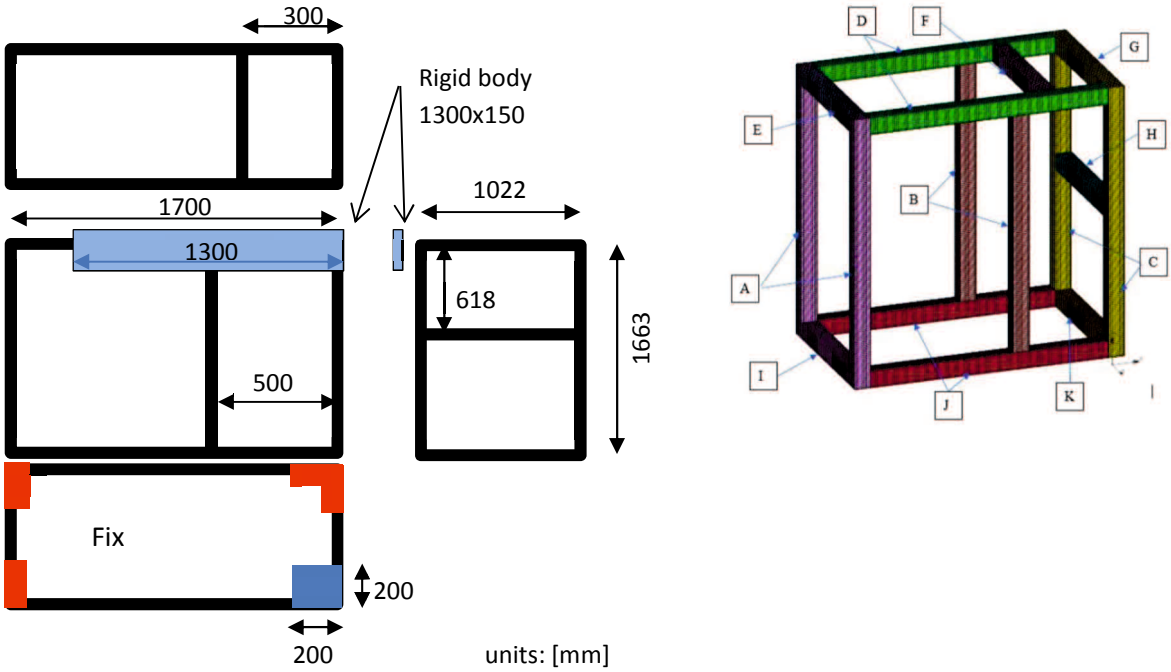

(a). Cab frame boundary condition. (b). Cab frame model.

Figure 7.1. Cab frame boundary condition and cab frame model.

Finite element model of cab frame is quadrilateral, where 1 element consists of 4 nodes. Element type of ROPS is shell type and the thickness as the parameter. Meshing size is 10x10 mm. MSC Marc [65] register this finite element as ID class Quad4, ID type 75.

Simulation process considered as static condition, simulation control is displacement and starts from point of rigid body. Total displacement of rigid body is 500mm, and incremental step is 2mm. Rigid body acts as a ground pressure to cab's body in rollover condition. Rigid body size is 1300x150 mm, according to ISO 3471: 2008, maximum total length of load applicator point (LAP) is ±0,8 of length ROPS. Simulation will stop when 1 cycle time is complete in 500mm within 250 steps. Outputs of simulation are rigid body load in [kN] and displacement in [mm].

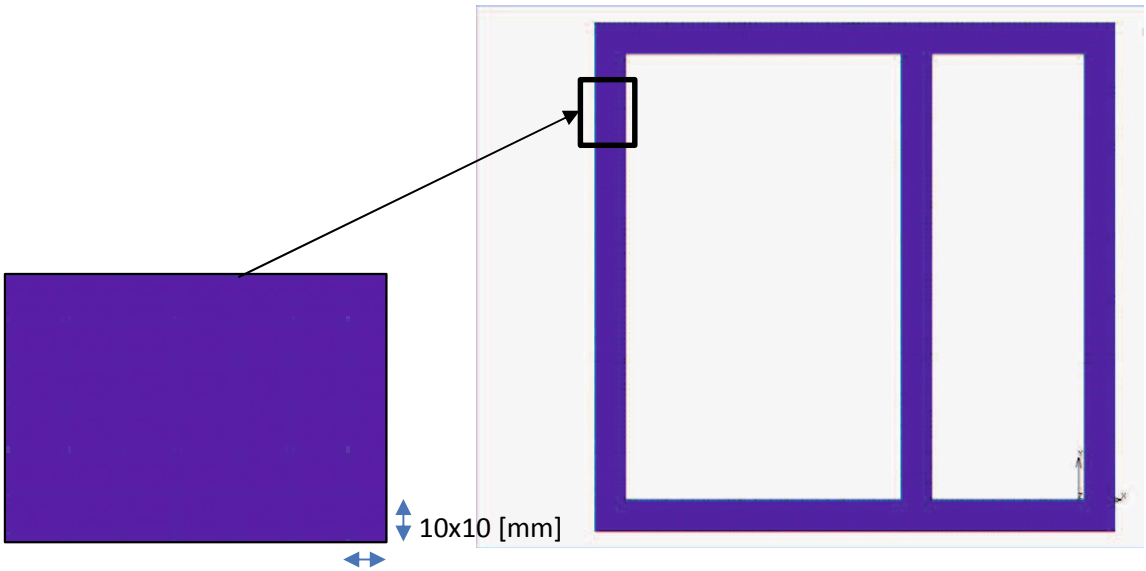

Figure 7.2. Finite element model of cab frame.

Table 7.2. Thickness condition of parts according L12 orthogonal array.

Pillars / Specimens	A	B	C	D	E	F	G	H	I	J	K
L12-1	2	2	2	2	2	2	2	2	2	2	2
L12-2	2	2	2	2	2	4	4	4	4	4	4
L12-3	2	2	4	4	4	2	2	2	4	4	4
L12-4	2	4	2	4	4	2	4	4	2	2	4
L12-5	2	4	4	2	4	4	2	4	2	4	2
L12-6	2	4	4	4	2	4	4	2	4	2	2
L12-7	4	2	4	4	2	2	4	4	2	4	2
L12-8	4	2	4	2	4	4	4	2	2	2	4
L12-9	4	2	2	4	4	4	2	4	4	2	2
L12-10	4	4	4	2	2	2	2	4	4	2	4
L12-11	4	4	2	4	2	4	2	2	2	4	4
L12-12	4	4	2	2	4	2	4	2	4	4	2

Thickness: [mm]

This research is using combination of thickness levels based on Taguchi's method. Thickness level 1 is 2 mm and level 2 is 4 mm, assembly of frame named (A-K) is the total of factors. There are 12 finite element simulations conduct in MSC Marc. Improvement of frame conducted according to previous research:

- Improving bending capacity of rectangular tubes by varying (C_2/C_1) and thickness (t), Masuda et al. [17].

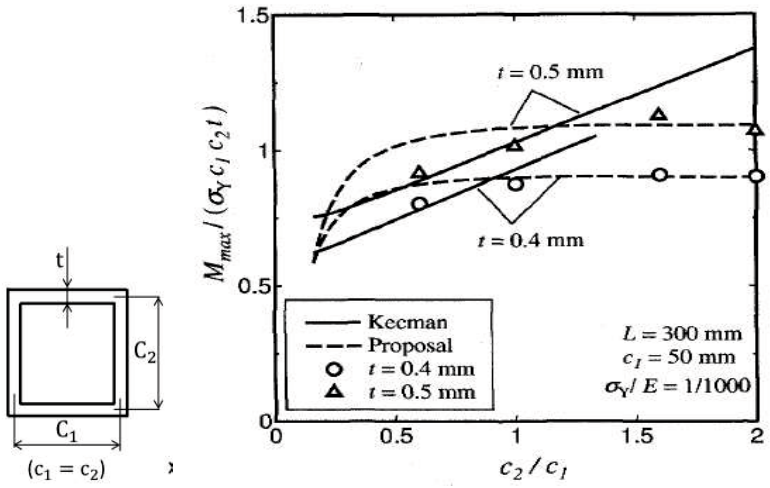

Figure 7.3. Comparison between Kecman's theory and FE analysis [17].

Table 7.3. Parameter for bending improvement.

C_2/C_1	C_2 [mm]	C_1 [mm]
1,5	150	100
1,7	170	100
2	200	100

- Improving axial compress capacity by choosing appropriate thickness to length (b/t), Shinohara et al. [61].

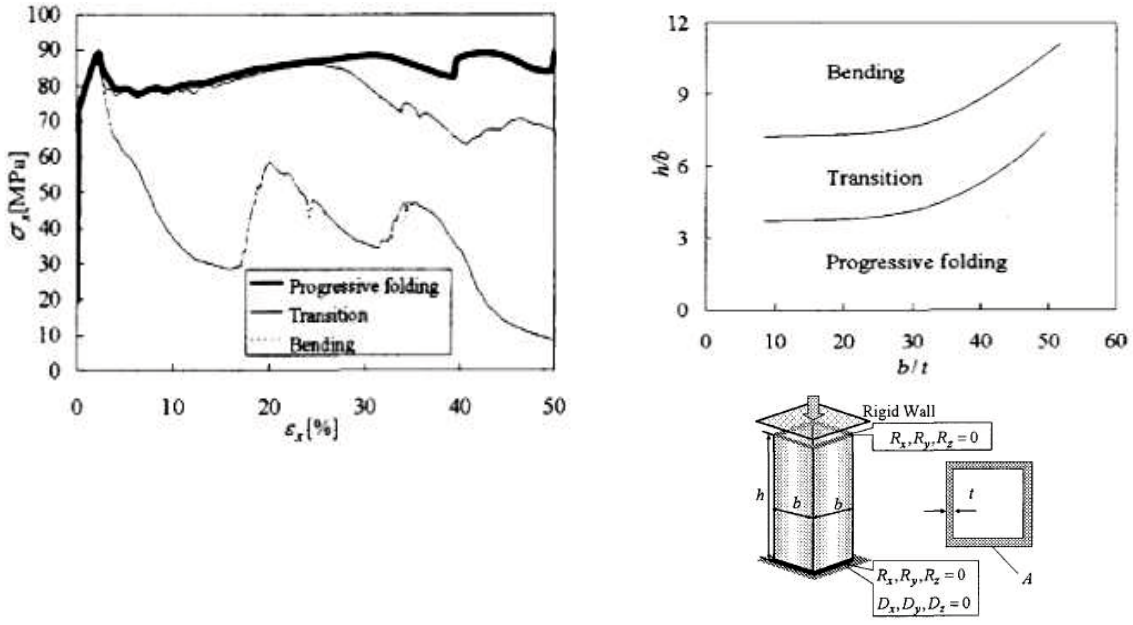

(a). Axial stress-strain curve for rectangular tube.

(b). Deformation mode for rectangular tube.

Figure 7.4. Axial stress-strain curve and deformation mode for rectangular tube [61].

- Reduce buckling by install energy absorption part at certain area, Haruyama et al. [62].

Table 7.4. Parameter for axial compress improvement.

h/b	h [mm]	b [mm]	b/t	t [mm]
5.48	822	150	42.8	3.5
5.48	822	150	50	3
5.48	822	150	75	2

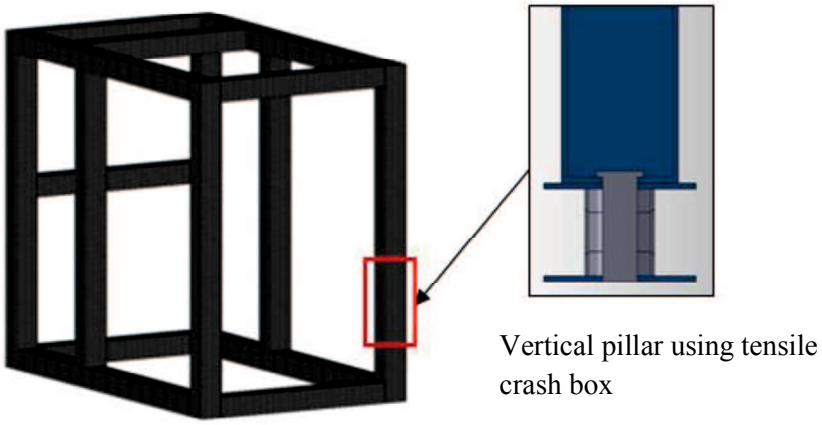

Figure 7.5 Install absorption part at vertical pillar of cab frame

7.3 Improve Absorption Energy by Thickness Condition

Finite analysis performed using MSC Marc to produce side collision of cab frame. A rigid wall created as ground surface similar when rolling happen and produce force to cab frame structure. Therefore, the dimension of the rigid wall is 1300 [mm] x 150 [mm], and total displacement of rigid wall to cab frame is 500 [mm]. Initial ROPS analysis according to Taguchi's method at Table 7.2.

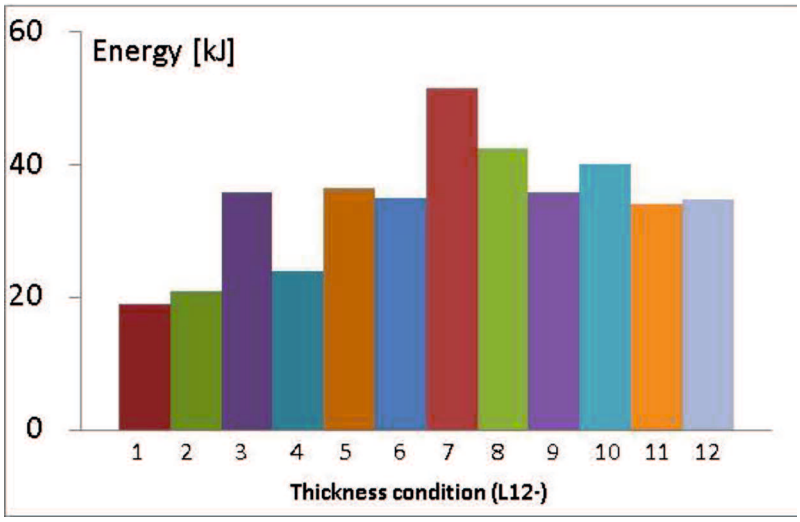

Figure 7.6 Comparison energy of cab frame among the specimens

From Figure 7.6, resulted that L12-7 is the highest energy and L12-1 is the lowest. In that case, thickness condition influences energy absorption. Simulation L12-7 was selected as basic comparison for improvement to verify better result.

7.4 Improve Bending Pillar and Compress Pillar Capacity

Based on table 7.3 and table 7.4, improvement generates simulation to improve bending and compress pillar capacity. Detail of simulation followed table 7.5 and 7.6.

Table 7.5. Improvement of bending and compress.

A,B,C Bending	Level 1	C_2=15mm
	Level 2	C_2=17mm
	Level 3	C_2=20mm
E Compress	Level 1	t=2mm; b=150mm
	Level 2	t=3mm; b=150mm
	Level 3	t=3.5mm; b=150mm

Table 7.6. L9 orthogonal array of improvement bending-compress.

Frame / Specimen	A	B	C	E
L9-1	1	1	1	1
L9-2	1	2	2	2
L9-3	1	3	3	3
L9-4	2	1	2	3
L9-5	2	2	3	1
L9-6	2	3	1	2
L9-7	3	1	3	2
L9-8	3	2	1	3
L9-9	3	3	2	1

Result of improvement on bending and compress pillars then compared with simulation L12-7, this specimen then will be called as default.

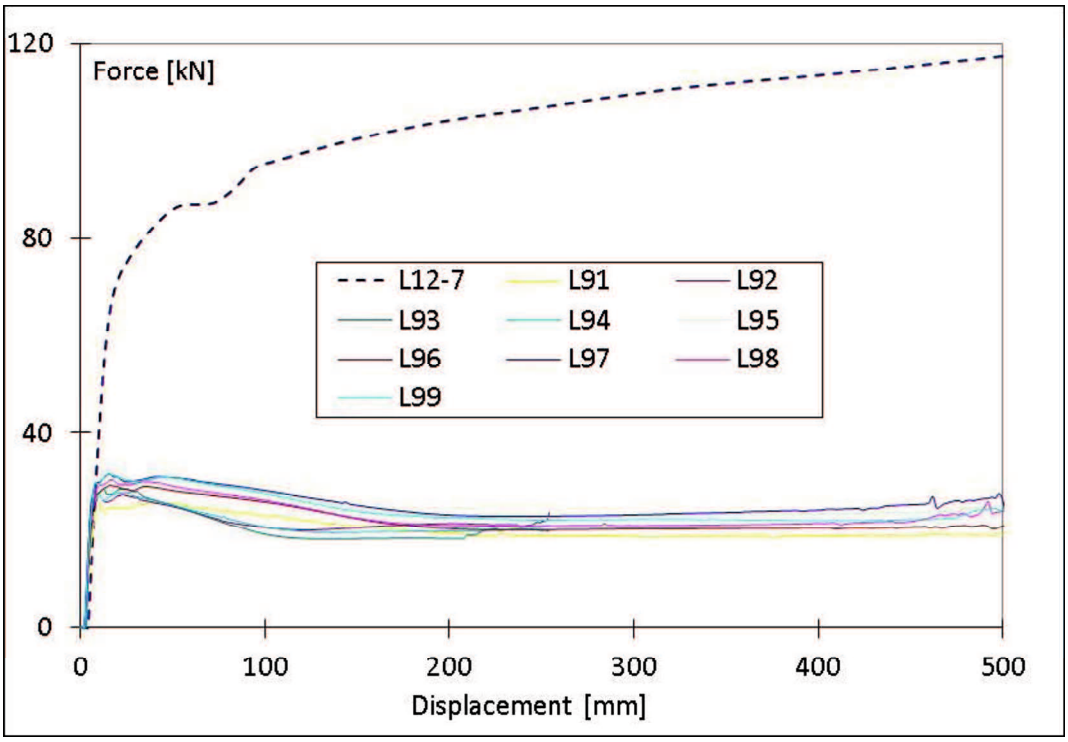

Figure 7.7. Result of improvement bending pillar and compress pillar.

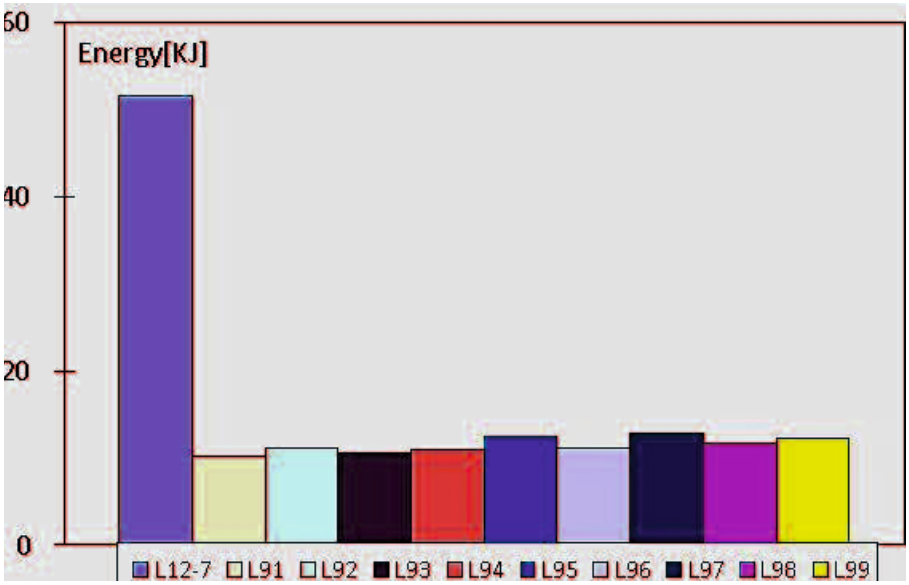

Figure 7.8. Comparison of energy absorption between (L12-7) and improvement bending pillar and compress pillar.

7.5 Improve Energy by Install Absorption Part at Vertical Pillar.

Improvement step divided into several categories. Absorption part will be placed at certain area of cab frame where obtained buckling. Absorption part next called as crash box. Type of absorption part will follow compress-expand tubular tube characteristic.

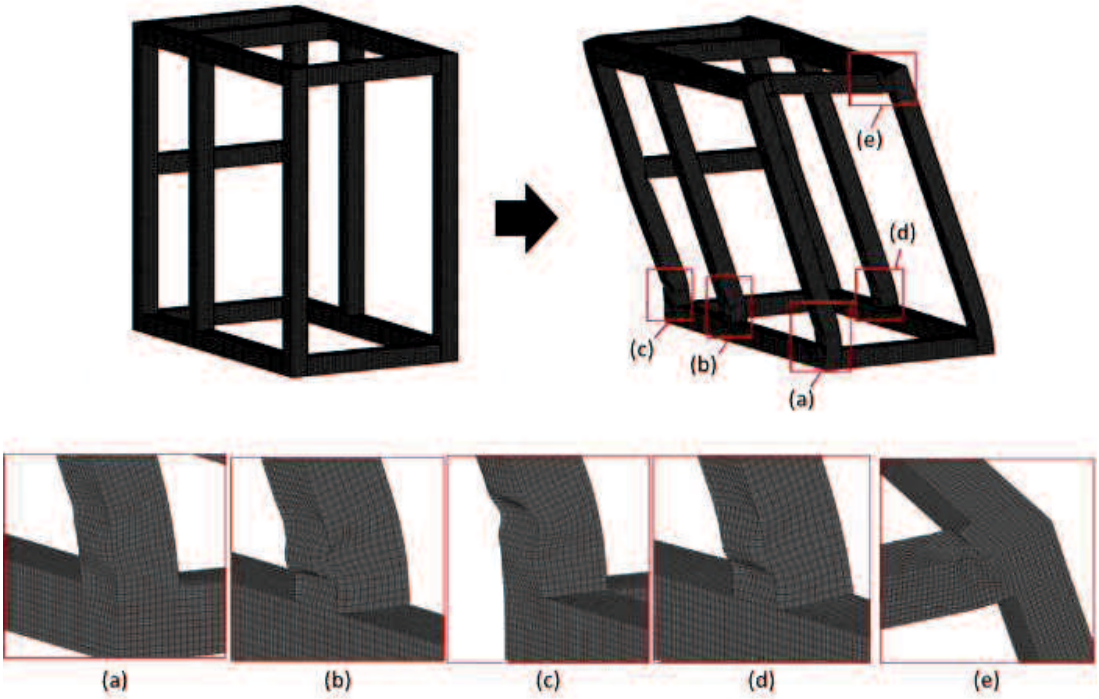

Figure 7.9. Buckling area of cab frame.

According to figure 7.9, absorption part will be placed at 4 improvement locations. Those locations were; lower bottom of frame C; lower side of frames A, B, C; upside of frames A, B, C; and at frame E. Results of install crash box at cab frame are shown in figures 7.11, and 7.12.

Improvement at 7.4 showed that results of improvement are worse than improve the thickness condition. According to study of [53], [35] improvement result should showed better than default. However, previous study was conducted for single square tube, the theory was not applicable when adopted for cab frame which consist of many part.

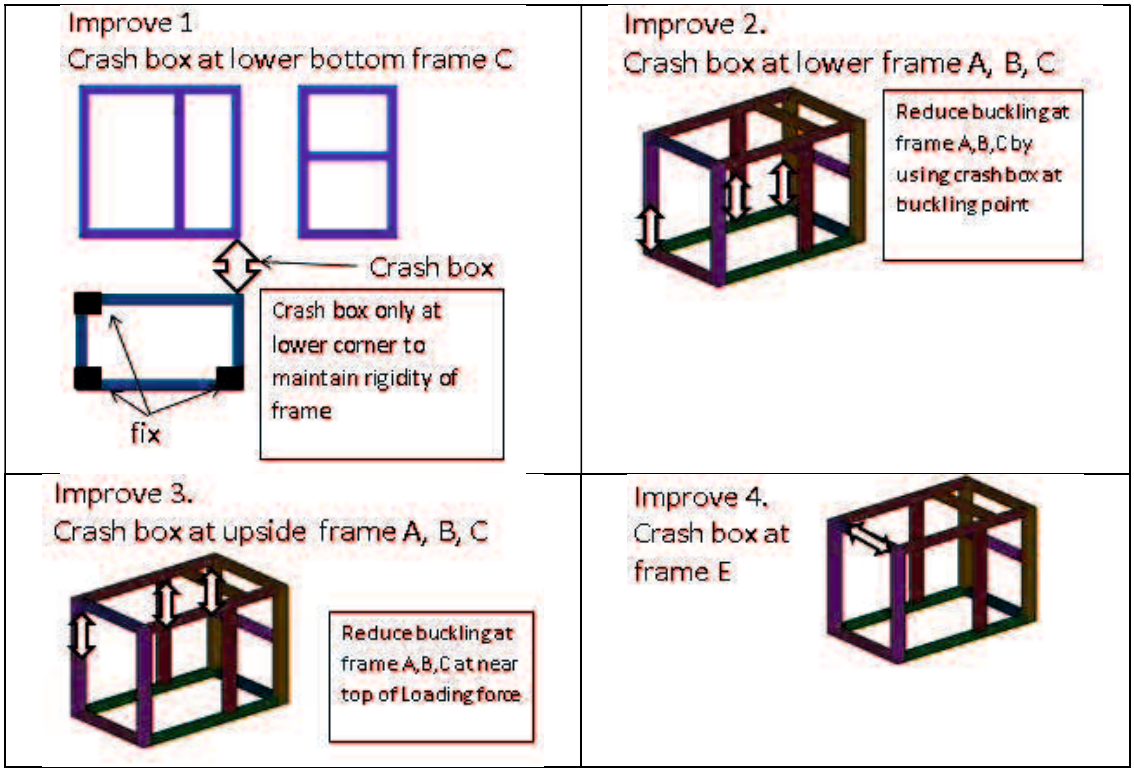

Figure 7.10. Location of install crash box at cab frame pillars.

Those condition also obtain at install crash box at vertical pillar, it showed a little increase about 1.97% than default. This increasing obtained from improvement 3, when install crash box at upside of frames A, B, C. The result was not quite significant and possible to failure due to limitation of crash box design. According to SAE J1040 [63] deformation on cab frame should not exceed deflection limiting volume (DLV) 15°.

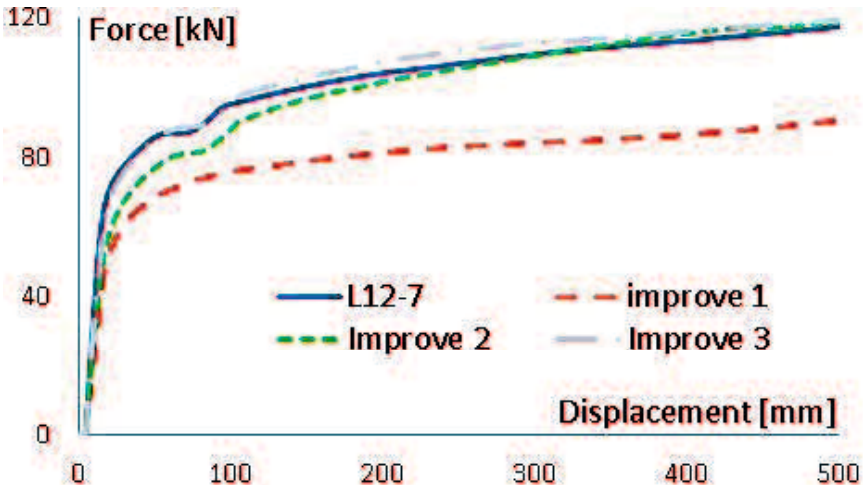

Figure 7.11. Result of load-displacement on install crash box at cab frame pillars.

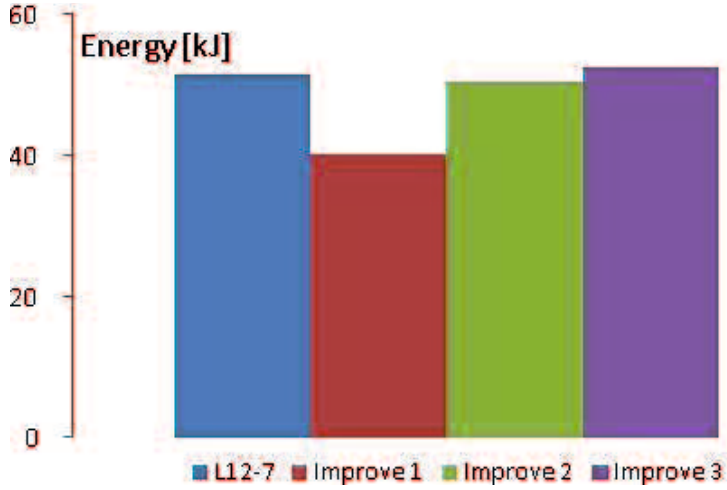

Figure 7.12. Result of energy on install crash box at cab frame pillars.

Design of crash box for single rectangular tube showed that it could improve moment bending and reduce buckling. However that studies condition was no bending angle limitation as in DLV of cab frame. Due to the limitation, crash box design was not compatible if install at cab frame for absorb roll over energy. Crash box for this cab's model only absorb energy at 13 [mm] of stroke length, while it needs more stroke to produce higher absorption.

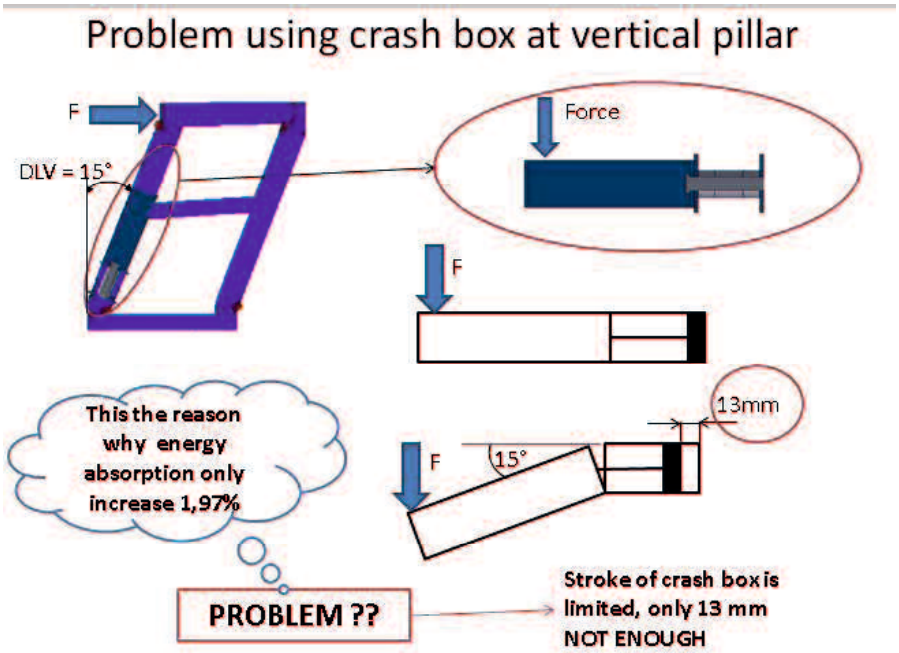

Figure 7.13. Limitation using crash box at vertical pillars of cab frame.

7.6 Tensile Mechanism of Crash Box

Due to the problem exist on bending crash box, the new design of absorption part was developed. New design should enable to absorb energy at such limiting DLV. Basic principal is using tensile stress at rear diagonal side of cab frame. The diagonal side provide enough strokes to absorb deflection energy at cab frame, based on cab's model dimension stroke length was 214mm.

Mechanism of tensile crash box at rear diagonal side of cab frame followed simple tensile at diagonal bar. When cab occurs deflection the bar could stretch because connected between two-posts (left and right pillars). The stretching of bar, and then pulled tensile crash box in opposite direction and crushing the axial compress-expand tube inside the box.

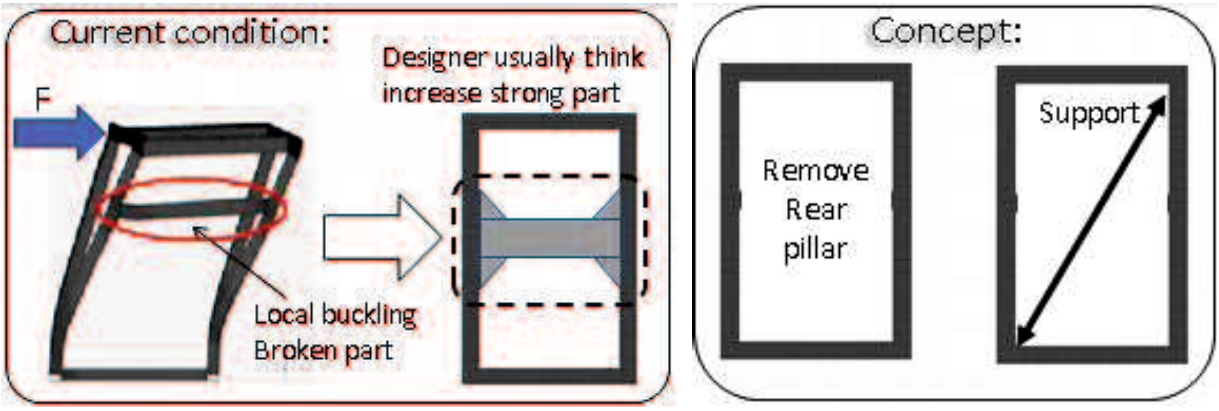

Figure 7.14. New concept of cab frame using crash box.

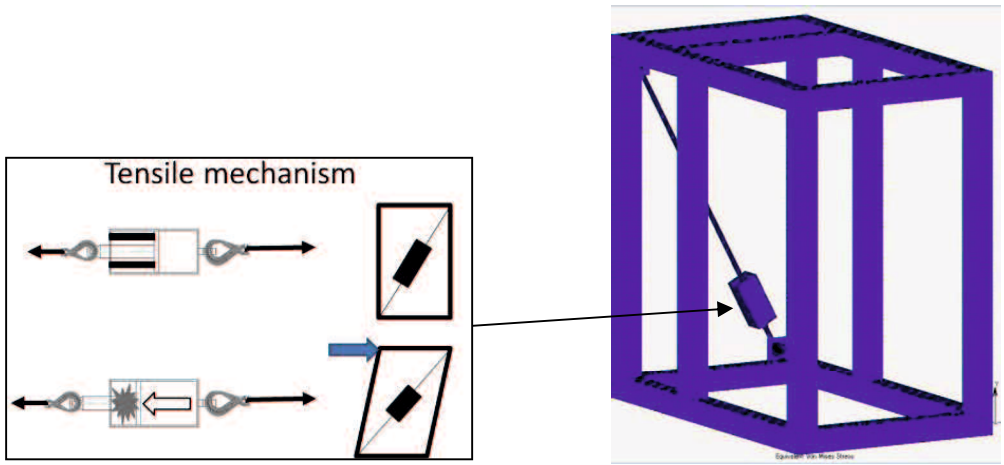

Figure 7.15. Tensile crash box mechanisms.

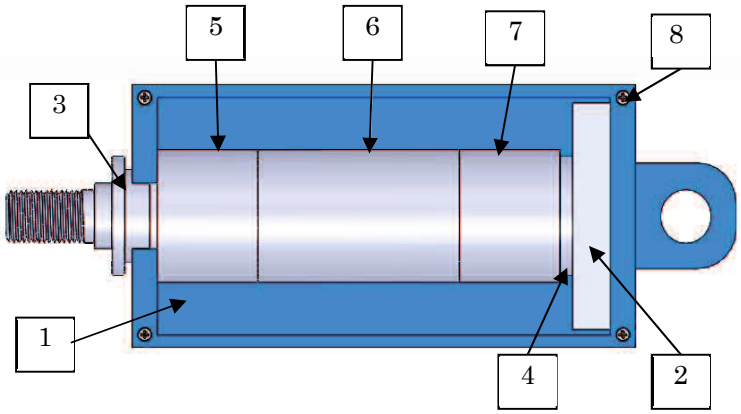

Part-No	Description	Total
1	Case	1
2	Pressure Link	1
3	Guide Bushing	1
4	End Bushing	1
5	Compress 1	1
6	Expansion	1
7	Compress 2	1
8	Bolts - M3 x 0,5 x 20	4

Figure 7.16. Tensile crash box assemblies.

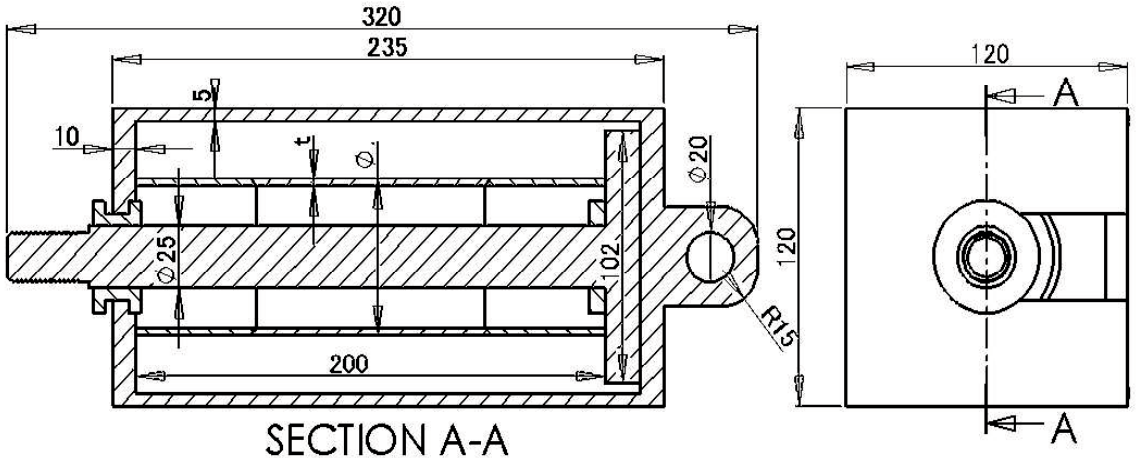

Figure 7.17 Detail design of tensile crash box.

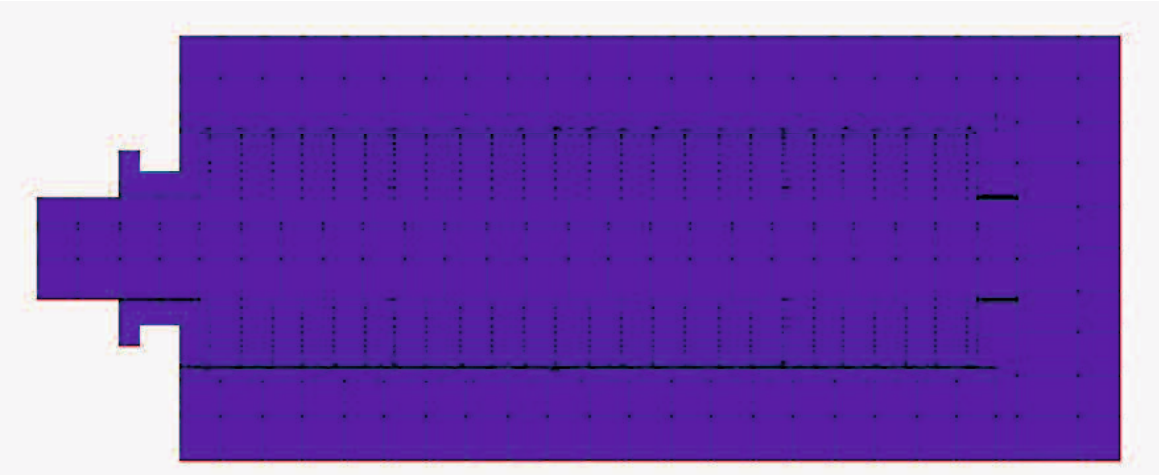

Figure 7.18. Finite element model of tensile crash box with stress tensor.

Finite element model of tensile box is arbitrary hexahedral, where 1 element consists of 8 nodes iso-parametric. Element type of cab frame is solid type. Meshing size is 5x5 mm. MSC Marc registers this finite element as ID class hex8, ID type 7. Tensile box connected to cab using bar, finite element model of bar is line, where consist of 2 nodes between the line. Element type of bar is truss type and the cross section area as parameter. MSC Marc registers this finite element as ID class line 2, ID type 9.

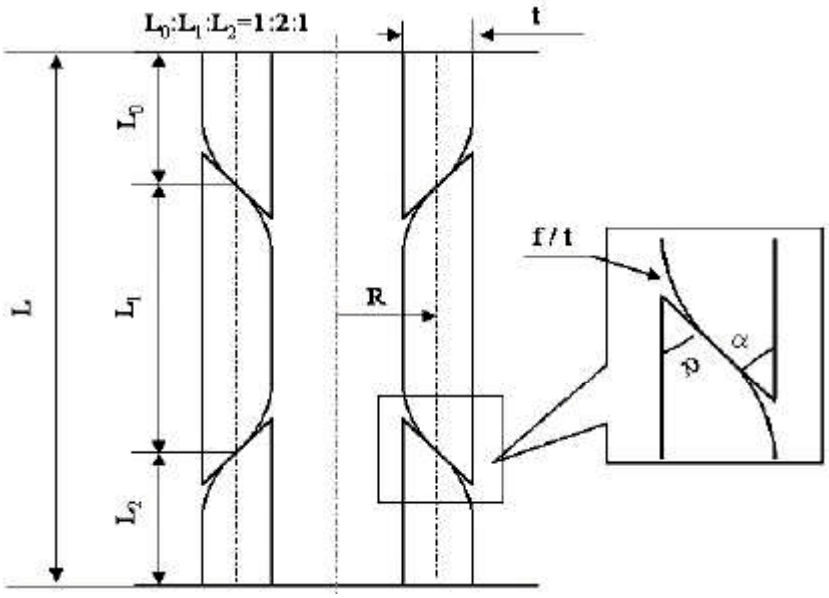

Figure 7.19. Compress-expand tube parameter.

Tensile box using compress-expand tube as core of absorption energy see figure 7.17, material properties of tensile box see table 7.7 (a), material properties of bar at table 7.7 (b). and detail parameters of compress-expand tube followed table 7.7 (c) Compress-expand tube in this study followed from previous research which consists of hardening ratio (E_h/E) 1/20 and 1/100, see figure 7.20 (a) and 7.20 (b).

Table 7.7 (a). Tensile box properties

Properties	Value
Yield stress σ_y [Mpa]	E/1000
Young modulus E [GPa]	205.9
Poisson ratio	0.3
Thickness of tube [mm]	1; 2; 3
Radius of tube [mm]	10; 20; 30; 40; 50
Hardening ratio E_h/E	1/100
Total length of tube [mm]	200
Ratio compress-expand	1:2:1

Table 7.7 (b). Bar properties

Properties	Value
Yield stress σ_y [Mpa]	E/1000
Young modulus E [GPa]	205.9
Poisson ratio	0.3
Radius of Bar [mm]	20
Type of Bar	Solid

Table 7.7 (c). Compress-expand tube parameter

Properties	Value
Thickness (t) [mm]	1.0; 2.0; 3.0
Radius (R) [mm]	20.0; 30.0; 40.0; 50.0
Total length (L) [mm]	200.0
Ratio ($L_0 : L_1 : L_2$)	1 : 2 : 1
Angle (α) [°]	30°

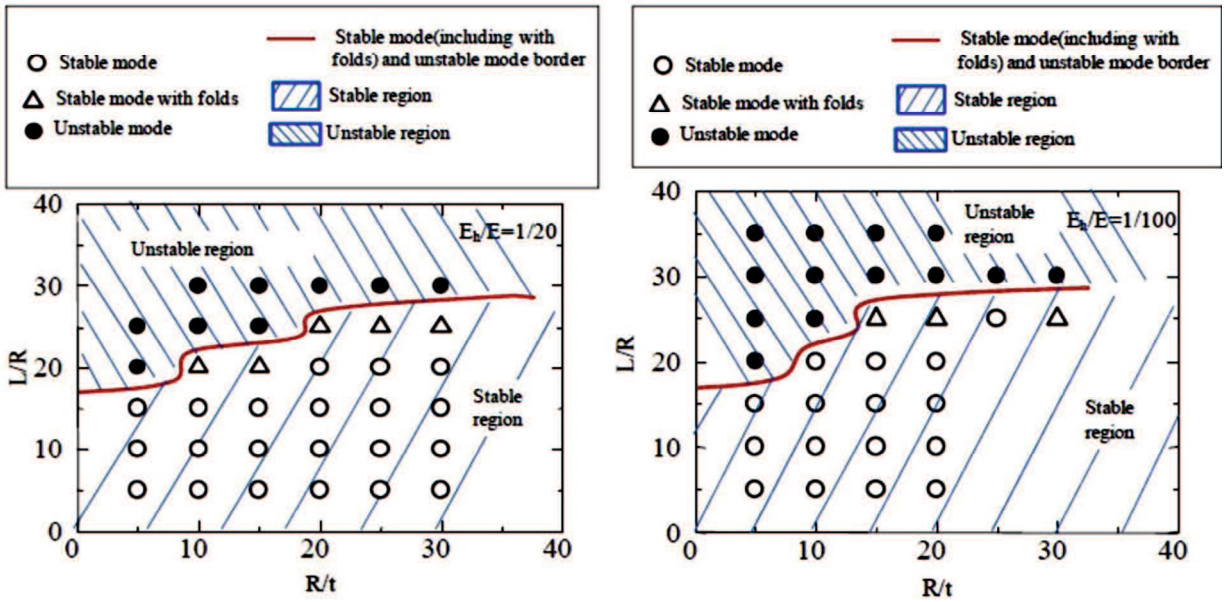

(a). Hardening ratio Eh/E=1/20. (b). Hardening ratio Eh/E=1/100.

Figure 7.20. Deformation map of compress-expand tube.

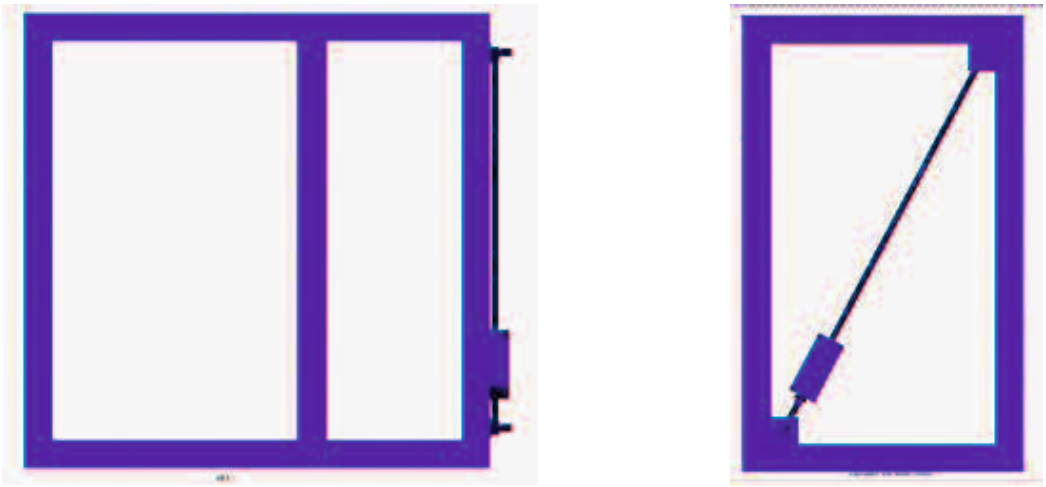

(a). Side view of cab frame. (b). Back view of cab frame.

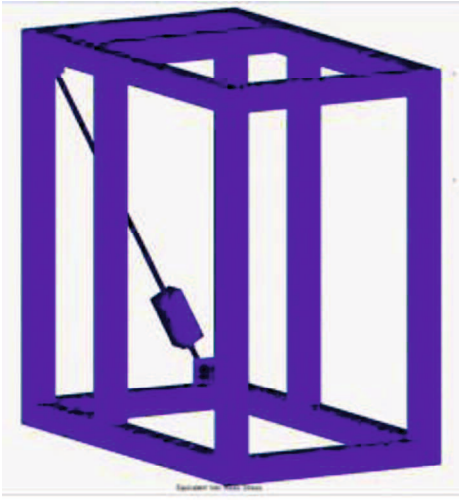

(c). Isometric view of cab frame.

Figure 7.21. Finite element simulation of cab frame using tensile crash box.

7.7 Result of Cab Frame Simulation Using Tensile Crash Box

Simulation of cab frame using tensile box with compress-expand tube thickness from 1 [mm] until 3 [mm], radius from 10 [mm] until 50 [mm], and hardening ratio (Eh/E) 1/20 and 1/100. Result of simulation curve cab frame using tensile box shown at figure 7.22 until figure 7.24. List of all simulation see table 7.8.

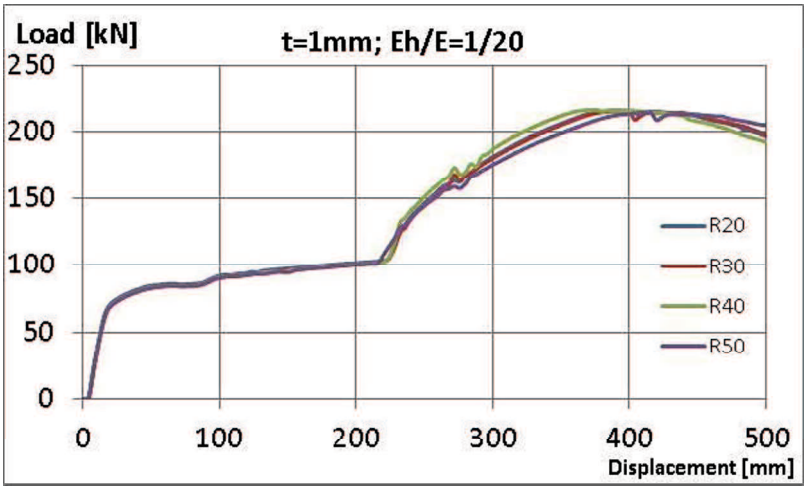

(a). Load-displacement curve (t=1mm, E_h/E=1/20).

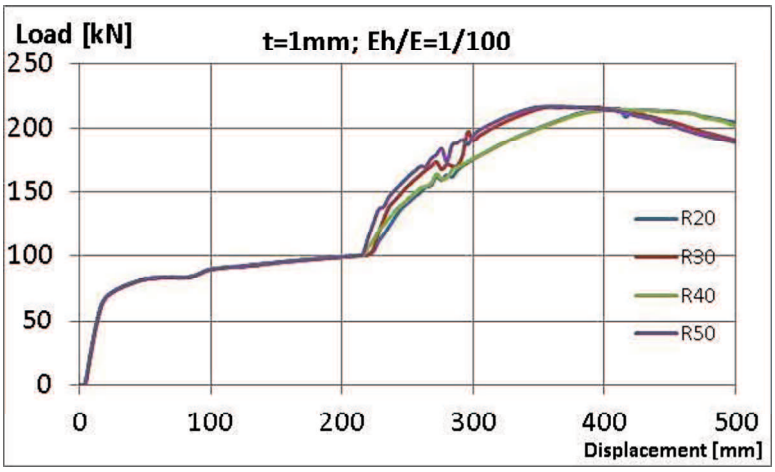

(b). Load-displacement curve (t=1mm, E_h/E=1/100).

Figure 7.22. Load-displacement curve of cab frame using tensile box (t=1mm).

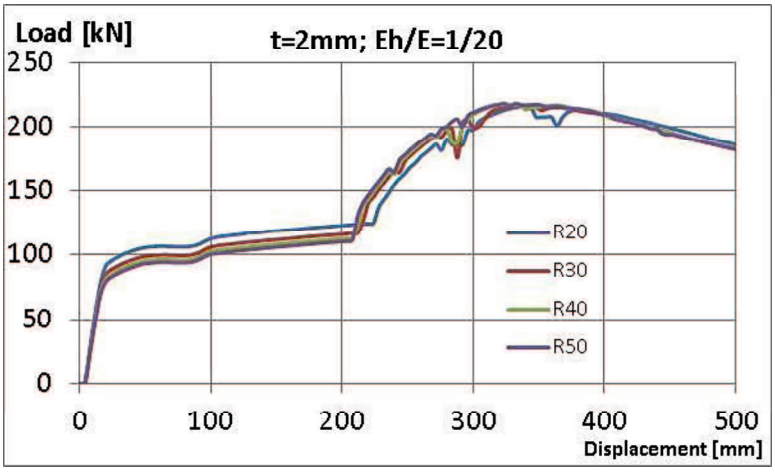

(a). Load-displacement curve (t=2mm, E_h/E=1/20).

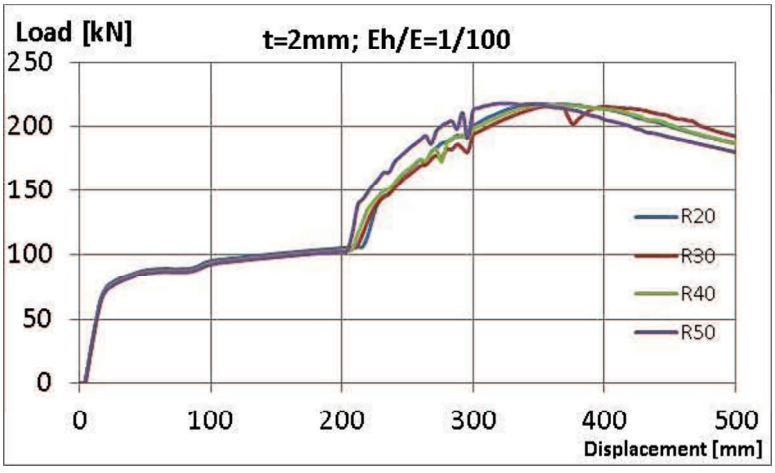

(b). Load-displacement curve (t=2mm, E_h/E=1/100).

Figure 7.23. Load-displacement curve of cab frame using tensile box (t=2mm).

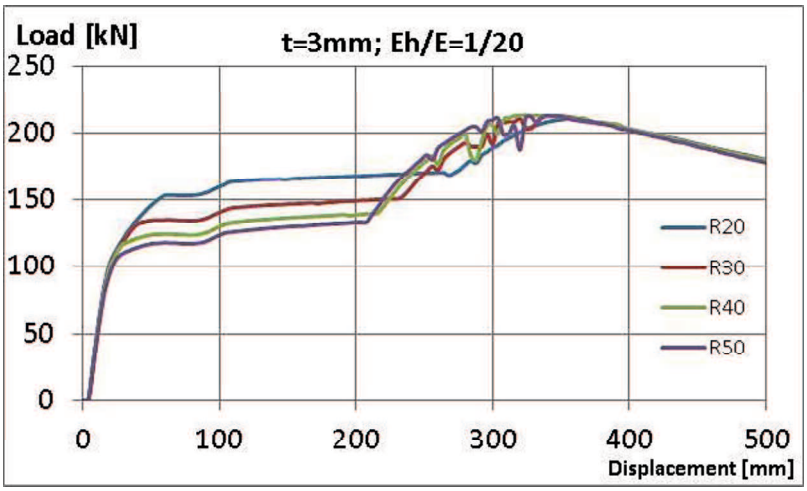

(a) Load-displacement curve (t=3mm, E_h/E=1/20).

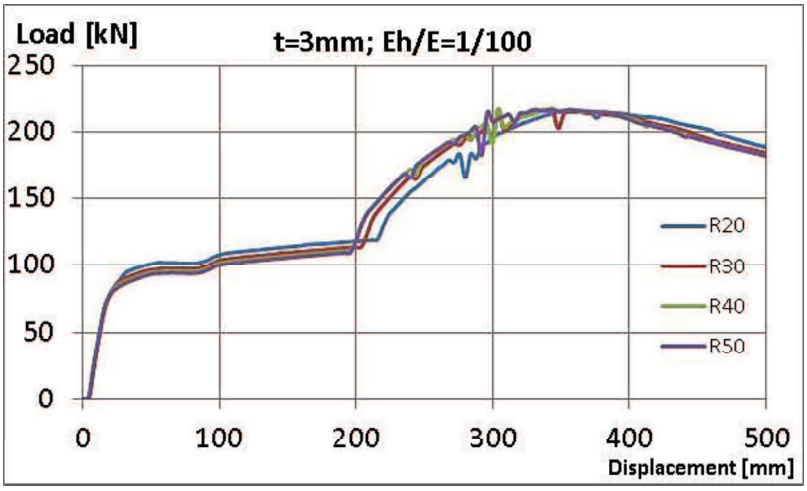

(b) Load-displacement curve (t=3mm, E_h/E=1/100).

Figure 7.24. Load-displacement curve of cab frame using tensile box (t=3mm).

From table 7.8 the highest result of ROPS using tensile crash box obtain at thickness condition of tube 3mm, radius 20mm, and E_h/E=1/20. And the lowest condition obtain at thickness 1mm, radius 10mm, and E_h/E=1/100. Highest condition and lowest condition then discussed and compare with cab without tensile crash box (cab frame only) and cab using bar only at rear diagonal. Detail analysis of those conditions see figure 7.25 and figure 7.26.

Table 7.8. Result of simulation cab frame using tensile crash box.

Radius [mm]	thickness [mm]	Energy [kJ]	
		Eh/E1/20	Eh/E1/100
10	1	unstable	66.49
20		72.48	71.29
30		72.20	72.64
40		72.73	71.47
50		71.56	73.25
10	2	unstable	unstable
20		77.96	74.82
30		77.29	74.41
40		77.06	74.56
50		76.92	75.19
10	3	unstable	unstable
20		85.91	77.15
30		82.96	77.25
40		81.64	77.21
50		80.51	77.05
ROPS only		56.84	

7.8 Analysis of Cab Frame Using Tensile Crash Box

Figure 7.25 shows cab frame using tensile crash box with thickness of compress-expand tube t=3mm, and R=20mm has biggest result compare with cab only (specimen L12-7) and cab using bar (R10mm). Those cab frame absorb more energy 51.14% than cab specimen L12-7, because tensile crash box provide additional plastic deformation on entire ROPS structure. Maximum energy absorption of cab using tensile crash box obtain at condition of compress-expand tube also at maximum condition (displacement 90mm). It seem that tensile crash box full functionally improve the absorption energy. When the displacement of compress-expand tube more than 90mm cab's load-deformation become decrease, because compress-expand tube become unstable deformation mode. Cab frame using bar (R10mm) also obtain improve energy absorption 23.40%. Increasing radius of bar will not increase the energy absorption, because cab structure become more stiffness and trigger buckling at certain area of frame.

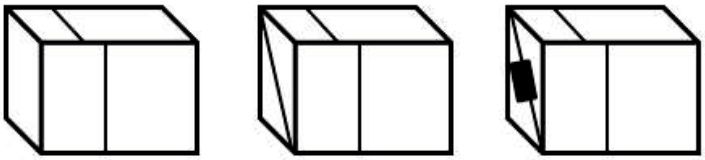

(1)Cab only (2) cab+bar(R10mm) (3) cab+tensile crash-box

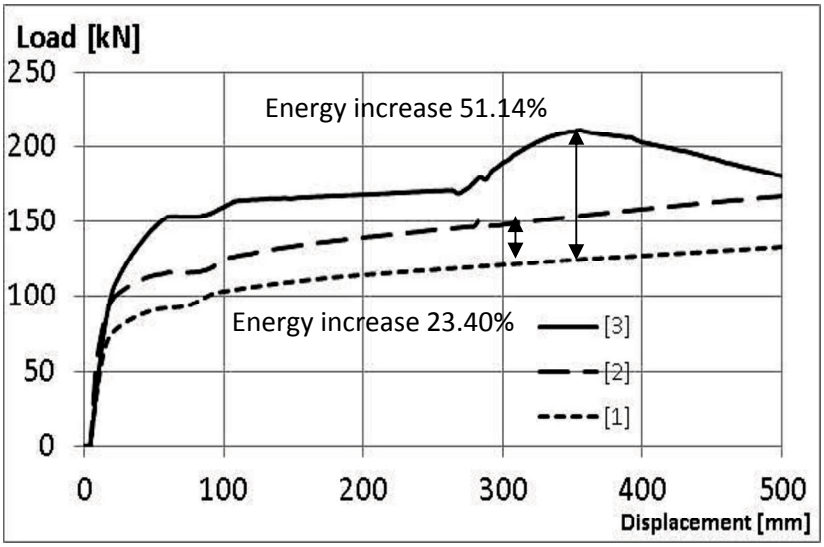

Figure 7.25 Comparison result of ROPS using tensile crash box (compress-expand tube t=3mm R=20mm).

Figure 7.26 shows cab frame using tensile crash box with compress-expand tube t=1mm, and R=10mm. At this condition cab frame using tensile crash box also obtain highest energy compare the others. Cab absorbs more energy 32.37% than cab specimen L12-7. Maximum energy absorption of cab using tensile crash box obtain at condition of compress-expand tube over than its stable condition (more than 120mm). It seems that tensile crash box overload and stop absorb the energy.

Figure 7.27 shows that energy absorption of cab frame was highly influence by thickness of compress-expand tube. When the radius of compress-expand tube different for example at thickness (t = 2 mm) for both hardening ration (Eh/E = 1/100 and Eh/E = 1/20) energy absorption of cab frame from radius (R = 20 mm) until (R = 50 mm) was small different. This condition also similar for thickness (t = 1mm), for thickness (t = 3mm) similar condition happen at (Eh/E=1/100) while (Eh/E=1/20) energy absorption of cab frame was different for different radius condition, because high hardening ratio make the stiffness of compress-expand tube higher at this thickness level. We can conclude that energy absorption of cab frame was highly influence by thickness condition of compress-expand tube.

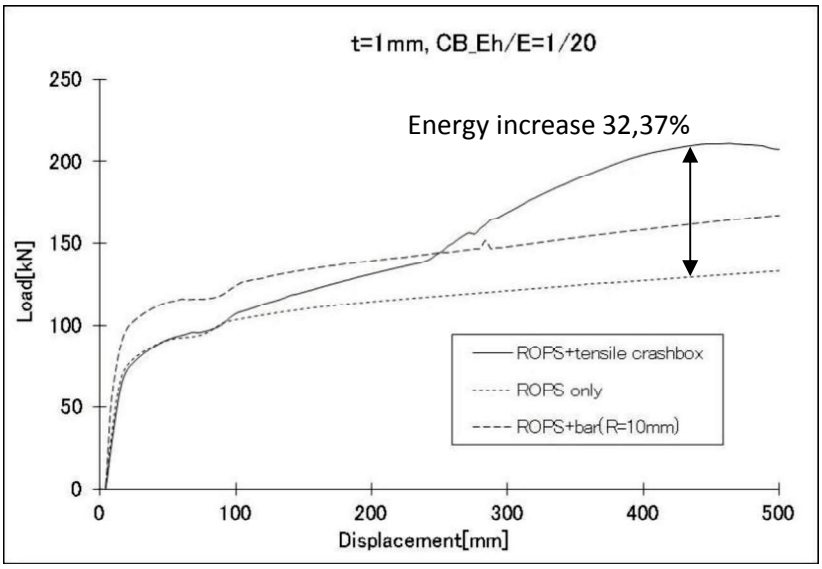

Figure 7.26. Comparison result of ROPS using tensile crash box (compress-expand tube t=1mm R=10mm).

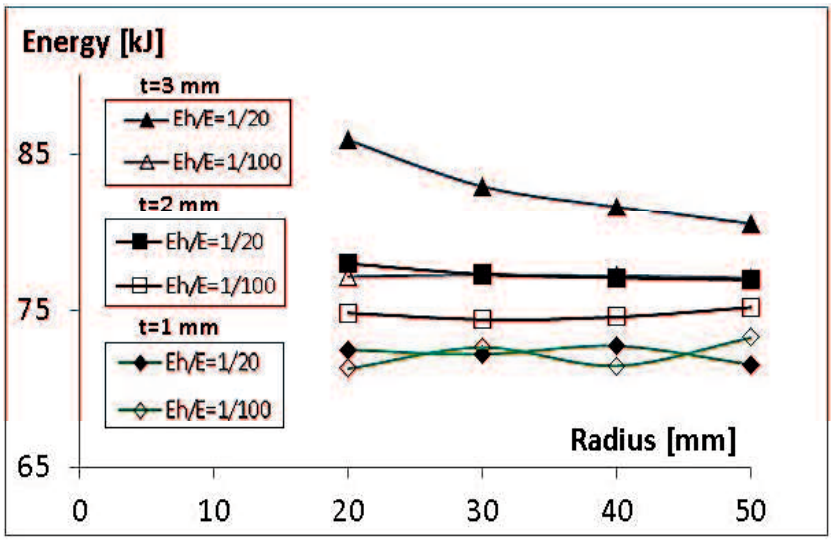

Figure 7.27. Energy absorption cab frame - Radius compress-expand tube curve.

From finite element simulation figure 7.27 show that tensile crash box has wide range of absorption energy using for various (Length/Radius) L/R and (radius/thickness) R/t condition. It is possible to use different size of compress-expand tube as core in tensile crash box for various target of energy absorption. Also it is possible to use same ROPS for different operating weight by only change the compress-expand tube as the core of tensile box.

7.9 Validation Finite Element Model with another Research Model

The research also investigates the finite element model designed by Hitachi. ROPS developed by Hitachi has detail design and specific material condition. The data was collect

from published paper by Hitachi [64]. ROPS model was used in machine ZX200-3. As the comparison, a six post ROPS created according to Hitachi specification.

Figure 7.28. Hitachi's cab frame model.

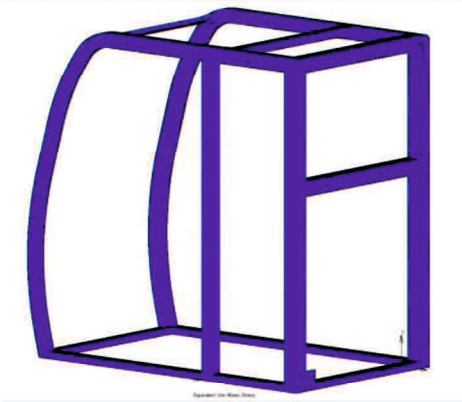

Figure 7.29. Cab frame model of this simulation.

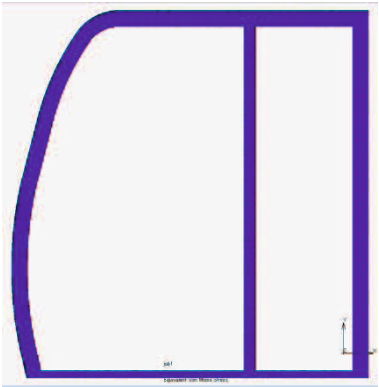

(a). Side view of cab frame.

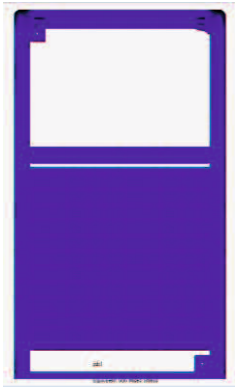

(b). Back view of cab frame.

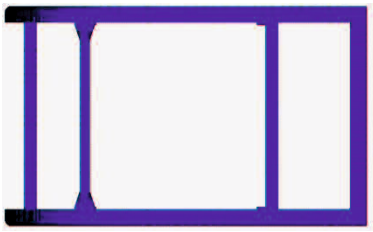

(c). Bottom view of cab frame.

Figure 7.30 Finite element model of cab frame of this study.

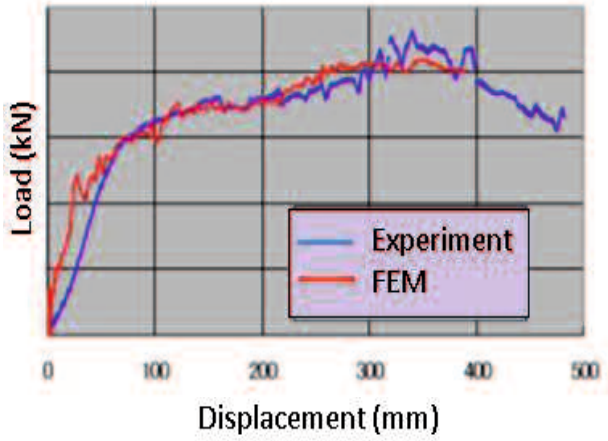

(a). Load-displacement curve of Hitachi cab frame.

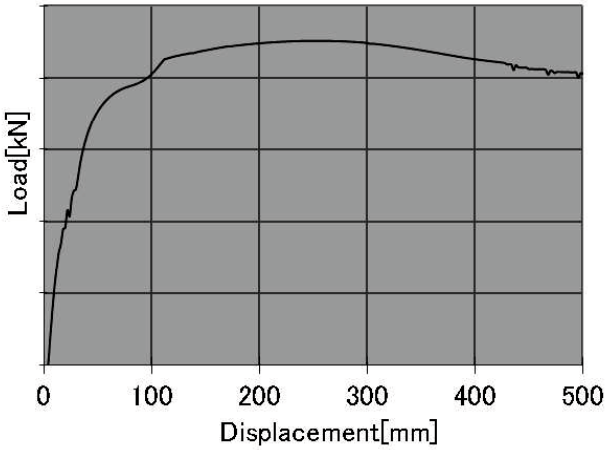

(b). Load-displacement curve from this research simulation.

Figure 7.31. Comparison load-displacement curve of Hitachi and this research simulation.

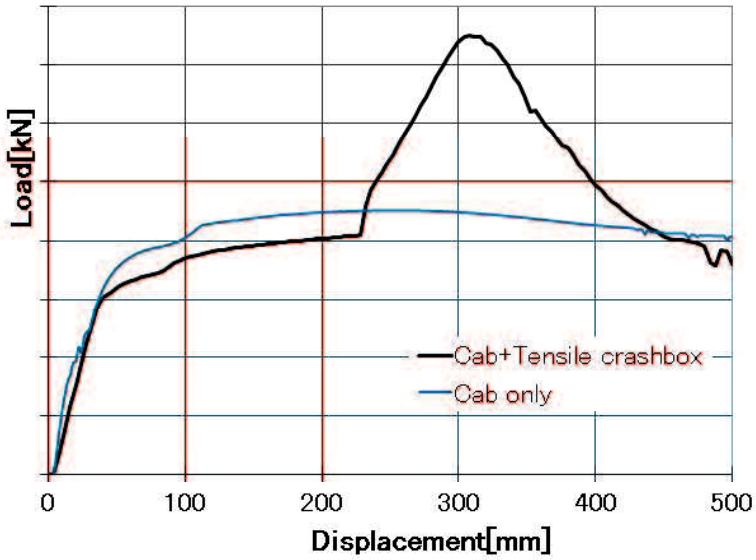

(a). Load-displacement curve of cab frame only and cab frame using tensile crash box (R=20mm, t=3mm, Eh/E=1/20).

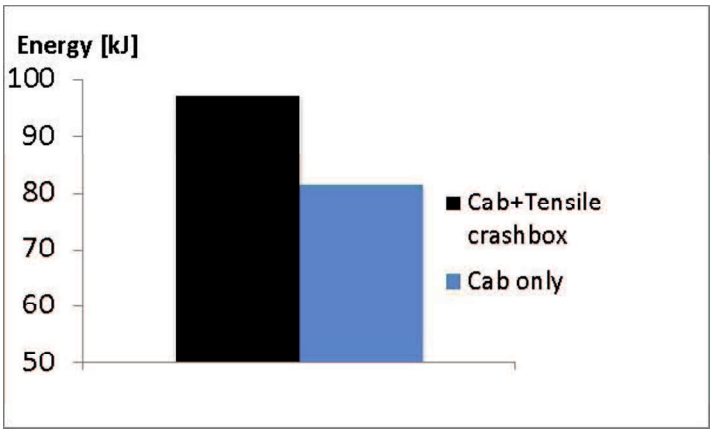

(b). Comparison Energy between cab frame only and cab frame using tensile crash box (R=20mm, t=3mm, Eh/E=1/20).

Figure 7.32. Comparison result of cab frame only and cab frame using tensile crash box in validation model.

Figure 7.31(a) shows that load-displacement result from Hitachi experiment and simulation has a similar result. It is a good example of validation condition in development cab frame. The simulation may reflect real condition in cab frame experiment, and this will speed up the process of development. This research also develop new cab frame model similar with Hitachi model, but the design purpose is to develop alternate design which have similar characteristic load-displacement. Such process was known as benchmarking in product development process. Figure 7.31(b) show that the simulation model has similar result with Hitachi model. Figure 7.32(a) show comparison load-displacement curve between

cab frame only and cab frame using tensile crash box from finite element simulation of validation model.

From finite element simulation of this study cab frame using new energy absorbing mechanism (Tensile crash box) could increase energy absorption than the conventional cab frame. The proposed mechanism removes the horizontal back pillar which usually designer thought to be stronger, and replace with tensile mechanism to support the deformation of cab frame. Comparison the finite element simulation of this study with the evaluation data of the preceding research obtained that cab using a new energy absorption mechanism could increase performance in roll-over condition. In line with increasing ability of ROPS, it is possible to design single cab frame for various operating weight machine by adjust the size of compression-expansion member according to the ROPS standard testing criteria.

7.10 Conclusion

In this study cab frame using new mechanism of energy absorption is investigated using finite element analysis. The propose mechanism was removed the horizontal rear pillar where local buckling obtain and reduce performance of cab frame, and usually designer thought to improve these rear pillar. The new mechanism introduce tensile crash box as energy absorption and replace rear pillar with this part at back side diagonal of cab frame. The tensile crash box used compress-expand tube model to absorb energy when rolling over happen at cab frame. Comparison of finite element simulation of this study with evaluation data from preceding research result a conclusion follow:

1. Improve cab frame energy absorption show highest result when applied at back side diagonal of cab frame because the diagonal side carry more displacement when cab deformation in roll over condition.
2. Cab frame using tensile crash box improve energy absorption up more than 50% compare than cab frame only (specimen L12-7). Because plastic deformation in roll over condition also absorb together between cab and tensile crash box.
3. Energy absorption of cab frame was highly influence by thickness condition of compress-expand tube. The highest energy absorption of this study was obtain at thickness (t = 3mm), radius (R = 20mm), and hardening ration (Eh/E = 1/20).
4. It is possible to increased energy absorption of ROPS without change the cab frame design using different size of tensile crash box core (compress-expand tube parameter).

CHAPTER VIII

GENERAL CONCLUSION

8.1 Conclusions.

The research of cab frame was described in several chapters to provide comprehensive explanation about absorption energy on rolling over phenomenon at ROPS. Finite element analysis and preceding simulation from another research in cab frame was used to improve reliability quality of simulation result. According to research investigation, main conclusion of this research pointed as:

1. Research investigation on the characteristic of cab frame/ ROPS at chapter 4 showed the different thickness level produced specific load-deformation curve and energy-deformation curve. Using Taguchi's method, thickness level of each specimen arranged to represented full combination experiments and could produce specimen with highest absorption energy. Local wrinkles which become weak points in the four different regions of the cab frame are obtained. Importance part of typical 6 post ROPS was vertical pillars (A, C, and H pillars). These pillars carry deformation of whole structure. Concentration of stress at these pillars triggers local wrinkle and reduce energy absorption. Further effort to increase performance at vertical pillar of ROPS is by given pre-treatment bending. Effect of pre forming on vertical pillar, investigated using finite modeling shown that initial stress of pre-treatment pillars are higher than non-pre-treatment.
2. Chapter 5 study on bending characteristic of square tube with expanded compression type energy absorption part for the purpose of preventing bending collapse show that bending capacity of tube increased when using absorption part. Collapse mode of square tube was highly influenced by thickness condition of the absorption part and dimension of cross section area of tube. Flat collapse mode shows no buckling at any area that high energy absorption characteristic can be achieved.
3. From chapter 6 obtain that the optimum design shape of the cab frame using optimization pattern of thickness condition could improve stress distribution at frame according to the three observation points on the square tube cross section. The energy absorption is increased while local buckling also reduced. Comparison of finite

element simulation before and after optimizations significantly shows reduces local buckling at certain frame.

4. It is obtained from finite element simulation at chapter 7 by using a new energy absorbing mechanism with the compression-expansion type absorbing member could increase energy absorption on the ROPS using the proposed mechanism than the conventional ROPS. The proposed mechanism shows highest result when applied at diagonal rear side of ROPS, because the diagonal side carries more displacement when ROPS deformation in roll over condition and the load direction can be reversed which change from compression become tensile so it can be pulled, and the load transmitted to the frame can be absorbed. Comparison the finite element simulation of this study with the evaluation data of the preceding research. It is obtained that ROPS using a new energy absorption mechanism could increase performance in roll-over condition without change the design of cab frame by adjust the size of compression-expansion member.
5. Finally, the result of this research in study of ROPS using new mechanism of absorption collision energy on rolling-over protective structure (ROPS) using new mechanism of energy absorption could enhance the ROPS performance. In line with increasing ability of ROPS it is possible to design single cab frame for various operating weight machine by adjust the size of the tensile crash box (compress-expand tube parameter) according to the ROPS standard testing criteria.

8.2 Future Development.

This research **s**tudy about absorption energy on rolling over protective structure (ROPS) using tensile crash box has future development in several ways:

1. It is possible to develop cab frame with tensile crash box with various size according to requirement and condition of cab frame.
2. Tensile crash box also possible to develop as energy absorption at various area such as in building structures, and bridge. The connection point must investigate further in tensile direction.
3. It is also possible to develop tensile mechanism for more than one direction of absorption, for example in tractor roll cage which is possibilities of rolling accident from both sides. To comply with this condition additional joint needs investigate and study further.

REFERENCES

[1] Yamagata, K., Tsumura, D. 2007. Introducing a simulation of a cab protecting operator during rolling over of a hydraulic excavator. Komatsu Tech Rep, vol. 52, no. 2, p. 2-7.

[2] Karlinski, J., Rusiński, E., Smolnicki, T. 2008. Protective structures for construction and mining machine operators. Automation in Construction, vol. 17, no. 3, p. 232-244.

[3] ISO3471 (2008). Earth-moving machinery Roll-over protective structures Laboratory tests and performance requirements. Geneva, International Organization for Standardization, Geneva.

[4] Adachi, T., Tomiyama, A., Araki, W., Yamaji, A. 2008. Energy absorption of a thin-walled cylinder with ribs subjected to axial impact. International Journal of Impact Engineering, Vol. 35, no. 2, p. 65-79.

[5] Jixin, W., Mingyao, Y., and Yonghai, Y. 2011. Global Optimization of Lateral Performance for Two-Post ROPS Based on the Kriging Model and Genetic Algorithm. Journal of Mechanical Engineering, vol. 57, pp. 760-767.

[6] Chen, C., Wang, Q., Zhang, Y., Zhang, Yan., and Si, J. 2012. Effect of lateral stiffness coefficient of loader ROPS on human injury in a lateral rollover incident. Biosystems Engineering, Vol. 113, pp. 207-219.

[7] Andrews, K, R, F., England, G, L., and Ghani, E. 1983. Classification of the axial collapse of cylindrical tubes under quasi-static loading. International Journal of Mechanical Sciences, Vol. 25(9-10), pp. 687-696.

[8] Elmarakbi, A., Long, Y, X., and MacIntyre, J. 2013. Crash analysis and energy absorption characteristics of S-shaped longitudinal members. Thin-Walled Structures, Vol. 68, pp. 65–74.

[9] Haruyama, S., Oktavianty, O., Darmawan, Z., Kyoutani, T., and Kaminishi, K. 2016. Study on Energy Absorption Characteristic of Cab Frame with FEM. International Journal of Mechanical, Aerospace, Industrial, Mechatronic and Manufacturing engineering, Vol. 10, No:3, pp. 570-576.

[10] Pardeshi, V. 2015. Design of ROPS (Roll over Protective Structure) For Operator Cabin. International Journal on Future Revolution in Computer Science & Communication Engineering, Vol: 1, issue: 2, ISSN: 2454-4248. P, 06-09.

[11] Karlinski, J., Ptak, M., Dzialak, P. 2013. Simulation Test of Roll-Over Protection Structure. Civil and Mechanical Engineering, Vol. 13, no. 1, p. 57-63.

[12] Khorsandi, F., Ayers, P, D., & Truster, T, J. 2017. Developing and evaluating a finite element model for predicting the two-post rollover protective structure nonlinear behavior using SAE J2194 static test. Biosystem engineering, Vol. 156, pp. 96-107.

[13] Mangado, J., Arana, J, I., Jaren, C., Arazuri, S., & Arnal, P. 2007. Design calculation on roll-over protective structures for agricultural tractors. Journal of Biosystems Engineering, vol. 96, no.2, pp. 181-191.

[14] Alfaro, J, R., Arana, I., Arazuri, S., & Jaren, C. 2010. Assessing the safety provided by SAE J2194 standard and code 4 standard code for testing ROPS, using finite element analysis. Journal of Biosystems Engineering, vol. 105, pp. 189-197.

[15] Kim, T, H., & Reid, S, R. 2001. Multiaxial softening hinge model for tubular vehicle roll-over protective structures. International Journal of Mechanical Sciences, vol. 43, pp. 2147-2170.
[16] Fabbri, A., and Ward, S. 2001. Validation of a Finite Element for The Design of Roll-over Protective Frame Structure (ROPS) for Agricultural Tractors. Journal of Biosystems Engineering, vol. 81(3), pp. 287-296.
[17] Ayers, P., Khorshandi, F., Wang, X., and Araujo, G. 2018. ROPS design to protect operators during agricultural tractor rollovers. Journal of Terramechanics, vol. 75, pp. 49-55.
[18] Harris, J, R., Winn, G, I., Ayers, P, D., and McKenzie Jr, EA. 2011. Predicting the performance of cost-effective rollover protective structure designs. Safety Science, vol. 49, pp. 1252-1261.
[19] Abramowicz, W. 2003. Predicting the performance of cost-effective rollover protective structure designs. Thin-Walled Structures, vol. 41, pp. 91-107.
[20] Alkhatib, S, E., Tarlochan, F., Hashem, A., and Sassi, A. 2018. Collapse behavior of thin-walled corrugated tapered tubes under oblique impact. Thin-Walled Structures, vol. 122, pp. 510-528.
[21] Zhang, X, W., Tian, Q, D., and Yu, T, X. 2009. Axial crushing of circular tubes with buckling initiators. Thin-Walled Structures, vol. 47, pp. 788-797.
[22] Haruyama, S., Khaidir, A., Kaminishi, K., Chen, D, H. 2013. Modes of Collapse Of Compress-Expand Member Under Axial Loading. International Scholarly and Scientific Research & Innovation, vol. 7(2), pp. 550- 557.
[23] Johnson, A, F. 1973. Bending and Torsion of Anisotropic Beams. International Journal Solids Structures, Volume 9, pp 527-551.
[24] Alexander, J, M. 1959. An approximate analysis of the collapse of thin cylindrical shells under axial loading. Imperial College of Science and Technology. Available at: http://qjmam.oxfordjournals.org/.
[25] Zheng, B., Shu, G., Xin, L., Yang, R., and Jiang, Q. 2016. Study on the Bending Capacity of Cold-formed Stainless Steel Hollow Sections. Structures, vol. 8, pp. 63-74.
[26] Paulsen, F., Welo, T., and Perry, O, P. 2001. A design method for rectangular hollow sections in bending. Journal of Materials Processing Technology, vol. 113, pp. 699-704.
[27] Chen, D, H., and Masuda, K. 2016. Rectangular hollow section in bending: Part I – Cross sectional flattening deformation. Thin-walled structures, Vol. 106, pp. 495-507.
[28] Franceschetti, B., Lenain, R., and Rondelli, V. 2014. Comparison between a rollover tractor dynamic model and actual lateral tests. Biosystems Engineering, vol. 127, pp. 79-91.
[29] Wang, J., Afshan, S., Schillo, N., Theofanous, M., Feldmann, M., and Gardner, L. 2016. Material properties and compressive local buckling response of high strength steel square and rectangular hollow section. International Journal of Engineering Structures, Volume 130, pp 297-315.
[30] Chi, K, S., and Lin, T, H. 1977. Slope Deflection Method For Elastic-Plastic Multi-story Frames. International Journal Solids Structures, Volume 13, pp 125-135.
[31] Stafford, R, O., and Pattichis, M. 1978. Bending and Torsion of Anisotropic Cantilevers. International Journal of Mechanical Science, Volume 20, pp 395-405.

[32] Wierzbicki, T., Recke, L., Abramowicz, W., Gholami, T., and Huang, J. 1994. Stress Profiles In Thin-Walled Prismatic Columns Subjected to Crush Loading – II Bending. Computer and Structures, Volume 51, No 6, pp 625-641.
[33] Kecman, D. 1983. Bending Collapse of Rectangular and Square Section Tubes. International Journal of Mechanical Science, Volume 25, No 9-10, pp 623-636.
[34] Kim, T, H., and Reid, S, R. 2001. Bending Collapse of Thin-Walled Rectangular Section Columns. Computer and Structures, Volume 79, pp 1897-1911.
[35] Masuda, K., Chen, D, H., and Ozaki, S. 2009. Study on Pure Bending Collapse of Square Tubes in Consideration of Work Hardening effect.. Transaction of The Japan Society of Mechanical engineers (in Japanese), Volume 75, No 749, pp 13-20.
[36] Masuda, K., and Chen, D, H. 2009. Study on Role of Partition Plates in Square Tube Subjected to Pure Bending. Transaction of The Japan Society of Mechanical engineers (in Japanese), Volume 75, No 753, pp 38-45.
[37] Haruyama, S., Tanaka, H., Chen, D, H., and Khaidir, A. 2012. Study on the Deformation Modes of an Axially Crushed Compact Impact Absorption Member. World Academy of Science, Engineering and Technology, Volume: 6.
[38] Masuda, K., and Chen, D, H. 2012. Maximum moment of rectangular tubes subjected to pure bending. Transactions of JSME, A78, pp. 1340-1347.
[39] Paulsen, F., and Welo, T. 2001. Cross-sectional deformation of rectangular hollow sections in bending: Part I – experiments. International Journal of Mechanical Sciences, vol. 43, pp. 109-129.
[40] Mikhail, V., Sukhoterin., sergey, O., Baryshnikov., Kseniya, O., and Lomteva. 2016. On homogenous solution of the problem of a rectangular cantilever plate bending. St Petersburg Polytechnical University Journal: Physics and Mathematics, vol. 2, pp. 247-255
[41] Yamagata, K., and Tsumura, D. 2006. Introducing a Simulation of Cab Protecting Operator During Rolling Over of Hydraulic Excavator. Komatsu Technical Report, vol. 52, No. 158.
[42] Kenzo T., "Construction Machinery Fall Protection Structure of Safety Measures Hydraulic Excavator when Rollover (ROPS) up to Japan International Standards", Precision Engineering Journal, Vol.75, No.3 (2009), pp. 341-345.
[43] Hiroshi I., Toshiaki H., "Safety Measures of Construction Machinery", the construction project, (2010), pp.78-81.
[44] Tadaaki N., Sasaki T., "Research on Large Hydraulic Excavators Fall Protection Structure", construction project, (2004), pp. 43-48.
[45] Kenichi Y., Tsumura D., "Introduction of Hydraulic Excavator Simulation for Driver's Protective Structure Cab during Fallen", Komatsu Technical Report, Vol.52, No.158 (2006), pp. 2-7.
[46] Hiro N.T., Ito T., "ROPS Structure Cab of Production Technology", Komatsu Technical Report, VOL. 54, No.161 (2008), pp.9-16.
[47] Kozeni, T., Haruyama, S., Kaminishi, K., “Study of Energy Absorption of Combined Model of Cylindrical Compression-Expansion Tube and Thin Cylindrical Tube”, Proceedings of the 8th International Conference on Innovation & Management, (2011), pp. 1052-1056.

[48] Tawk, I., Rishmany, J., Gergess A., "Assessment of Residual Stresses due to Cold Bending Structural Steel Girders using Finite Element Modeling", Athens Journal of Technology & Engineering, Vol. X, No. Y.
[49] Prasad, V., Mohan, K., "Finite Element Simulation of Residual Stresses in Roller Bent Section", IJSR, 2013.
[50] Chen, D.H. 2016 Crush Mechanics of Thin-Walled Tubes. Florida: Taylor & Francis Group.
[51] McCann. 2006. Heavy equipment and truck-related deaths on excavation work sites. Journal of Safety Research, Vol. 37, pp. 511-517.
[52] Guzzomi, A, L., Rondelli, V., Guarnieri, A., Molari, G., & Molari, P, G. 2009. Available energy during the rollover of narrow-track wheeled agricultural tractors. Journal of Biosystem Engineering, vol. 104, pp. 318-323.
[53] OEEC. 1959. OEEC Standard code for the official testing of agricultural and forestry tractors. Paris, France: Organization for the European Economic Co-operation.
[54] PennStateExtension. 2017. Pennstate official website. [online] Available at: http://www.extension.psu.edu/business/ag-safety/vehicles-and-machine/tractor-safety/e42/ [Accessed July, 19, 2017].
[55] SAE. 2009. Roll-Over Protection Structures (ROPS) for wheeled agricultural tractors. SAEJ2194. SAE International.
[56] OECD. 2008. OECD standard code for the official testing of rollover protective structures on agricultural and forestry tractors. Paris, France: Organization for the European Economic Co-operation.
[57] Wierzbicki, T., Recke, L., Abramowicz, W., & Gholami, T. 1994. Stress profiles in thin-walled prismatic column subjected to crush loading-I, Compression. Journal of Computers and Structures, vol. 51, pp. 611-623.
[58] Haruyama, S., Muhamad, A, K., kaminishi, K., & Chen, D, H. 2013. Modes of collapse of compress-expand member under axial loading. Journal of World Academy of Science, engineering and Technology, vol. 7, pp. 550-557.
[59] Haruyama, S., Tanaka, H., Chen, D, H. & Muhamad, A, K. 2012. Study on the deformation modes of an axially crushed compact impact absorption member. Journal of World Academy of Science, engineering and Technology, vol. 6, pp. 1105-1113.
[60] Haruyama, S., Muhamad, A, K., Kyoutani, T., Chen, D, H., & Kaminishi, K. 2013. Implementing ALD in product development: The effect of geometrical dimensions on tubular member deformation. Journal of World Academy of Science, engineering and Technology, vol. 7, pp. 1114-1118.
[61] Shinohara, M., Chen, D, H., & Ozaki, S. 2009. Numerical study of axial crushing characteristic for square tube (Japanese version). The Japan Society of Mechanical Engineers, vol. 6-4, pp. 191-192.
[62] Haruyama, S., Darmawan, Z., & Kaminishi, K. 2017. Study on bending characteristic of square tube using energy absorption part. Journal of World Academy of Science, engineering and Technology, vol. 11-4, pp. 885-891.
[63] SAE J1040. 1994. Performance criteria for Rollover Protective Structures (ROPS) for construction, Earthmoving, Forestry, and Mining machines. Washington. The Executive Director Office of The Federal Register the United States of America.

[64] Tamura, K., Komatsu, K., and Iijima, T. Development of A Rollover Protective Structure (ROPS) cab for Hydraulic Excavators (Available in Japanese). Technical report of Hitachi Construction Machinery Co., Ltd.
[65] Marc Manual. 2012. Volume A: Theory and User Information. MSC Software Corporation. United States of America.
[66] Reynolds, S, J., and Groves, W. 2000. Effectiveness of Roll-Over Protection structures in Reducing Farm Tractor Fatalities. American Journal of Preventive Medicine, vol. 18, pp. 63-69.
[67] Alkhatib, S, E., Tarlochan, F., and Eyvazia, A. 2017. Collapse behaviour of thin-walled corrugated tapered tubes. Engineering Structures, vol. 150, pp. 678-692